Naturally-Sensitized Photoanodes for Molecular Photovoltaics

BY

HISHAM AGEEL MADDAH
B.S., King Abdulaziz University, 2012
M.S., University of Southern California, 2017

THESIS

Submitted as partial fulfillment of the requirements
for the degree of Doctor of Philosophy in Chemical Engineering
in the Graduate College of the
University of Illinois at Chicago, 2020

Chicago, Illinois

Defense Committee:

Sanjay Behura, Advisor

Vikas Berry, Chair and Co-advisor

Gang Cheng

Ying Liu

Matthew Daly, Civil and Materials Engineering

[TO MY FAMILY] – DEDICATION

This dissertation is dedicated to my family: my caring father (Ageel Maddah), my beloved mother (Hana Jamalallail), my encouraging wife (Ruba Hakeem), and the rest of my family (Mohammed, Ammar, and Shahad) for all their support, which kept me motivated to progress towards this big achievement. I also would like to dedicate this work to my little boy (Ziyad) who's the cherry on the top bringing joy, laughter, and blessing to me and my wife. Thank you all for always standing by my side, believing in me, trusting in my abilities, and telling me that I can do it. I am truly blessed to have such a family.

ACKNOWLEDGEMENT

This work would not have been possible to accomplish without the continuous support and valuable feedback provided by my advisor, co-advisor, and other committee members. I would like to express my sincere gratitude and appreciation to my dissertation advisor Dr. Sanjay K. Behura, who believed in me, kept me motivated, and guided me throughout my study towards the success and perfection of my research in a short time. Without him, it would not have been possible to refine and develop my research skills which resulted in producing more than five peer-reviewed publications. I would also like to extend my thanks to Dr. Vikas Berry (Chair of the committee and Head of the Chemical Engineering Department) for co-advising me with his generous help and feedback over the years that helped me to excel my research skills. I was very lucky to have such mentors who really cared about me as a graduate student and as a person. With their devoted efforts towards shaping me for academia, they have guided me to develop my critical thinking, scientific reasoning, academic writing, and teaching skills.

I would also like to acknowledge my committee members Dr. Gang Cheng, Dr. Ying Liu, and Dr. Matthew Daly for providing the time to serve on my committee. It was an absolute pleasure to work with them towards improving my research from the invaluable discussions, feedback, and suggested research directions and/or questions.

TABLE OF CONTENTS

LIST OF TABLES

LIST OF FIGURES

LIST OF ABBREVIATIONS AND NOMENCLATURES

PV	Photovoltaics
DSSCs	Dye-Sensitized Solar Cells
CE(s)	Counter Electrode(s) Or Cathode
e-h	Electron-Hole
CB	Conduction Band
LH	Light-Harvesting
RC	Reaction Center
PCE	Power Conversion Efficiency
SEM	Scanning Electron Microscopy
TCO	Transparent Conductive Oxide
ITO	Indium Tin Oxide
FTO	Fluorine Doped Tin Oxide
$[I^-/I_3^-]$	Iodide and Triiodide Redox Couple
S	Ground Energy State
S*	Higher Energy State or Excited-Dye Molecule
S^+	Oxidized Dye Molecule
HOMO	Highest Occupied Molecular Orbital
LUMO	Lowest Unoccupied Molecular Orbital
I_3^-	Iodide
$3I^-$	Triiodide
n	Conjugated Double Bonds
D-π-A	Donor-Acceptor-Substituted π-Conjugated Bridge
BChl or PBB	Chlorophyll A
PSI	Photosystem I Trimer
J_{sc}	Short-Circuit Current Density
V_{oc}	Open-Circuit Voltage
FF	Fill Factor
IPCE	Incident Photon-to-Current Efficiency
η	Quantum Yield of Photo-Generated Electrons

QE	Quantum Efficiency
Spx	Carotenoids
LHCII	Light-Harvesting Complex II
BRs	Bacteriorhodopsin Proteins and/or Bacterioruberin Carotenoids
PSI	Photosystem I Trimer
CSSC	Chromatophores Sensitized Solar Cell
NIR	Near-IR
TD-DFT	Time-Dependent Density Functional Theory
HTM	Hole-Transporting Materials
MAI	Methylammonium Iodide
PbI_2	Lead Iodide
$MAPbI_3$	Methylammonium Lead Iodide
HTL	Hole Transport Layer
ETL	Electron Transport Layer
HOPG	Highly Ordered Pyrolytic Graphite
PANI	Polyaniline
PEDOT	Poly(3,4-Ethylenedioxythiophene)
MWCNTs	Multi-Walled Carbon Nanotubes
HSG	Honeycomb-Structured Graphene
PDDA	Poly(Diallyldimethylammonium Chloride)
ERGO	Electrochemically Reduced Graphene Oxide
GNs	Graphene Nanosheets
NDG	Nitrogen Doped Graphene
THF	Tetrahydrofuran
GO	Graphene Oxide
$NaNO_3$	Sodium Nitrate
H_2SO_4	Sulfuric Acid
$KMnO_4$	Potassium Permanganate
H_2O_2	Hydrogen Peroxide
HCl	Hydrochloric Acid
-OH	Hydroxyl

-COOH	Carboxyl
rGO	Reduced Graphene Oxide
R_s	Series Resistance
MA	Methylammonium
FESEM	Field Emission Scanning Electron Microscope
IV	Current-Voltage
I_{cell}	Cell Current
KVL	Kirchhoffs's Voltage
KCL	Kirchhoffs's Current
I_{ph}	Cell Photo-Generated Current
I_0	Dark Saturation Current
I_r	Back Reaction (Recombination) Current
I_{sh}	Shunt (Leakage) Current
V_{PE}	Photoanode Electrode Voltage
R_{sh}	Shunt Resistance
R_r	Recombination Resistance
V_{cell}	Cell Voltage
q	Electron Charge
n	Ideality Factor
$k_B = k$	Boltzmann Constant
T	Absolute Temperature
I_{sc}	Short-Circuit Current
TE	Thermionic Emission
J-V	Current Density-Voltage
J_D	Diode-Generated Current Density
J_0	Dark Saturation and/or Leakage Current Density
RF(s)	Rectification Factor(s)
SBH=ϕ_{SBH}=Φ_{Bo}	Schottky Barrier Height
J_1	Apparent Current Density in both TiO_2 and $MAPbI_3$
J_2	Total Apparent Current Density in the Electrolyte

D_e	Diffusion Coefficients
N_e	Number of Electrons
E_g	Bandgap Energy
G	Generation Rate
L_n	Electron Diffusion Length
L_p	Hole Diffusion Length
Φ_0	Incident Photoflux
λ	Light Wavelength
$r(\lambda)$	Incident Light Loss
n_0	Electron Density in the Conduction Band of TiO_2
k_{et}	Recombination Reaction Rate
P_{max}	Maximum Power
P_{in}	Input Power
EQE = IPCE*	External Quantum Efficiency (*IPCE, defined previously)
$LHE(\lambda)$	Light-Harvesting Efficiency at Wavelength λ
φ_{inj}	Quantum Yield for Electron Injection
η_{coll}	Efficiency for The Collection of Electrons
IQE	Internal Quantum Efficiency
UV-Vis	Ultraviolet-Visible
A	Absorption Constant
ε	Molar Attenuation
b	Path Length
C	Concentration
WBG	Wide Bandgap
α	Absorption Coefficient
$\hbar\nu$	Photon Energy
t	Thickness of the Quartz Cuvette (Light Path)
OD	Optical Density
λ_{max}	Maximum Absorption
V_0	Maximum Theoretical Voltage (V_{oc}^{*}=V_0)

V_1	Voltage Loss at TiO_2/ITO Interface
V	Experimental (actual) Measured V_{oc}
A*	Richardson Constant of TiO_2
$\emptyset_{TiO_2-ITO}$	Schottky Barrier Height at the TiO_2/ITO Interface
z	Thickness of TiO_2
p	Porosity
τ	Tortuosity
D_1	Effective Diffusion Coefficients of I^-
D_3	Effective Diffusion Coefficients of I_3^-
C_3	Ion Concentration of I_3^-
E_F	Fermi Energy
E_V	Vacuum Level
Φ	Work Function
VBM	Valence Bands Maximum
E_{VB}	Valence Band
E_{CB}	Conduction Band
V_{bi}	Built-in Potential
E_{F_1}	Fermi Energy of the n-Type Semiconductor
E_{F_2}	Fermi Energy of the Metal (or p-Type Semiconductor)
Φ_M	Work Function of the Metal
χ	Electron Affinity of the Semiconductor
N_{eq}	Dark Equilibrium Density
N_{CB}	Effective Density of States of Conduction Band Electrons
(0)	Cells Before Photoanode Perovskite Cosensitization
(1)	Cells After Photoanode Perovskite Cosensitization
$V_{oc}\|_{\mathrm{Exp}}$	Actual or Experimentally-Tested Cell Output
V_2	Produced Voltage from the Semiconductor
ϕ_{TiO_2}	Work Function of TiO_2

ABSTRACT

Naturally-sensitized photoanodes in dye-sensitized solar cells (DSSCs) are promising alternatives to enhance photoabsorption, electron excitation/injection, but voltage loss remains a challenge. In this work, we focus on understanding perovskite cosensitization leveraging forward charge transport to address the voltage loss arising from ITO/TiO_2 junction's built-in potential in bio-sensitized DSSCs. The β-carotene-sensitized TiO_2 photoanode modified with added $MAPbI_3$ co-sensitizer cause an upward shifting in TiO_2 Fermi level (E_F). This phenomenon is predominantly attributed to increased initially injected electrons due to low $MAPbI_3$ bandgap (~1.87 eV) and high visible-light absorption. Thermal annealing of TiO_2/$MAPbI_3$ heterostructure ensures existing of both: (i) covalent bonding contributing to ultrafast interfacial charge separation, and (ii) strong van der Waals interactions between donor/acceptor species at TiO_2/$MAPbI_3$ interface facilitating electron injection. Enhanced charge separation and injection mechanisms at the TiO_2/$MAPbI_3$ interface increase the effective density of states (>2.46×10^{21} cm^{-3}) in TiO_2 conduction band (CB) and hence decrease its work function to 4.82 eV. The decrease in TiO_2 work function suppressed CB bending at the ITO/TiO_2 junction, which minimized the photoinduced electrostatic potential barrier up to 13.1%. This lessened Schottky barrier (ϕ_{SBH}<0.52 eV) only allow electrons tunneling, while inhibited back-electron transport reduced both current leakage and voltage loss yielding in high V_{oc} increased by 120% and PCE (>240%). $MAPbI_3$ incorporation also broadened photoanode absorbance by 2-fold, paving the way towards perovskite cosensitization to avoid voltage loss from bio-integrated photoanodes for photovoltaic and optoelectronic applications.

Chapter 1: Introduction

Maddah, H. A., Berry, V., & Behura, S. K. (2020). Biomolecular Photosensitizers for Dye-Sensitized Solar Cells: Recent Developments and Critical Insights. ***Renewable and Sustainable Energy Reviews***, *121*, 109678.

1.1 Solar Energy Conversion using Dye-Sensitized Molecular Devices

Non-renewable energy resources such as fossil fuels pose environmental concerns and will be diminished due to the limited oil/gas reserves as well as the increasing demand for energy. Econometric models estimated that fossil fuel reserves will be totally consumed by the year 2042 [1]. In contrast, solar energy is the most abundant, unlimited, free, and environmental-friendly energy among all the available renewable energy resources with power approximately 1.8×10^{11} MW from sun intercepted by the earth [2]. Photovoltaics (PV) is an efficient tool designed to harness solar power by converting incident photons to excitons for electricity generation [2]. However, commercial silicon-based solar cells (first-generation) are expensive to manufacture and are restricted to the terrestrial PV market only as compared to the second-generation PV systems (multi-crystalline Si) [3]–[7] and the emerging third-generation PV systems such as organic/inorganic perovskite solar cells [8]–[16], inorganic solar cells (Si, III-V compounds, alloys, CdTe, CIGS) [17]–[24], organic tandem solar cells [25]–[31], quantum dot solar cells [32]–[37] and dye-sensitized solar cells (DSSCs) [38]–[48], which are still in the development phase for being commercialized [49]. In 1991, O'Regan and Grätzel [38] initiated the idea of DSSCs inspired by natural photosynthesis and photography processes [50]. In natural photosynthesis, plants and fruits utilize their pigment molecules to transfer energy and electron for the conversion of light energy into chemical energy stored as sugars and carbohydrates. DSSC (Grätzel cell) is a thin-film photovoltaic (solar) cell that efficiently converts any visible light into electrical energy.

An intense research work [38] has been devoted to DSSCs from 1991 to 2014 which resulted in improving DSSCs efficiency from 7.1% to 13% as an attempt to involve DSSCs in commercial applications [51]. In 2015, Ye et al. reported in their recent review paper on DSSCs that maximum efficiency of 15% can be achieved with a solid-state mesoscopic TiO_2 DSSC sensitized with lead iodide perovskite ($CH_3NH_3PbX_3$) under AM1.5 illumination; which is expected to reach a future cell performance as high as 20%. The maximum recorded efficiency of commercial crystalline silicon solar cells is approximately 25% ($2.7–3.57/W) [52]. However, DSSCs are cost-effective solar cells with a potential to achieve production costs below $0.5/W of solar electricity owing to their inexpensive materials and components and also due to their explicit fabrication design that requires very little maintenance [2], [41], [49]. A typical DSSC system includes four major components: photoanode, photosensitizer, electrolyte, and counter electrode (CE) [49]. The cell converts visible light energy into electrical energy by sensitizing a wide bandgap semiconductor (e.g. TiO_2, ZnO and SnO_2) to inject a photo-excited electron at the interface between the semiconductor material and the monolayer sensitizer (commercial and/or natural dye) which both compose the photoanode electrode [50]. Nanoporous semiconductors have a large surface area and can absorb large amounts of the dye in order to harvest sunlight energy and generate electron-hole (e-h) pairs; illumination excites dye molecules to generate e-h pairs where charge separation occurs in femtoseconds due to the injection of an electron from the dye molecules into the conduction band (CB) of the semiconductor [42], [53]. To date, commercial photosensitizers used in DSSCs are limited to several types of organic dyes [44], ruthenium dyes [54], and platinum dyes [55]; however, these dyes are scarce in nature, synthetically produced, very expensive, and pose

a high risk of toxicity to humans (ecosystem pollution) [56]. Thus, research efforts have been shifted to focus on natural photosensitizers, and specifically on biomolecular sensitizers such as naturally optimized light-harvesting (LH) and photochemical reaction center (RC) protein complexes for converting photon energy into electricity [57].

1.2 Natural Photosensitizers for Solar-to-Electricity Applications

Natural dyes extracted from different biological sources (e.g. anthocyanin, carotenoid, flavonoid, aurone, chlorophyll, tannin, betalain obtained from fruits, flowers, leaves, seeds, barks and various parts of plants or other biological sources) [58], [59] have been previously proposed to be used as sensitizers in DSSCs due to their low cost and environmental friendliness [50], [52], [53], [60]. Previous studies have only investigated the use of anthocyanins [60], [61] flavonoids [62], [63] and carotenoids [43] as plant-sourced photosensitizers in DSSCs.

Hug et al. (2014) [52] collected available data for biological dyes utilized in DSSCs. Bixin, crocetin, crocin, betaxanthin, betalains, mangostin, rutin, neoxanthin, violaxanthin, and lutein were among the investigated natural sensitizers extracted from plant-based sources. More importantly, anthocyanin and carotenoids (e.g. β-carotene) have been identified as one of the promising biomolecular dyes with many studies on their application in bio-DSSCs for photo-to-electricity conversion [52]. Carotenoids are highly light-sensitive pigments [39], [52] due to their conjugated double π-bonds structure with optimal chain length of seven [64] giving an approximated light-absorption range of 400–500 nm [56], [65]. The highest observed performance with single carotenoids in DSSCs was 2.6% with optimal structure length consist of double conjugated bonds [66]. The use of dye blends from the combination of carotenoids/chlorophylls derivatives can increase the

efficiency up to 4.2% as found in earlier works from testing modified chlorophyll/ β-carotene, modified chlorophyll/lutein, modified chlorophyll/violaxanthin, and modified chlorophyll/neoxanthin [67]. Rutin [50] from mangosteen pericarp extract showed the highest efficiency g of 1.17% while extract of rhoeo spathacea showed an efficiency of 1.49% [68]. Further, sicilian prickly pear extract (betaxanthin) was determined to be capable of achieving high efficiency of 2.06% [69].

The expansion of the absorption range of the photoanode photoactive and/or semiconductor layers is feasible to optimize DSSC efficiency [70]. Proteins pigment complexes (PPCs) might be good alternatives to carotenoids since they have higher absorption coefficient, wider absorbance range (300–1100 nm), and higher conversion efficiency [53], [71]. Under 1 sun radiation (100 mW/cm^2), the DSSCs performance have been estimated from reported photovoltaic properties of several biomolecular photosensitizers extracted from plants and other biosources: black rice (anthocyanin) 3.27% [72], capsicum (carotenoid) 0.58% [72], erythrina variegata flower (carotenoid, chlorophyll) 2.06% [72], rosa xanthine (Anthocyanin) 1.63% [72], kelp (chlorophyll) 1.18% [72], organic dye zinc phthalocyanines 4.6% [73] and 6.4% [74], cyanine dyes 4.8% [75] and 7.62% [76], rose bengal (xanthenes) in ZnO-based DSSCs 1.56% [77], coumarin dyes having thiophene moieties in TiO_2-based DSSCs 7.7% [78] and 9% [79].

1.3 Research Motivation and Objectives

Biomolecular carotenoids are one of the most commonly well-known natural hydrocarbon pigments used in DSSCs [39], [52] due to their conjugated double bonds structure which has a light absorption range of 400–500 nm [56], [65]. Carotenoids consist of an optimal chain length of seven conjugated π bonds [64]. The use of carotenoid

pigments from plant sources showed a highest DSSC efficiency of 2.6% [66] where the integration of chlorophyll derivatives (from plant or biological sources) with carotenoids can increase the DSSC efficiency up to 4.2% [67]. A major challenge in optimizing DSSC efficiency is the expansion of the absorption range of the various photoactive and/or semiconductor layers utilized in the structure of the photoanode electrode [70]. In Chapter 2, we have presented a through discussion and review on the available biological pigments which can be used as potential sensitizers in DSSCs for photons-to-electrons conversion.

Thus, this thesis focuses on studying the integration of organic-inorganic 3D $MAPbI_3$ halide perovskites with β-carotene dyes incorporated in a novel naturally-sensitized photoanode in [ETL/Perovskite/HTL] configuration for liquid-state DSSCs. We also focus on understanding the charge transport as well as analyzing diode and photovoltaic characteristics of a perovskite cosensitized carotenoid-based DSSCs. The research aims to explore the possibility of improving photons-to-electrons conversion of β-carotene-based DSSCs *via* $MAPbI_3$ cosensitization.

We also discussed the mechanisms behind perovskite cosensitization leveraging forward charge transport to address the voltage loss arising from ITO/TiO_2 junction's built-in potential in bio-sensitized DSSCs. This includes understanding the photoabsorption mechanisms [80] pertaining cosensitization of β-carotene pigments. Perovskite cosensitizers are believed to improve power conversion efficiency (PCE) *via* enhancing [visible-light absorption, excitons generation, electron injection], and reducing voltage loss at ITO/TiO_2 junction. Expansion in the absorbance spectrum is expected for the cosensitized photoactive layers increasing the probability of absorbing more photons within (400–700 nm) [70] from the available 50% visible-light energy in solar radiation.

1.4 Thesis Summary and Chapters Briefs

This thesis consists of seven chapters complementing each other. Chapter 1 discusses the history behind utilization of DSSCs, available natural sensitizers, and research motivation and objectives.

Chapter 2 discusses the architecture and working mechanism of DSSCs, the state-of-the-art in biomolecular sensitizers and their sources, chemical structures, and advantages, $MAPbI_3$ perovskite as a cosensitizers, and graphene-based counter electrodes.

Chapter 3 illustrates the experimental adopted procedures including deposition of TiO_2 *via* dip-coating or spin-coating techniques, synthesis of $MAPbI_3$ perovskites and their deposition, extraction of carotene dyes, and synthesis of graphene-based counter electrodes.

Chapter 4 discusses the materials characterization of DSSCs electrode active layers using Raman spectroscopy and Scanning Electron Microscopy (SEM) tools. Confirmation of the presence of the deposited electrode materials have been discussed. Also, morphology and cross-section characterization of TiO_2 photoanode is considered.

Chapter 5 shows the selected photoanode designs utilized in device fabrication, and their diode and photovoltaic characteristics investigated from the single-diode model and photoelectrochemical performance parameters.

Chapter 6 discusses UV-Vis absorbance sample preparation and analysis of photosensitizers, hypothesized charge transport mechanism and voltage loss at TiO_2/ITO.

Chapter 7 lays out the concluding remarks, recommendations, and possible future directions for the utilization of natural sensitizers and perovskites in DSSCs.

Chapter 2: Literature Review (State-of-the-Art)

Maddah, H. A., Berry, V., & Behura, S. K. (2020). Biomolecular Photosensitizers for Dye-Sensitized Solar Cells: Recent Developments and Critical Insights. ***Renewable and Sustainable Energy Reviews***, *121*, 109678.

Maddah, H. A., Berry, V., & Behura, S. K. (2020). Cuboctahedral stability in Titanium halide perovskites *via* machine learning. ***Computational Materials Science***, *173*, 109415.

Maddah, H. A., Jhally, A., Berry, V., Behura, S. K. (2020). Highly Efficient DSSCs with 3D Graphene-Based Materials, ***Royal Society of Chemistry***, Under-Review.

2.1 Fundamentals of Dye-Sensitized Solar Cells (DSSCs)

2.1.1 Architecture of DSSCs

A regular DSSC consists of four important components [49], [50], [52], [81]–[83] to initiate the conversion of visible-light photons to electrons. These components and their roles in electron transportation and current generation are briefly (i) photoanode for charge separation/conduction, (ii) counter electrode for electron collection, (iii) photosensitizer for electron injection, and (iv) redox electrolyte for dye regeneration; as shown in Figure 2.1. Transparent conductive oxide (TCO) glass substrate sheet resistance of either indium tin oxide (ITO) or fluorine doped tin oxide (FTO) must be low (<15 to 40 $\Omega/\blacksquare$) with a visible-light (400 to 700 nm) transmission of >80%, facilitating electron injection and transport. Crystallization and annealing of TiO_2 film at 100–500 °C are important for better charge transfer and conduction. Covalently bonded dye molecules forming a monolayer on the semiconductor surface improves photons absorption and e-h pair generation. Dye neutralization occurs *via* liquid or solid (gel) electrolyte when dye molecules receive their missing electrons from reduction of a redox mediator (e.g. iodide and triiodide $[I^-/I_3^-]$ redox couple). A schematic representation of a typical DSSC system with its main components is shown in Figure 2.1.

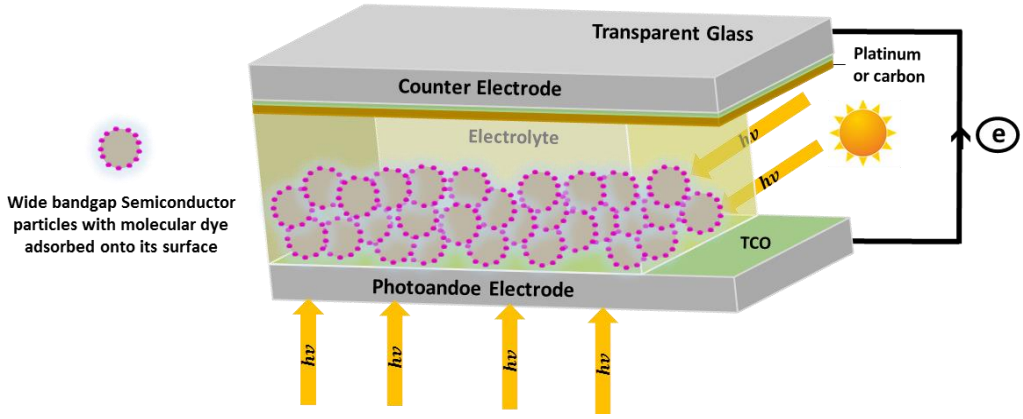

Figure 2.1 Schematic Representation for Typical Components and Architecture of DSSC: Photosensitizer for electron injection; photoanode electrode for charge separation/transport; counter electrode for electron collection; redox electrolyte for dye neutralization [86].

2.1.2 Working Mechanism and Recombination Kinetics

The complete operation cycle of DSSCs is composed of four main steps as follows [49], [50], [81], [84]–[86]

a) Dye excitation (photonic energy absorption): Dye molecules get excited from their ground state (S) to a higher energy state (S*) with light incident due to photon energy, [from the highest occupied molecular orbital (HOMO) to the lowest unoccupied molecular orbital (LUMO)], and then photon-excited electrons (e-h pairs) are generated.

b) Electron injection (transportation): Excited-dye (S*) is oxidized (S^+) and an electron from S* is injected into the semiconductor CB (e.g. TiO_2); then electrons flow through the

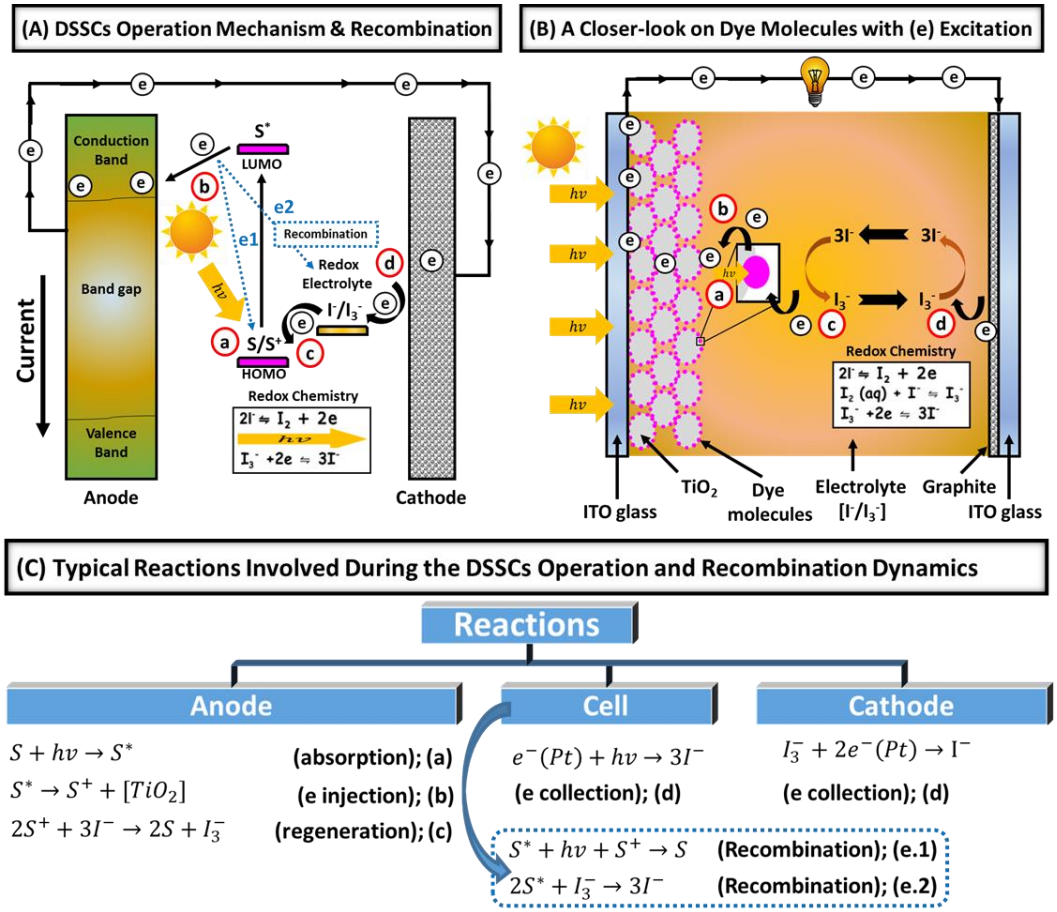

Figure 2.2 DSSC Operation Cycle and Reactions: (A) DSSCs complete operation cycle and recombination dynamics; **(B)** Closer-look on the electron excitation and transport in DSSCs; **(C)** Anode (TiO_2) and cathode (Pt/C) typical redox reactions in a DSSC (electron flow depends on light intensity and trapping-detrapping effect of the surface); Charge transport/regeneration mechanism in (A) and (B): (a) photons energy excite electrons from HOMO to LUMO levels and generate excitons within the dye molecules to (b) inject excited electron into the conduction band of the semiconductor which initiate charge separation/transport of electrons from photoanode electrode to cathode electrode for current generation while (c) electrolyte ensures continuous current generation by neutralizing dye molecules through (d) redox reactions mechanism, (e1) and (e2) describes possible recombination within DSSCs [86].

porous TiO_2 thin film to the ITO glass substrate where they move from anode to cathode through an external circuit in order to complete the cycle and generate current.

c) Oxidized-Dye regeneration (regeneration): Oxidized-dye (S^+) is regenerated by electron donation from the iodide in the electrolyte and redox mediator $[I^-/I_3^-]$.

d) Electrochemical reduction (cathodic reduction): In return, iodide (I_3^-) in the electrolyte and redox mediator diffuses to the counter electrode (cathode) and gets regenerated by reduction of triiodide ($3I^-$) on the cathode.

There are two recombination mechanisms (e1 and e2) in DSSCs which can be viewed as two competing chemical reactions arise form oxidization of both dye molecules and redox electrolyte species simultaneously [84], [85]. Recombination of photogenerated electrons with oxidized dye molecules and/or redox species (I_3^-) takes place within a timescale in microseconds (10^{-6} s) [87], [88]. Asbury et al. [89] estimated the time scale for the electron transfer at the semiconductor/dye (injection) and dye/electrolyte (electrolyte reduction) interfaces in 10^{-15} s (femtoseconds) and 10^{-8} s, respectively; which explains the possibility of neglecting recombination from the faster injection mechanism at the semiconductor/dye interface as compared to recombination dynamics from electrolyte reduction (dye/electrolyte) [84]. A schematic representation of the operation cycle and working principle of DSSCs along with both anode and cathode typical redox reactions and recombination dynamics are illustrated in Figure 2.2(A–C).

e1) Recombination with the oxidized dye: Arise from loss of excited electrons transferring across the semiconductor/dye interface and/or in the semiconductor which consequently recombine with holes in the oxidized dye (acceptors) in presence of visible-light (photocurrent).

e2) Recombination with the oxidized redox electrolyte: Arise from loss of excited electrons transferring across the dye/electrolyte interface which consequently recombine with holes in the oxidized redox species (I_3^-) in the electrolyte in absence of visible-light (dark current).

2.2 Biomolecular Photosensitizers for DSSCs

2.2.1 Sources of Biomolecular Pigments

Bioactive and/or bio-passive pigments are extracted from complex molecules and small particles found in the cytoplasm of various genetics and living bacterial cells. For example, Ribosomes in the bacteria cytoplasm (outside the cell nucleus) is capable of creating different PPCs such that LH2, LH4, and RC as well as producing unique enzymes as hydrogenase for solar-to-energy applications [90]–[92]. Organic carotenoids pigments (yellow to orange-red) are synthesized by photosynthetic organisms in response to various environmental stresses in many bacteria, algae, fungi, and plants to protect the structure of their cells from oxidation damage [93]–[95]. Chlorophyll derivatives synthesized in cyanobacteria, plants, or algae are pigments used to obtain energy from light through photosynthesis [52], [58], [96]. Various reviewed and discussed biomolecular pigments for bio-DSSCs are shown in Table 2.1.

Table 2.1 Bacterial sources of various reviewed and discussed biological pigments for bio-DSSCs

Bio-pigment	Bacterial Source	Ref.
RC Proteins	Rb. sphaeroides (purple non-sulfur bacteria); bacterium RS601 [97]; M. pneumoniae; M. genitalium; B. subtilis; S. sanguinis; H. pylori; C. crescentus; P. aeruginosa and E. coli [98]	[97], [98]
Chlorophyll a (BChl)	Purple bacteria, Heliobacteria, Green sulfur bacteria, Chloroflexi	[99]
Carotenoids	Rhodobacter sphaeroides G1C, Rhodobacter sphaeroides 2.4.1, Allochromatium vinosum and Rhodospirillum rubrum S1	[96]
Chromatophores	Rhodospirillum rubrum [46]; Rhodobacter sphaeroides [100]	[46], [100]
LH2, LH4 and RC proteins pigment complexes (PPCs)	Purple bacteria, specifically, Rhodopseudomonas palustris CQV97 and Rhodobacter azotoformans R7	[101]
Bacteriorhodopsin (BR) proteins	Halobacterium salinarum (purple membrane)	[53]
Bacterioruberin (BR) carotenoids	Halobacterium salinarum (purple membrane) [53]; Haloarcula japonica [102]	[53], [102]
Xanthophylls carotenoids	Hymenobacter sp.[56]; Chryseobacterium sp. [103]	[56], [103]
Lycopene carotenoids	E. coli (Lycopene)	[104]
RC photosystem I trimer (PSI)	Cyanobacteria; thermophilic cyanobacteria Thermosynechococcus	[105]

2.2.2 Chemical Structure of Biomolecular Pigments

Available functional groups, chemical (covalent) and physical bonds, length of the organic hydrocarbon structure chain and the number of conjugated double bonds (n) are some of the parameters that should be considered in the selection of an ideal bio-pigment (e.g. proteins, carotenoids, and Chlorophyll) for DSSCs. Hydrocarbon chains with lots of hydroxyl (–OH) and carboxyl (–COOH) radicals are preferred for strong binding and attachment of dye molecules onto the semiconductor surface resulting in lower electron resistance and facilitated electron injection [96], [106]. Shahzada et al. [107] reported on the possibility of incorporation of phenyl units on both the donor/acceptor moieties within the dyes to reduce recombination.

The chemical structure of a photosensitizer material involves a donor-acceptor-substituted π-conjugated bridge (D-π-A), Figure 2.3. The dye's anchoring group exists in the acceptor part allows dye molecules to chemically attach themselves to the semiconductor surface [108]. Anchoring groups in dye molecules bind to oxide layers *via* a surface hydroxylation chemical reaction [85]. Excited and/or regenerated donor dye electrons flow through the π-bridge to acceptor segments for electron injection. Covalently-bonded dye particles reduce interfacial resistance for the electron flow. Perfect bonding and dye attachment occur from surface interaction between functional groups as carboxyl and/or other peripheral acidic anchoring groups with the semiconductor surface. Earlier works [109] suggest that acidic dye solutions are preferred since de-attachment of dye molecules usually occur around pH = 9.

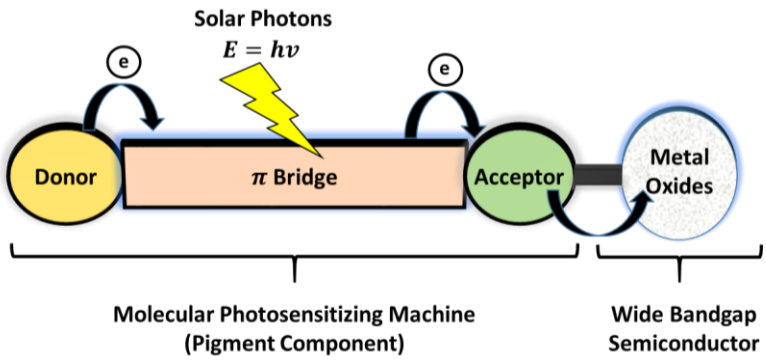

Figure 2.3 Dye-Sensitized Molecular Device: Donor-π-acceptor (D-π-A) structure of an organic dye in DSSCs with a wide bandgap semiconductor photoanode [86].

Conjugated systems such as carotenoids show strong colors or pigments due to the presence of conjugated electrons in their structure (free π-electrons arise from the conjugated double bonds structure which indicates an alternation between single and double bonds in the long hydrocarbon chains resulting in the strong carotenoids colors and the free easily photo-excited electron carriers along the molecular chain for current generation). Photoexcitation initiates electron transition to a higher energy level (π to π^*). An electron transient with photoexcitation from HOMO level to LUMO level according to the selection rules for electromagnetic transitions. Pigments from carotenoids only show up when the number of conjugated double bonds is (n>8) and that system with few conjugations (n<8) only absorb high light energy like UV radiations. Visible-light energy (low energy) can be absorbed by carotenoids constituents that have enough conjugated double bonds (n>11) which typically observed as orange to red pigments. In other words, molecules with more conjugated bonds absorb lower energies of light than molecules with fewer conjugated bonds [110]–[112]. Functional groups, conjugated bonds, and other bonding within the chemically structured long hydrocarbon chains of the reviewed/discussed biomolecular pigments for bio-DSSCs are illustrated in Figure 2.4 [52], [53], [56], [96], [103], [113]–[117].

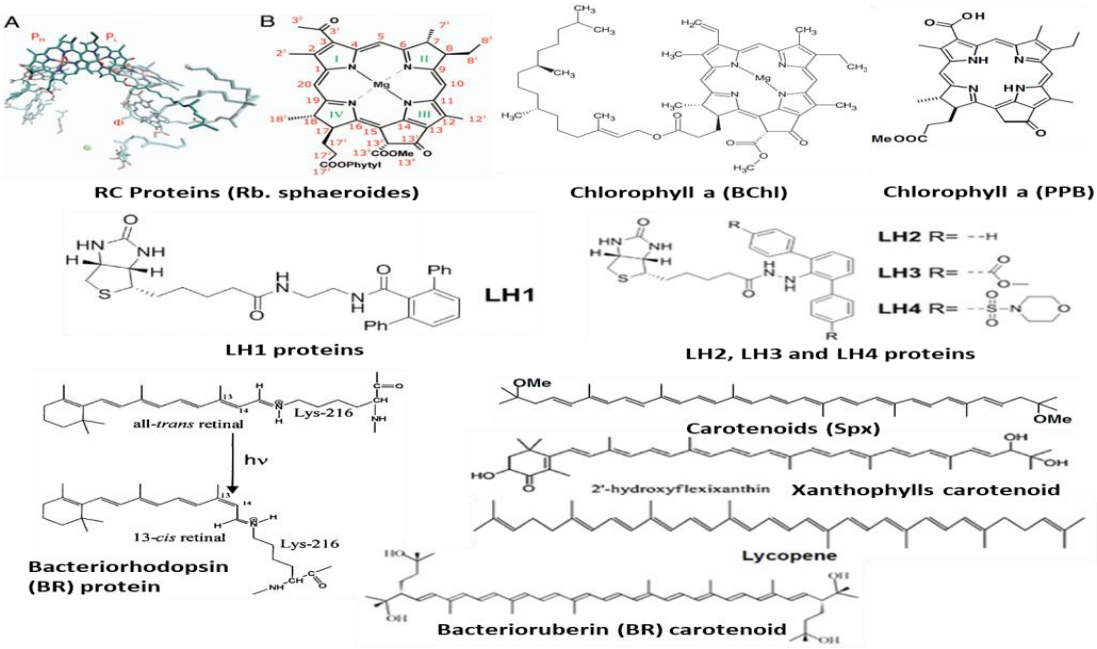

Figure 2.4 Chemical structure of different biomolecular pigments; Adapted from [52], [53], [56], [96], [103], [113]–[117].

2.2.3 Advantages of Bio-Pigments and Photosensitization Requirements

Bacterial pigments have many advantages over the commercial metal-synthetic dyes for DSSCs. Natural pigments from biological sources are promising candidates to be integrated in DSSCs which can be simply installed as rolls in many daily used items such as handbags and clothing as well as building walls, windows and integrated bio-photovoltaics [118], [119]. Advantages of using natural pigments from biomolecular sources include [53], [56], [118], [119] and as shown in Figure 2.5:

(i) Bacteria and their protein complexes and carotenoids are abundant and cost-effective.

(ii) Extraction of bio-dyes is easy, feasible and can be also utilized in large scales (scalable).

(iii) Biological pigments are biodegradable, renewable, and sustainable which makes them very convenient.

(iv) Pigments from bacterial sources are usually noncarcinogenic and pose no health concerns to humans which make them environmental-friendly alternatives.

(v) Biosensitizers can absorb most of the light energy due to their wide absorption spectrum (multi colors and wavelengths).

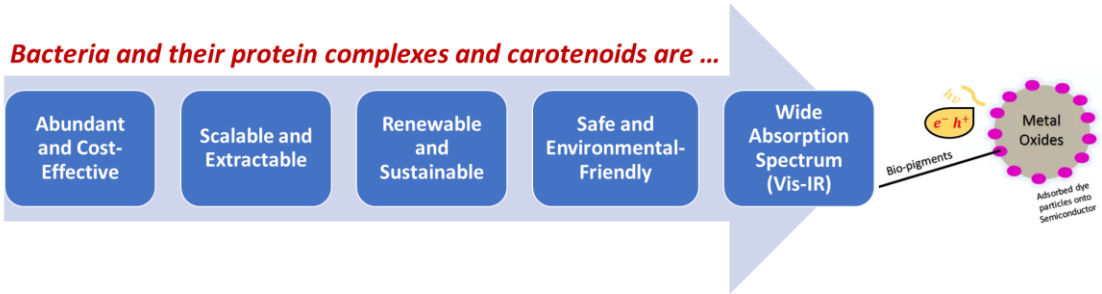

Figure 2.5 Advantages of natural and/or bimolecular photosensitizers over commercial and metal-(Ru)-based sensitizers for DSSCs.

A photosensitizer is considered efficient for DSSCs when it fulfills these requirements [50]: (i) intense visible-light absorption, (ii) strong chemisorption onto the semiconductor surface, (iii) fast electron injection into the semiconductor CB, and (iv) involve several =O or –OH groups to anchor dye molecules onto the semiconductor surface. The pigment's molecular structure, properties (i.e. hydrophilicity/hydrophobicity, solubility, surface chemistry, and stability of dye molecules), surface morphology, self-assembly, aggregation tendency, anchoring groups, and electrolyte interaction with photosensitizers are some of the basic parameters need to be well understood in order to optimize DSSCs performance through using commercial and/or natural photosensitizers [52]. Uniformly dispersed dyes in an optimal solvent prevent dye agglomeration and enhance dye/semiconductor surface interactions required for the attachment of dye acceptor segments, reducing series resistance and improving electron injection at the interfacial contacts.

2.2.4 Current Advancements in Bio-Photosensitized DSSCs

Very few works and minimal progress have been devoted towards the use of bacterial proteins complexes in bio-DSSCs which may be a potential alternative as a natural sensitizer with comparable performance to carotenoids. Thus, several previously designed bio-DSSC systems have been reviewed, studied, and discussed thoroughly with current knowledge and advancements on the selected biomolecular photosensitizers. Biomolecular pigments discussed in this work include reaction center (RC) proteins [97], chlorophyll a (BChl) [96], chromatophores [46], PPCs including LH2, LH4 and RC; mimicking the principles of natural photosynthesis [101], light-harvesting complex II (LHCII) [120], BR proteins [53], [121], Xanthophylls carotenoids [56], [103], Lycopene carotenoids [104], and RC photosystem I trimer (PSI) [105]; in order to understand the biomolecular photosensitizers impact on the DSSCs performance for improved bio-designed DSSCs.

Photosynthetic RC proteins consist of a transmembrane pigment-protein complex across the bacteria which act as a charge separator of the photo-formed electron-hole pairs [97]. Semiconductor/protein films and their functionalization have been recently extensively studied due to their promising role in the development of bioelectronics and bio-photoelectric devices [97], [122], [123]. Yet, researchers are still unable to overcome two major problems: (i) loss of energy due to the formation of the final charge separation state of RC [124], [125]; (ii) charge recombination of the photoinduced electrons which hinders separation of electron-hole pairs that greatly hamper the photoelectric conversion of such RC [97].

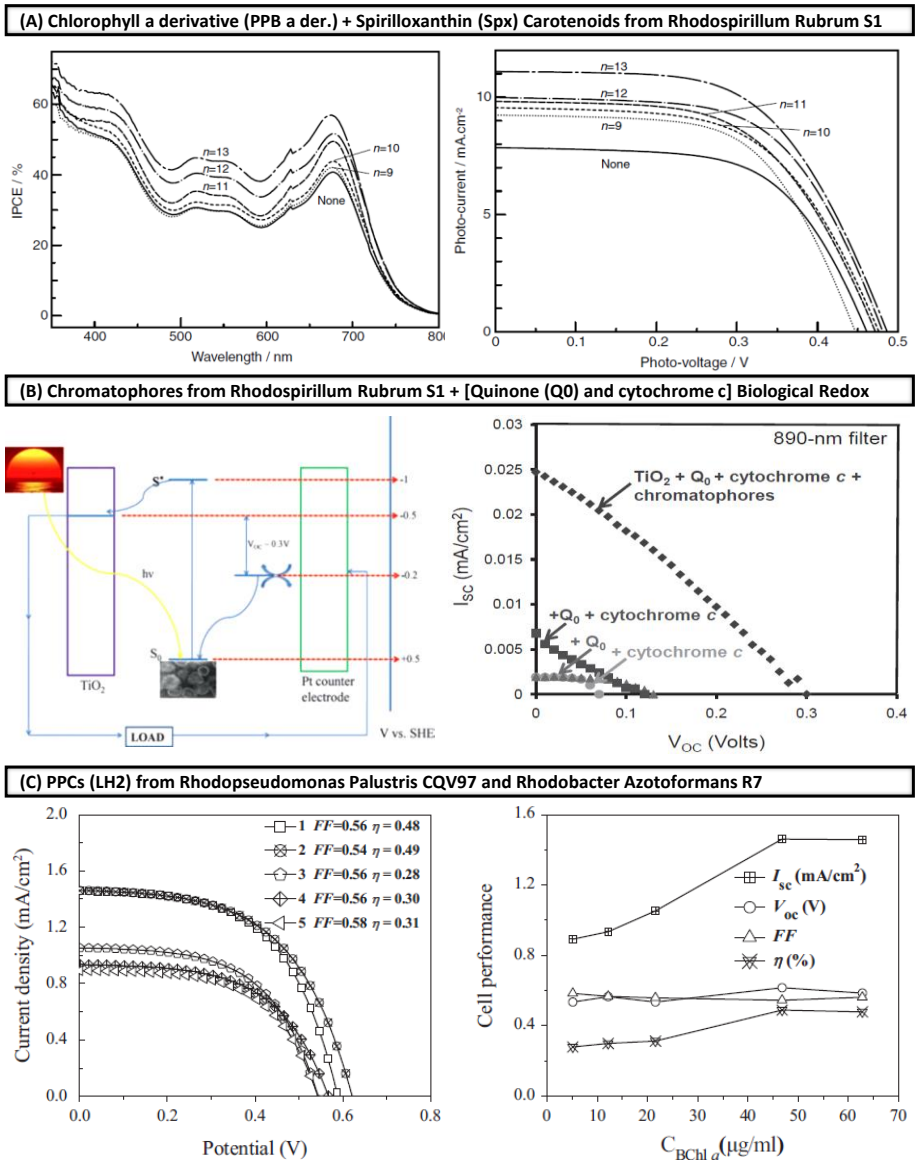

Figure 2.6 (A) IPCE profiles; and I-V curves; for the PPB a der. DSSCs without carotenoids and with a 10% each of carotenoids having n = 9–13; Adapted from [96]; **(B)** Band diagram and I-V curves of various chromatophores sensitized solar cell (CSSC) under near-IR (NIR) illumination; Adapted from [46]; **(C)** I-V curves and photoelectric parameters of DSSCs in different concentrations of LH2; Adapted from [101].

A new type of Bio-DSSC known as photosynthesis DSSCs, which is based on the principle and materials of photosynthesis, has gained much attention from the scientific community for photovoltaic applications [106]. Chlorophyll derivatives are considered as a great biological alternative for traditional dye sensitizers in DSSCs for the conversion of solar energy to electricity [96]. The blending of chlorophyll with photosynthetic pigments like carotenoids has shown much improvements and developments in chlorophyll sensitizing function in DSSCs since carotenoids play a key role in harvesting light energy, protecting chlorophyll layer [126], [127], and forming radical cations for the redox function [128]. Cell performance and IV-curves of various naturally-sensitized DSSCs from literature can be found in Figure 2.6 [46], [96], [101] and Figure 2.7 [53], [56], [103], [104].

From Table 2.2, bio-pigments extracted from protein complexes (LH2, BR, RC) and chlorophyll a derivatives combined with carotenoids showed the highest bio-DSSCs performance for solar-to-electricity applications, with a conversion efficiency of 0.16–0.57% and 4%, respectively. Conversely, Xanthophylls carotenoids isolated from Antarctic bacteria reserved the lowest photoelectric conversion performance of 0.008–0.03% in comparison with other studied biomolecular pigments; the use of co-adsorbents boosted up the performance to 0.03% due to dye strong anchoring capabilities for enhanced charge carriers transport and electron injection.

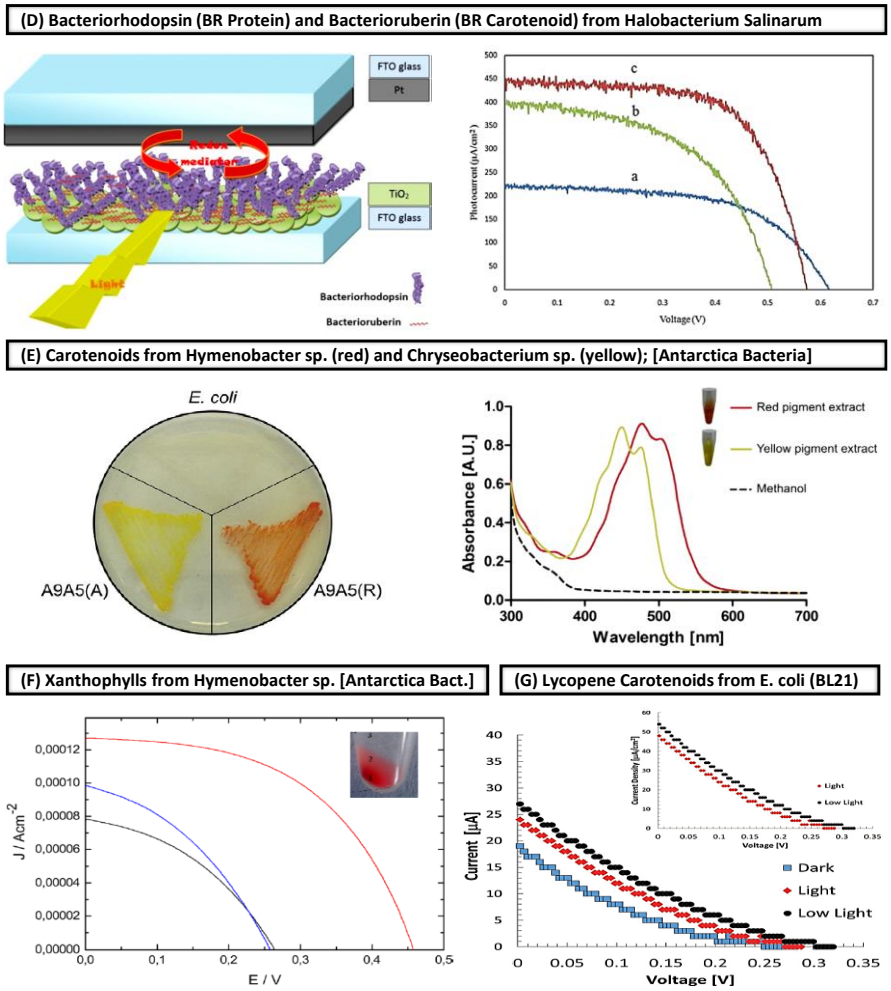

Figure 2.7 **(D)** Bio-DSSC system and I-V curves for the DSSC sensitized with (a) Bacterioruberin (BR carotenoid), (b) Bacteriorhodopsin (BR protein), and (c) a mixture of two pigments; Adapted from [53]; **(E)** Agar plate with pigmented A9A5(R) and A9A5(A) isolates, for the yellow and red pigments, respectively, and E. coli as non-pigmented bacteria; and visible-light absorbance of yellow and red pigments; Adapted from [56]; **(F)** I-V curves for the dye-sensitized cells using different pigments: PURE orange (black line), RAW orange (red line) and cocktail orange + co-adsorbent (blue line); inset: extracted dye from centrifuge with numbers as (1) bacterial pellet, (2) slime, (3) supernatant; Adapted and modified from [103]; **(G)** I-V curves of the bio-PV DSSC using E. coli/Lycopene as a biological sensitizer; Adapted from [104].

Table 2.2 Performance comparison between various reviewed and discussed biological pigments for solar-to-electricity bio-DSSCs under AM1.5 radiation[a]

Bacterial Pigment	J_{sc} (μA cm^{-2})	V_{oc} (mV)	FF	η^b (%)	Ref.
Chlorophyll a (PPB) + Carotenoids (Spx)	11500	-	-	4	[96]
Chromatophores	24.7	300	0.29	0.04	[46]
PPCs (LH2)	1460	620	0.54	0.49	[101]
PPCs (RC)	1240	840	0.55	0.57	[101]
Light-harvesting complex II (LHCII)	800	590	0.58	0.27	[120]
Bacteriorhodopsin proteins and bacterioruberin carotenoids (BRs)	450	570	0.62	0.16	[53]
Xanthophylls carotenoids (yellow)	130	549	-	0.0323	[56]
Xanthophylls carotenoids (red)	200	435	-	0.0332	[56]
Xanthophylls carotenoids (PURE orange)	78	260	0.39	0.008	[103]
Xanthophylls carotenoids (RAW orange)	127	460	0.51	0.03	[103]
Xanthophylls carotenoids (Cocktail)	98	260	0.38	0.009	[103]
Lycopene carotenoids	696	289	-	0.057	[104]
RC photosystem I trimer (PSI)	362	500	0.71	0.08	[105]
Bacteriorhodopsin (BR) protein	620	-	-	0.19	[121]
Bacteriorhodopsin (BR) protein	1008	-	-	0.49	[121]

[a] J_{sc} = Short-circuit current density; V_{oc} = Open-circuit voltage; FF = Fill factor;
[b] η = Incident photon-to-current efficiency (IPCE) = Quantum efficiency (QE).

2.2.5 Bacteria Isolation and Extraction Processes of Bimolecular Pigments

Biomolecular pigments can be extracted from various biomaterials including (i) plant extracts: fruits, flowers, leaves, seeds, peels, and vegetables; (ii) different amino acids and proteins; (iii) nucleic acids DNA, bacteria, and fungi [129]. Water-insoluble fibers, carbohydrates, protein, chlorophyll, and tannins are some examples of targeted materials to be extracted for preparing purified natural dyes. The different common methods used for the extraction of coloring materials are (i) aqueous extraction, (ii) alkali or acid extraction, (iii) microwave and ultrasonic-assisted extraction; (iv) fermentation; (v) enzymatic extraction; and (vi) solvent extraction.

Extraction of natural dyes is a complex process and it requires understanding the nature of the coloring materials and identifying their solubility characteristics. There are several extraction methods which can be used to extract the coloring matter or pigments from natural dye-bearing materials contained in bacteria, plants, and animal constituents.

Water-insoluble fibers, carbohydrates, protein, chlorophyll, and tannins are some examples of targeted materials to be extracted for preparing purified natural dyes. The aqueous extraction is utilized for extracting dyes from plants by breaking the dye-containing materials, sieving undesired residues, soaking materials in water (overnight), boiling and filtering followed by centrifuging to separate residual matter. Alkali or acid extraction is used for extraction of dyes from flowers as in tesu (buteamonosperma), some flavone dyes (using acidified water) and for dyes having phenolic groups (soluble in alkali); acid hydrolysis occurs from addition of the acid or alkali facilitating the hydrolysis of glycosides in the dyes which can be later precipitated. Microwave and ultrasonic assisted extraction require treatment of dye-containing materials (e.g. plants) in water or any other solvent in the presence of ultrasound; creation/collapse of bubbles increases the extraction efficiency due to applied stress on materials. Fermentation utilizes produced enzymes from the atmosphere/surrounding materials as in harvesting indigo leaves soaked in water for about 10–15 h (glucosideindican breaks down into glucose and yellowish indoxyl by the indimulsin enzyme). Enzymatic extraction uses enzymes including cellulase, amylase, and pectinase for the extraction of dyes from complex plant tissues containing cellulose, starches, and pectins as binding materials. Solvent extraction requires organic solvents (e.g. acetone, chloroform, ethanol, and methanol) or water/alcohol mixtures to extract water-soluble and alcohol-soluble substances from plants which are then purified [130]. Table 2.3 shows isolation and extraction processes used for separating bacteria and obtaining bacterial-based biomolecular pigments in the various reviewed studies on bio-sensitized DSSCs.

Table 2.3 Isolation/extraction processes adopted in extracting bacterial-based pigments from various reviewed and discussed biomolecules for solar-to-electricity bio-sensitized DSSCs.

Bacterial Pigment	Remarks on Bacteria Isolation and Pigment Extraction	η (%)	Ref.
Chlorophyll a (PPB) + Carotenoids (Spx)	Spirilloxanthin (Spx) was isolated from rhodospirillum rubrum S1. bacteriochlorophyll and lipids were removed by washing cells with methanol, centrifuged, washed with acetone, and centrifuged again. Resultant cells were washed with benzene and centrifuged (3 times) to completely extract the carotenoids after fractionating benzene solution against NaCl aqueous. Benzene layer containing carotenoids was filtered using low-pressure liquid chromatograph.	4	[96], [131]
Chromatophores	Cell growth was done by keeping Rsp. rubrum strain S1 to grow for 3 days under 1-sun condition and at 30 °C. Chromatophores were isolated from French pressure through rate-zone sedimentation on sucrose density gradients, then isolated mixture was centrifuged and resuspended in 0.1 M Na_2PO_4. Purified membrane (lipid) fractions were obtained from trichloroacetic acid-precipitated by two chloroform-methanol extractions.	0.04	[46]
PPCs (LH2)	Bacterial PPCs were isolated from collected sand using StrainCQV97 and R7 cultured anaerobically in modified Ormerod medium at 30 °C for 1 h, then PPCs were purified with ammonium-sulfate fractionation (DEAE-52 anion-exchange) and gel-filtration chromatography.	0.49	[101]
PPCs (RC)	Pigment Extraction as PPCs (LH2).	0.57	[101]
Bacteriorhodopsin proteins and bacterioruberin carotenoids (BRs)	Two strains of H. salinarum, NRC-1 and R1, were used for extraction of bacteriorhodopsin and bacterioruberin, respectively. Strain cells were ground with quartz powder, extracted with ethanol, ether, and 15% NaCI aqueous solution to separate organics. The organic layer was dried over anhydrous sodium sulfate, loaded with a benzene solution on a silica gel column. Bacterioruberin pigments were eluted with acetone:benzene (42:58), pooled and concentrated under reduced pressure. The bacterioruberin was dissolved in acetone and stored under N_2 gas in the dark at −30 °C. Bacteriorhodopsin was isolated by other standard methods reported in literature.	0.16	[53], [132]
Xanthophylls carotenoids (yellow)	Bacteria isolation was carried out by suspending collected soil containing biomaterials in distilled water. Samples were stirred vigorously, incubated at 28 °C for 1 h, and seeded on R2A agar plates for two days. The streak plate method was used to obtain pure cultures where selected isolates were identified by 16S rRNA sequencing. Pigments were extracted using DNeasy® Blood & Tissue Kit (Qiagen) with the amplification steps including initial denaturation final extension.	0.0323	[56], [133], [134]
Xanthophylls carotenoids (red)	Pigment Extraction as xanthophylls carotenoids (yellow).	0.0332	[56], [133], [134]
Xanthophylls carotenoids (PURE orange)	Xanthophylls pigments were extracted from cells grown in R2 medium, centrifuged to discard the uncolored supernatants while suspending pellet and slime phases in 98% ethanol, and then heated at 60 °C for 1 h until reddish pigments turned to orange. Samples were then centrifuged again, and supernatants were filtered with sterile membrane. Extracted carotenoids from hymenobacter sp. were kept at −20 °C in darkness for future	0.008	[103]

	use.		
Xanthophylls carotenoids (RAW orange)	Pigment Extraction as xanthophylls carotenoids (PURE orange).	0.03	[103]
Xanthophylls carotenoids (Cocktail)	Pigment Extraction as xanthophylls carotenoids (PURE orange).	0.009	[103]
Lycopene carotenoids	No isolation was there, instead cloning of bacterial strains was carried out within E. coli BL21 cells to synthesize and overproduce the photoactive pigment lycopene.	0.057	[104]
RC photosystem I trimer (PSI)	Trimeric PSI was isolated from the thylakoids of the thermophilic cyanobacteria thermosynechococcus elongates. PSI was isolated from frozen cells, resuspended in wash buffer and sorbitol, adjusted to a specific chlorophyll a content, and then homogenized. Lysozyme was added to the mixture prior incubation for 2 h at 37 °C with shaking. Resultant mixture was centrifuged to discard supernatant; remaining pellet phase was resuspended, passed twice through French Press (Amino) at a cell pressure of 20,000 psi, and washed with 3 M NaBr. Density gradient centrifugation was performed prior to collection of the lowest green bands of pooled PSI samples diluted with dialysis against MES and anion exchange column.	0.08	[105], [135]

2.2.6 Bandgap Energies of Biomolecular Dyes

In biomolecular organic dyes, two typical energy levels exist for electrons called LUMO and HOMO levels. Under illumination, dye molecules get excited allowing electron injection into the CB of the semiconductor as long as LUMO energy level is closer to the vacuum level and higher than the semiconductor CB. Effective electron-diffusion and high dye reduction rates occur with the existence of large energy difference between dye-HOMO and electrolyte-redox-potential [69]. Dye light-absorption abilities depend exclusively on HOMO/LUMO energy potential levels and other unknown parameters. HOMO/LUMO molecular orbitals and electron distribution within the dye [136], [137] can be utilized to predict quantum chemistry and electron transport to/from the D-π-A dye conjugated structures [138], [139]. Electrochemistry calculations show that dye reduction and oxidation potentials occur at the excited state (LUMO) and the ground state (HOMO), respectively. Determination of redox potential can be attributed to the dye bandgap

calculated from electrochemical methods and/or UV-Vis absorbance (Tauc plots). Electron delocalization occur with minimum absorbed photon energy yielding in the excitation of the ground state populations (HOMO), delivering electrons to the LUMO moieties through biomolecular conjugated-bridges [140]. Bandgap energies can be calculated from the difference between HOMO to LUMO levels ($E_g = E_{LUMO} - E_{HOMO}$), that is typically desired to be lower than the semiconductor bandgap (e.g. TiO_2 or ZnO; <3.2 eV). For example, for cyanine dyes HOMO (–5.73 eV) and LUMO (–3.82 eV) at 590 nm which is equivalent to a molecular cyanine bandgap of 1.91 eV [76]. Table 2.4 shows the theoretical HOMO/LUMO energy levels for different biomolecular dyes and their corresponding bandgaps (eV) required for electron photoexcitation.

Theoretical-average HOMO/LUMO gap energies of 2.46, 5.22, 4.13, 1.13, 3.15, 2.22 eV were calculated (from Table 2.4 and the given values found in literature) and observed for anthocyanin, carotenoid, chlorophyll, cyanine, xanthene, and coumarin, respectively. Correlating the determined biomolecular bandgap energies with the dye performance of anthocyanin 1.67–3.27% [72]; carotenoid 0.58% [72]; chlorophyll 4.6% [141]; cyanine dyes 4.8–7.62% [75], [76]; xanthenes 1.56% [77], coumarin dyes 7.7–9% [78], [79] give us a complete understanding for the role of HOMO/LUMO gap energy. Low amounts of energy band gap result in easy electron excitation and e-h pair generation in the HOMO levels; hence, anthocyanin, cyanine, and coumarin dyes showed the highest bio-DSSC efficiency >3.27% and up to 9% due to the low HOMO/LUMO energies <2.46 eV. On the contrary, both carotenoid and xanthenes dyes showed low cell performance <1.56% due to their high bandgap energies >3.15 eV. However, the bandgap is not the only parameter controlling the dye absorbance rate, since an exception was noticed with

chlorophyll dyes where high performance is observed with high bandgaps which may be explained by the 'relative state of HOMO-level vs. SHE and its correspondence to the CB-level vs. SHE' or by other unknown phenomena such as impact of existing functional groups, dye/semiconductor interactions, and bonding mechanisms changing the photosensitization performance.

Table 2.4 HOMO/LUMO energy levels of different and common biomolecular dyes

Pigment Category and/or TiO_2	Theoretical/ Experimental	HOMO-to-LUMO Energy (eV)[a]		Ref.
		HOMO	LUMO	
Anthocyanin	Theoretical	2 – 2.78		[142]
	Experimental	2.18 – 3.26		[142]
Carotenoid	Theoretical	2.2 – 7.3		[143], [144]
	Experimental	N/A		[143]
Chlorophyll	Theoretical	4.14		[145]
	Experimental	1.82		[145]
Cyanine	Theoretical	1 – 1.5		[146] [140]
	Experimental	1.5 – 2.2		[146]
Xanthene[b]	Theoretical	1.74 – 3.95		[147]–[149]
	Experimental	N/A		[147]
Coumarin	Theoretical	1.25 – 2.93		[150], [151]
	Experimental	2.08 – 3.49		[150]
TiO_2	Theoretical	4.18		[151]
	Experimental	3.49		[151]

[a] HOMO/LUMO energies determined from theoretical time-dependent and density functional theory (TD-DFT) studies as reported in the literature; [b] Xanthene in Spiro[fluorene-9,9′-xanthene] hole-transporting materials (SFX-based HTM) used in perovskites solar cells.

2.3 $MAPbI_3$ Perovskite as a Co-Sensitizer in DSSCs

Organic-inorganic hybrid perovskite crystals have been widely used in optoelectronic devices such as solar cells and light-emitting devices [152]–[154]. Typical perovskite materials have the chemical formula ABX_3 where A refers to an organic and/or inorganic cation with +1 charge (e.g. Cs^+, methylammonium (MA^+), and Rb^+), B is a metal cation with +2 charge (e.g. Pb^{+2}, Hg^{+2}, Zn^{+2}, Mg^{+2}, and Cd^{+2}) and X is a halide anion with

-1 charge (e.g. F^-, Cl^-, Br^- and I^-) [155]–[157]. Ideal ABX_3 perovskites (e.g. $MAPbI_3$) consist of a cubic array with three-dimensional A-site corners sharing BX_6 octahedral units in which A-site cation is surrounded by 12 equidistant X anions; The A-site cations fill the cuboctahedral cavities and B-site cations occupy the center of the octahedral sublattice and have 6 nearest X-anion neighbors [158], [159] (see Figure 2.8, [160]). Perovskites have enabled outstanding achievements in the field of solid-state photovoltaics including the achievement of high photovoltaic conversion efficiency (PCE > 22.1%) [153], [154], [161], which is already close to the theoretical Shockley-Queisser limit of 33.5% [162] for a single-junction silicon solar cell.

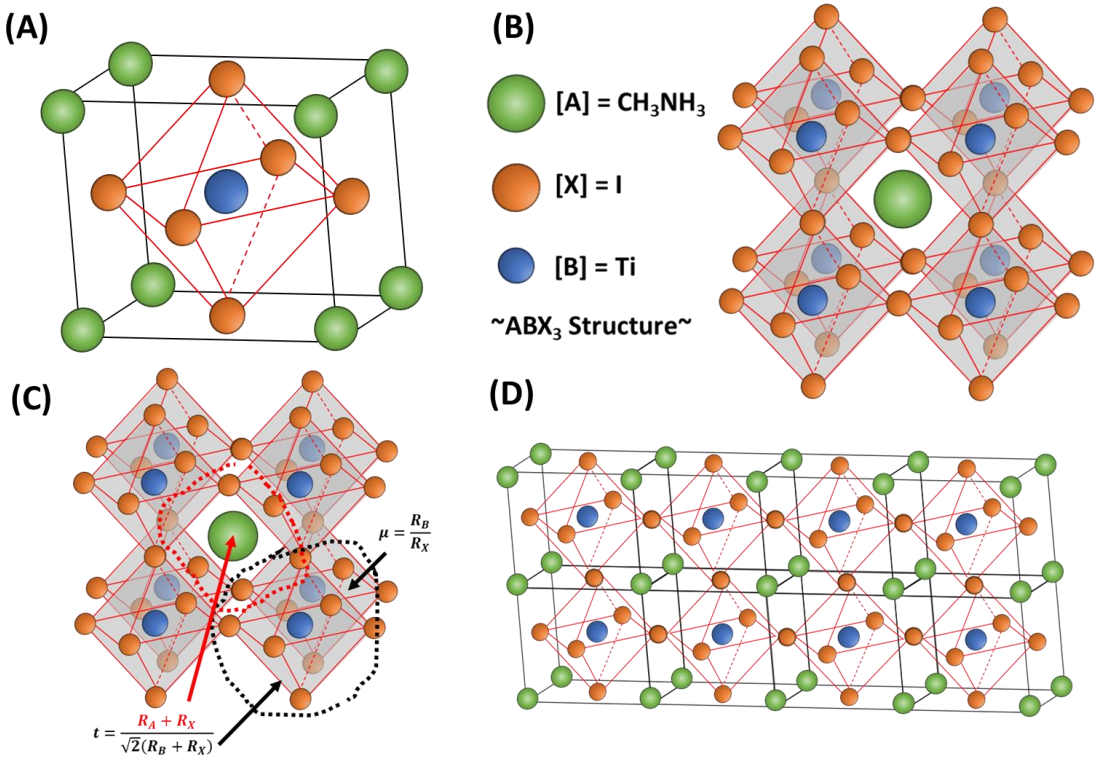

Figure 2.8 Ti-based perovskites (ABX_3) typical crystal structure: **(A)** A cubic structure unit cell; **(B)** MA^+ cation occupying an A-site and surrounded by eight octahedral structures; **(C)** Role of stability factors in determining the possibility of MA^+ and Ti^{+2} cations to occupy A-sites and B-sites, respectively, based on the involved elements ionic radii; **(D)** The ideal cubic structure for $MATiI_3$ when (t = 1) indicating a perfect cation fit; [160].

Moreover, perovskite materials have many other advantages for photovoltaic and optoelectronics applications [8], [10], [163]–[165] including (i) excellent light absorption capabilities; (ii) high charge carriers mobility including both electron and hole mobilities; (iii) outstanding transport properties due to long diffusion lengths; (iv) tunable bandgap structure (bandgap of 3D $MAPbI_3$ is approximately 1.55 eV); (v) easily synthesized with low temperature solution processability; (vi) highly crystallizable at low annealing temperature; and (vii) inexpensive and highly efficient for power conversion in photovoltaic applications [9], [153], [166]. $MAPbI_3$ planar three-dimensional perovskite films can be easily fabricated by spin-coating a mixture of methylammonium iodide (MAI) and lead iodide (PbI_2) with further post-annealing for crystallization to form the covalently bonded perovskite structure ABX_3 [167].

Perovskite cosensitization [168]–[171] and/or absorbance expansion are some of the promising techniques utilized for improving electron injection and photoanode sensitization, respectively. Enhanced photoanode sensitization and widened photoanodes absorption spectrum [172] are attainable by utilizing low-bandgap energy cosensitizers [168]–[171] such as organic-inorganic hybrid methylammonium lead iodide ($MAPbI_3$) semiconductor perovskite crystals [10], [160] owing to their high visible-light absorption (α=0.7×10^7 cm^{-1}) [12], bandgap tunability (E_g=1.5~2.43 eV) [166], high charge carriers mobility (>5 cm^2 V^{-1} S^{-1}) [173], long diffusion lengths (>100 nm) [174], and easy processability [175], [176].

In DSSCs, perovskites are utilized as cosensitizers to harvest visible light energy from the enhanced absorption coefficient as well as the covered visible-spectrum range. Kojma et al. [168] combined the $MAPbX_3$ in the photoanode in TiO_2-based electrode

utilized in DSSCs ($CH_3NH_3PbX_3/TiO_2$) to achieve the highest power conversion efficiency of 3.81% using Ru dyes. High efficiency of 6.54% was also achieved from using $MAPbI_3$ quantum-dot-sensitized 3.6 mm-thick TiO_2 photoanode films under AM 1.5G and 1 sun intensity (100 mW cm^{-2}) [169]. Another study investigated the use of $CH_3NH_3PbBr_3$ as a cosensitizer to Ru-complex (Z907) in TiO_2-based DSSCs which improved the visible-absorbance with a maximum performance of 3.4% [170]. The substitution of the liquid electrolyte with a solid-state hole transport layer (HTL) incorporated into the perovskite-sensitized rutile TiO_2 nanorods increased the PCE up to 9.4% (and by 15% in a solid-state mesoscopic DSSC) [177] where TiO_2/perovskite act as the electron transport layer (ETL) [171].

2.4 Graphene-Based Counter Electrodes for DSSCs

Pristine graphene is an atomically-thick layer of sp^2-hybridized carbon arranged in hexagonal crystal structure [178]. Graphene-based materials, with their exceptional electrical, optical, and mechanical properties, have been previously incorporated into each aspect of a DSSC [178]. Interestingly, this amazing material can be derived from graphite (*via* top-down approach), which is economical and naturally abundant [179]. Wang et al. (2012) [180] utilized graphene-based composites in DSSCs owing to its excellent conductivity and high electrocatalytic activity. The hexagonal "honeycomb" two-dimensional sp^2 carbon atoms [181] possesses high carrier mobility (200,000 cm^2 V^{-1} s^{-1}) [182], high specific surface area (2600 m^2 g^{-1}) [183], and high optical transparency (97.7%) [184]; making graphene a promising material to be utilized as electrodes for efficient and practical DSSCs. Graphene sheets have been typically produced either by mechanical exfoliation *via* repeated peeling of highly ordered pyrolytic graphite (HOPG) or by

chemical oxidation of graphite (top-down approach) [185]. Table 2.5 shows the performance of different graphene-based DSSCs from previous studies, based on their cell configuration design with graphene-based counter electrodes.

Table 2.5 Performance comparison of various DSSCs: Efficiency and photovoltaic parameter values observed in previously designed DSSCs with different graphene-based counter electrodes[a]

Cell Configuration	V_{oc} (V)	J_{sc} (mA/cm^2)	FF (%)	η (%)	Ref.
FTO/TiO_2/N719/Graphene/[I^-/I_3^-]/FTO	0.74	16.99	0.54	6.81	[186]
FTO/TiO_2/N719/Graphene/[I^-/I_3^-]-(AN-50)/FTO	0.54	14.30	0.65	5.69	[187]
ITO/TiO_2/N719/[I^-/I_3^-]/[Graphene/PEDOT-PSS]/ITO	0.72	12.96	0.48	4.50	[188]
FTO/TiO_2/N719/[I^-/I_3^-]/[Graphene/PANI]/FTO	0.68	13.28	0.67	6.09	[189]
FTO/TiO_2/N719/[I^-/I_3^-]/[Graphene/PEDOT]/FTO	0.77	12.60	0.63	6.26	[190]
FTO/TiO_2/N719/[I^-/I_3^-]/[Graphene/Pt]/FTO	0.71	15.20	0.71	7.66	[191]
FTO/TiO_2/N719/[I^-/I_3^-]/ [Graphene/Pt]/FTO	0.79	12.06	0.67	6.35	[192]
FTO/TiO_2/N719/[Graphene/$Ni_{12}P_5$]/[I^-/I_3^-]/FTO	0.74	12.86	0.61	5.70	[193]
FTO/TiO_2/N719/[Graphene/$Ni_{12}P_5$]/[I^-/I_3^-]/FTO	0.70	12.88	0.52	4.70	[193]
ITO/TiO_2/N719/[Graphene/MWCNTs] [I^-/I_3^-]/ITO	0.72	8.95	0.70	4.46	[188]
FTO/TiO_2/N719/[Graphene/MWCNTs] [I^-/I_3^-]/FTO	0.75	16.05	0.63	7.55	[194]
FTO/TiO_2/N719/[I^-/I_3^-]/[Graphene-(HSG-12 h)]/FTO	0.77	27.20	0.37	7.80	[195]
ITO/TiO_2/N719/[I^-/I_3^-]-(Z946)/[PDDA@ERGO]/ITO	0.69	18.77	0.74	9.54	[196]
ITO/TiO_2/N719/[I^-/I_3^-]-(Z952)/[PDDA@ERGO]/ITO	0.65	15.19	0.76	7.66	[196]
ITO/TiO_2/N719/[I^-/I_3^-]-(Z946)/[PDDA@ERGO]/Pt/ITO	0.69	18.11	0.74	9.14	[196]
FTO/TiO_2/N719/[GNs@ZnO]/[I^-/I_3^-]-(BMII)/FTO	0.76	21.70	0.67	8.12	[197]
FTO/TiO_2/N3/NDG/[I^-/I_3^-]/FTO	0.69	15.76	0.64	7.01	[198]
FTO/TiO_2/N719/Graphene-(0.15wt.%)/[I^-/I_3^-]/FTO	0.75	15.46	0.68	7.88	[199]

[a] PANI: Polyaniline; PEDOT: Poly(3,4-ethylenedioxythiophene); MWCNTs: Multi-walled carbon nanotubes; HSG: honeycomb-structured graphene; PDDA: Poly(diallyldimethylammonium chloride); ERGO: Electrochemically reduced graphene oxide; GNs: Graphene nanosheets; NDG: Nitrogen doped graphene.

Counter electrodes (CEs) in DSSCs play a critical role in determining the cell efficiency depending on their abilities to collect electrons coming from the photoanode through the external circuit. A number of parameters should be investigated for the selection of optimal and scalable CEs: (i) sheet resistance; (ii) catalytic activity; (iii) chemical stability; and (iv) cost [49], [180], [200]–[204]. For an optimized cell, the CE sheet resistance must be as low as possible to facilitate electron transport, the CE catalytic

activity should be very high for effective chemical reduction of redox species, and the CE materials must possess a noble-like behavior as in Pt electrodes for corrosion stability [205]–[208]. However, Pt is highly expensive for large-scale applications due to its scarcity. As such, the development of Pt-free CEs should be pursued to have graphene-based cost-effective and scalable CEs [180].

Chapter 3: Synthesis/Deposition of Electrode Materials for Cell Architectures

Maddah, H. A., Aryadwita, L., Berry, V., & Behura, S. K. (2020). Perovskite Cosensitization for Reduced Voltage Loss in Naturally-Sensitized Solar Cells, ***Nano Energy,*** Under-Review.

3.1 Introduction

Fabrication and designing of a DSSC requires three main parts: (i) support: a layer of transparent conducting oxide called the ITO or FTO coated on two glass sheets, (ii) electrodes: this include the anode as Dye/TiO_2 electrode (meso porous with a high surface area) coated on ITO glass and also a counter electrode from platinum or graphite deposited/taped on the cathode glass, and (iii) electrolyte: iodide/triiodide acting as a redox mediator [209], [210]. To prepare photoanode electrodes, pre-purchased TiO_2 nano-powders paste was used directly for drop-casting and/or dip-coating on the ITO glass. Then, TiO_2 were prepared to be annealed at 400°C for 30 min and left to cool at room temperature to have the anatase structure. After calcination, dye deposition was achieved *via* soaking ITO/TiO_2 overnight in a pre-extracted and purified β-carotene solution to sensitize the semiconductor material and allow visible light absorption. To prepare the counter (positive) electrodes, conductive ITO glass sheets sides were coated with graphene-based materials using Hummers method [211]. The drop-casted graphene oxide was then annealed at 200°C for 3 h to have a thin rGO conductive layer as counter electrode for electron collection in DSSCs. This thin carbon layer serves as a catalyst for the tri iodide-to-iodide regeneration reaction. For long-lasting results, the carbon-coated counter electrode was annealed at 450°C for a few minutes, washed with ethanol, and gently dried before assembling the electrodes [209], [210].

3.2 TiO_2 Deposition (Dip-Coated or Spin-Coated) on ITO Photoanodes

Numerous ITO 1'' conductive glass sheets (~23 Ω/■) were thoroughly cleaned with IPA (sonicated for 15 min) and followed by DI water washing prior being used for electrodes fabrication. TiO_2 nanoparticles paste from (Sigma Aldrich, USA) was used directly without further treatment. Adhesive scotch tape was applied on the conductive sides to have a 2 cm x 1.5 cm exposed surface area ready for TiO_2 dip-coating (or spin-coating). After covering the backside with tape, all the four ITO sheets were dip-coated (or spin-coated @ 3000 rpm) successively using the TiO_2 and removed immediately to remove the excess amount of the deposited semiconductor. The glass sheets were then kept to dry in the air for 5 min to become ready for annealing the ITO/TiO_2 structure at 400 °C for 30 min [212]. TiO_2 crystallization was achieved from the high sintering temperature which converted the liquid-like nanostructure to a defined solidified crystal structure creating a layer of a wide bandgap semiconductor (3.2 eV) [48] atop of the ITO (Figure 3.1). The ready and crystallized ITO/TiO_2 were removed from the hot plate and stored in a dry petri dish to be used later in fabricating our photoanode structures.

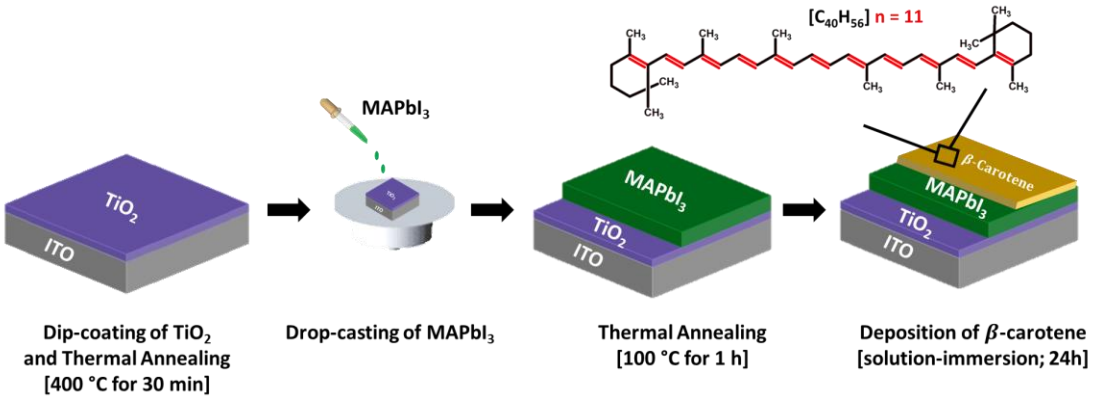

Figure 3.1 Experimental steps used in the fabrication of [ITO/TiO_2/$MAPbI_3$/β-carotene] photoanode heterostructure (from left to right), with a schematic showing the chemical structure of β-carotene natural sensitizers and conjugated bonds (n=11).

3.3 Synthesis of $MAPbI_3$ and Deposition

The precursor solution for $MAPbI_3$ synthesis was prepared as reported in previous literature [175], [176]. Briefly, $MAPbI_3$ was synthesized by mixing 2 g of PbI_2 powders with 0.5 g of MAI powders in a small beaker (50 mL) with continuous addition of 5 mL of DMF using a pipette under the atmospheric condition and at room temperature (T=23 °C). The mixed solution was then heated on a hot plate for 1 h at 60 °C and then continuously stirred at a constant rate using a magnet stirrer. The pre-prepared precursor solution of $MAPbI_3$ was drop-casted (2-3 drops) on the four sintered ITO/TiO_2 (2 cm x 1.5 cm) electrodes and then annealed on the hot plate at 100 °C for 1 h in order to obtain the solidified crystal structure for $MAPbI_3$ and obtain the heterostructure ITO/TiO_2/$MAPbI_3$ (Figure 3.1).

3.4 THF-Extraction of β-Carotene Sensitizers and Deposition

From literature, β-carotene was tested for its solubilization in different 18 organic solvents; Craft et al. found out the solubility of β-carotene carotenoids is greatest in tetrahydrofuran (THF) (10,000 mg/L), followed by dichloromethane (6000 mg/L), benzene and toluene (4000 mg/L), chloroform (2000 mg/L), acetone (200 mg/L), and ethanol (30 mg/L) [213]. Hence, we used THF organic solvent to solubilize our non-treated lab-grade β-carotene powders (Sigma Aldrich, USA). Dye extraction and purification were carried out like the stepwise purification process of the mangosteen pericarp extract reported in earlier work [68].

Pre-purchased β-carotene powders (1.5 mg) was added to THF organic solvent (50 mL) under continuous stirring for 1 h in ambient conditions. Dye extraction from carotenoid solids was confirmed from the observed change in the THF color which turned

into a yellowish/reddish color. THF solvent was then filtered using a vacuum filtration system to discard precipitates. Dried filtrate solids containing the THF-extracted pigments were washed with water under vigorous stirring (50 mL) and filtered again (step-wise purification) to get the THF-H_2O-extracted carotenoid precipitates. Purified carotenoids were then washed finally with THF (50 mL) to obtain "Solution A" used for dye deposition onto the photoanode. The complete step-wise pacification process flowchart and dye-coated TiO_2 are shown in Figure 3.2. Solution A was used to provide sensitization after being concentrated at 60 °C (THF volume was reduced to 25 mL). All sintered photoanodes were soaked in a petri dish of THF-β-carotene concentrated solution for >24 h to ensure dye deposition (Figure 3.1) and molecules anchoring onto the semiconductor.

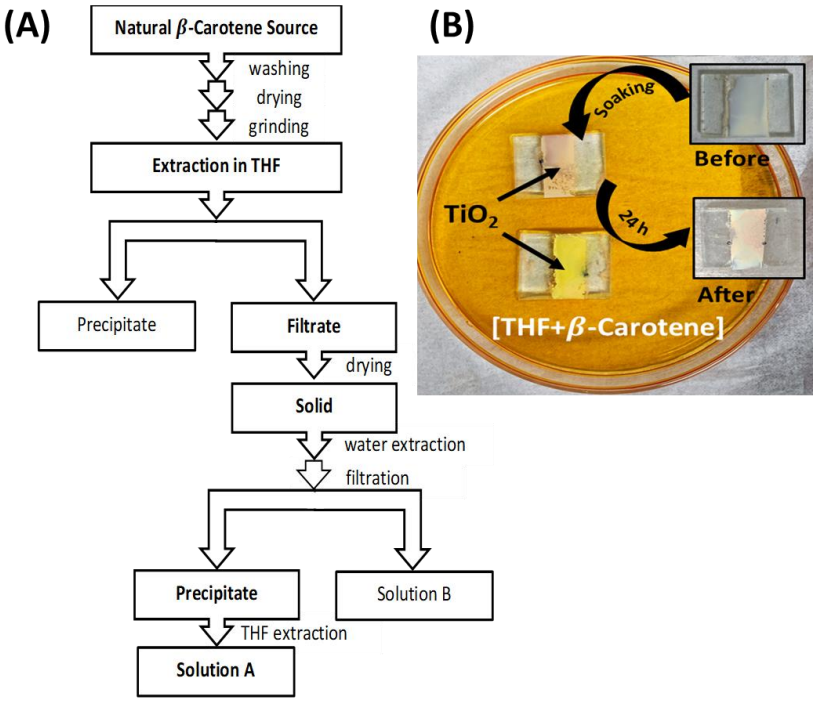

Figure 3.2 (A) Flowchart showing the extraction procedure adopted for the step-wise purification and THF extraction of β-carotene; **(B)** Crystallized TiO_2 dip-coated thin-film (2 cm x 1.5 cm) on ITO glass before and after β-carotene overnight deposition.

3.5 Synthesis of Graphene Oxide and their Reduction for rGO-Based Cathode

Modified Hummers Method [211], [214], [215] was used for the synthesis of graphene oxide (GO). Briefly, we initiated GO synthesis by mixing 1 g of natural carbon-based graphitic flakes with 0.5 g of sodium nitrate ($NaNO_3$) in a 23 mL of concentrated sulfuric acid (H_2SO_4). Addition of 6 g of potassium permanganate ($KMnO_4$) as oxidizing agent to the suspension was carried out subsequently under continuous stirring and ice-bath cooling for 1 h to maintain the suspension below room temperature (~ 0 $^{\circ}$C). The $KMnO_4$ oxidant can break the van der Waals interlayer forces exist between the graphene layers creating graphene-based suspension. The mixture was then stirred for 12 h at 35 $^{\circ}$C until the suspension became dark green. The exothermic reaction was then terminated (the excess $KMnO_4$ was also eliminated) by the addition of 500 mL of deionized water (DI water) and 3 mL of 30% hydrogen peroxide (H_2O_2).

Undesired ions/particulates were removed through washing the suspension with a 1:10 hydrochloric acid (HCl) to DI water (25:250 mL) and then dialyzed at room temperature (~ 23 $^{\circ}$C) in a DI bath overnight, while changing the DI water every 1 h during the first 6 h to remove undesirable metal ions, acids, and other functional groups responsible for the high suspension acidity [211], [214]–[216]. The resultant GO suspension become much pure with a low acidity (pH ~ 6) owing to the elimination of acidic ions from the produced mixture (without addition of sodium hydroxide or any other hydroxyl ions to the suspension). The pH of GO suspension is believed to help in coating pure 2D graphene-based suspension on ITO.

The counter electrode (cathode) was created by drop-casting (2-3 drops) the GO suspension on the conductive side of ITO. Drop-casted GO on ITO was then reduced in a

vacuum oven by annealing at 200 °C for 3 h to remove undesired oxygen (=O), hydroxyl (–OH), and carboxyl (–COOH) functional groups yielding in reduced graphene oxide (rGO) blackish deposited layers. The prepared rGO-based counter electrodes are shown in Figure 3.3(B), which were then used later in creating the four selected cell structures, Figure 3.3(A).

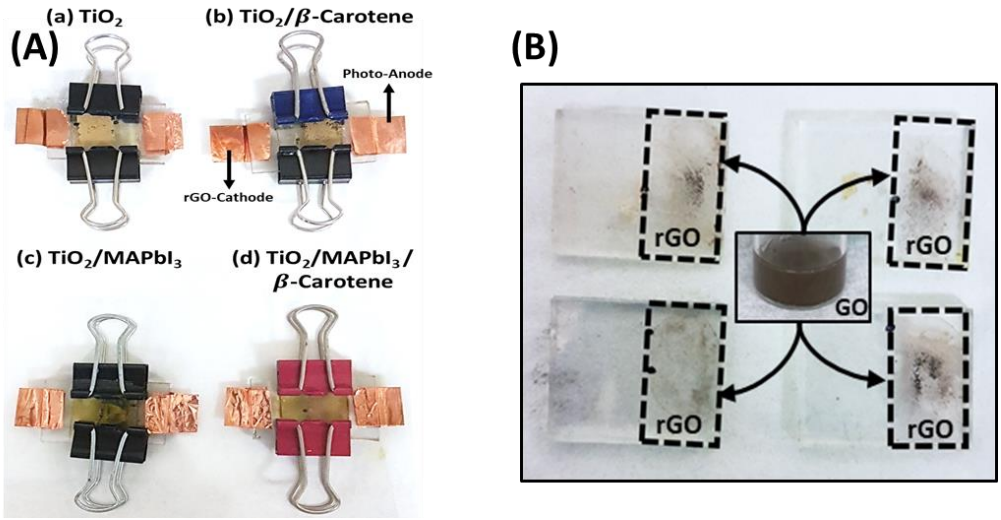

Figure 3.3 (A) Nano-architecturally structured DSSCs using different photoanode designs with natural-sensitization and/or co-sensitization; **(B)** Post-annealed ITO/rGO counter electrodes for lower series resistance (R_s) and efficient current (electron) collection.

3.6 Discussion

We have prepared the ITO/TiO_2 structure by annealing TiO_2 at 400 °C for 30 min for crystallization creating a layer of a wide bandgap semiconductor (3.2 eV) [48] atop of the ITO [212]. The pre-prepared precursor solution of $MAPbI_3$ was deposited on the sintered ITO/TiO_2, then annealed at 100 °C for 1 h to obtain the crystal structure for $MAPbI_3$. Created photoanode heterostructures soaked in β-carotene (Solution A) for >24 h to ensure dye deposition. The GO deposited on the ITO was reduced in a vacuum oven by annealing at 200 °C for 3 h to remove undesired functional groups and form rGO.

Chapter 4: Materials Characterization of DSSCs Electrode Active Layers

Maddah, H. A., Aryadwita, L., Berry, V., & Behura, S. K. (2020). Perovskite Cosensitization for Reduced Voltage Loss in Naturally-Sensitized Solar Cells, ***Nano Energy,*** Under-Review.

4.1 Introduction

Raman spectroscopy is an important optical characterization tool utilized for materials surface characterization from detection of vibrational, rotational and other low and/or high-frequency modes of a molecule through inelastic scattering which provides the molecular fingerprints of different materials [217]–[221]. Even though that Raman effect (inelastic scattering) is very small and can be only as 1 in 10^7 photons, using Raman spectroscopy allows us to detect the tiny fraction of the inelastically scattered photons which can be assessed from a laser light (532 nm) where the spectrum is plotted to identify the molecular fingerprints [221].

Scanning electron microscope (SEM) is one of the common methods for imaging the microstructure and morphology of the materials, utilized to observe and detect surface morphology and structural characteristics of nanostructured or microvolume samples. In SEM, an electron beam (fine and focused) with low energy is radiated to the material and scans the surface of the sample. Several different interactions occur as the beam reaches and enters the material, which lead to the emission of photons and electrons from or near the sample surface. In order to form an image, the receiving signals produced from the electron–sample interactions are detected with different types of detectors depending on the mode of SEM being used. Different modes of SEM exist, based on the produced various signals, for characterization of materials such as the X-ray mapping, secondary electrons imaging, backscattered electrons imaging, electron channeling, and Auger electron microscopy. When the electron beam scans the sample surface, the signals will change

according to the surface topography. The limited emission of secondary electrons within the volume close to the electron focusing area results in high image resolution. The three-dimensional appearance of images comes from the deep depth of field and shadow effect of secondary electron contrast. A typical SEM consists of several components such as: (i) the electron gun (electron emitter), (ii) hairpin tungsten gun to form high-resolution images through creating a high diameter electron beam, (iii) electromagnetic lenses and apertures to focus and shape the electron beam, and (iv) a high-vacuum environment allowing easy electrons movement and without being scattered or absorbed by the air. The resolution of a field emission scanning electron microscope (FESEM) can reach as low as 1 nm. Another important feature of the scanning electron microscope is that it can be used to observe and analyze samples three-dimensionally due to its deep depth of field. The greater the depth of field, the more sample information is provided [222], [223].

4.2 Raman Spectroscopy Characterization

Raman spectroscopy characterization of photoactive electrode materials was performed using confocal Raman microscope (Raman-AFM, WITec alpha 300 RA, laser wavelength of 532 nm). Single-spectrum data were carried out using a laser spot-size 721 nm and 20× objective lens. Spatial mapping obtained for a 25 × 25 μm^2 region of β-carotene on ITO/TiO_2 to check layer uniformity *via* investigating position and intensity of v_3 peak.

4.2.1 Photoanode Active Layers

Raman spectroscopy characterization (532 nm laser excitation) of bulk TiO_2 in the anatase phase reveal evident vibrational modes at 638, 520, 396, and a very distinct peak at 129 cm^{-1} (Figure 4.1, Figure 4.2, and Figure 4.3) confirming the deposition of TiO_2 layer

on ITO substrate. The space group D_{4h}^{19} is attributed to anatase phase with assumed site symmetries for the Ti and O atoms within the unit cell (D_{2d} for Ti; C_{2v} for O), group-theory analysis shows six Raman-active "lattice vibrations" assigned as follows: A_{1g} (517 cm^{-1}), B_{1g} (640 cm^{-1}), B_{1g} (397 cm^{-1}), E_g (640 cm^{-1}), E_g (147 cm^{-1}), and E_g (197 cm^{-1}). The distinct peaks at 128~134 cm^{-1} indicate the vibrations of Ti-Ti bonding in the octahedral chains. The band 396 cm^{-1} represents the O-O covalent interactions in TiO_2, where covalence/length/frequency relation calculations confirm Ti-O band occurrence at 638 and 520 cm^{-1} [224]. Broader/shifted peaks were observed in Figure 4.3 for Ti-O (638 cm^{-1}) and O-O (396 cm^{-1}) vibrations from addition of $MAPbI_3$ and/or β-carotene photosensitizers. The O-O band is blue-shifted while the Ti-O band is red-shifted indicating changes in the energy requirements for Raman-active polarizable vibrations.

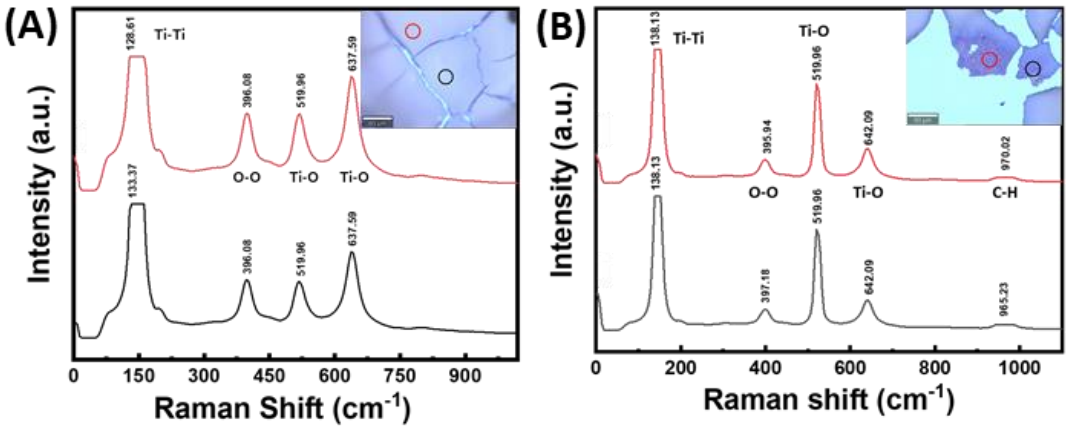

Figure 4.1 Raman spectroscopy characterization of different nanostructured naturally-sensitized photoanodes: **(A)** ITO/TiO_2; **(B)** ITO/TiO_2/β-carotene, insets: optical image and scan location.

Raman spectra of $MAPbI_3$ is characterized by two complex broad bands: the first one with lower wavenumber (50-150 cm^{-1}) and the second one with higher wavenumber contribution (175-450 cm^{-1}) where both bands are Raman-active (polarizable structural bonds) with a 532 nm (green) laser light [217], [218], [225]–[227]. Further, $MAPbI_3$

spectra can be portioned into three distinct regions: (i) internal vibrations of methylammonium (MA) cations including stretching, bending, rocking modes (300-3200 cm^{-1}) with a broad and unstructured modes (200−400 cm^{-1}) assigned to the torsional mode of MA cations; (ii) liberations/translation and spinning modes of organic MA cations (60-180 cm^{-1}); (iii) stretching/bending internal vibrations of the PbI_3 network (<120 cm^{-1}) and Pb-I-Pb bending modes (<60cm^{-1}) [227].

In Figure 4.2, and Figure 4.3, we observed the Raman spectra of $MAPbI_3$ with two prominent peaks: (i) the vibrational mode at 76∼80 cm^{-1} (theoretically ∼110 cm^{-1}) is attributed to the Pb-I stretching and bending of the Pb-I-Pb bond with either A_g or B_{2g} symmetry, and (ii) the bands at 200 and 300 cm^{-1} (theoretically ∼250 cm^{-1}) indicate the liberations of the MA cations (MA torsional modes) [217], [226]. No red-shifts were observed in perovskite peaks when $MAPbI_3$ was interfaced with other photoanode materials confirming stress-free/undeformed perovskite crystals and preserved $MAPbI_3$ photosensitivity. Thampy et al. [228] proved that the use of [$MAPbI_3$ + TiO_2] ∼ $MAPbI_3$ provides the highest interfacial stability, indicated by decomposition temperature, as compared to [$MAPbI_3$ + SnO_2] > [$MAPbI_3$ + NiO] contacts. MAI DFT calculations and experiments showed the strongly bound $MAPbI_3$ molecules on the TiO_2 surface preventing further reactions [228]. This comes in agreement with the observed stress-free/undeformed $MAPbI_3$ crystals deposited on TiO_2 suggesting equivalent $MAPbI_3$ bulk decomposition rates for [$MAPbI_3$ + TiO_2] ∼ $MAPbI_3$ for reduced interfacial recombination and improved device stability.

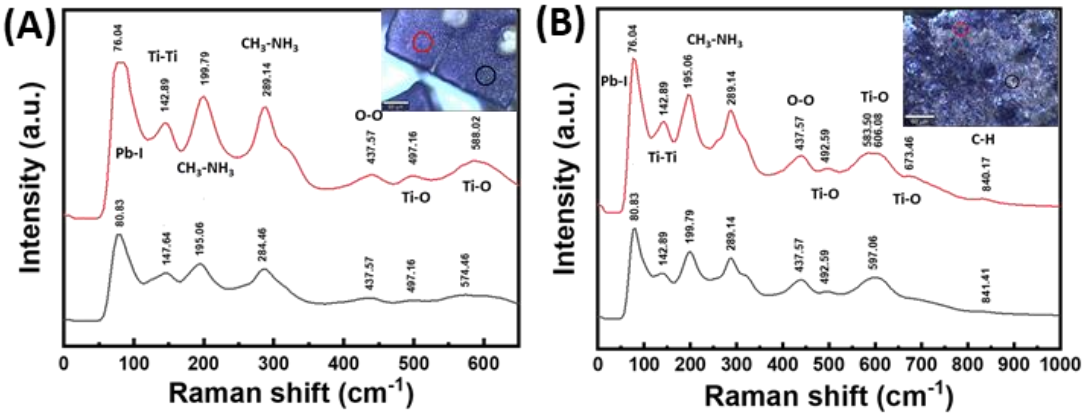

Figure 4.2 Raman spectroscopy characterization of different nanostructured naturally-sensitized photoanodes: **(A)** ITO/TiO_2/$MAPbI_3$; **(B)** ITO/TiO_2/$MAPbI_3$/β-carotene, insets: optical image and scan location.

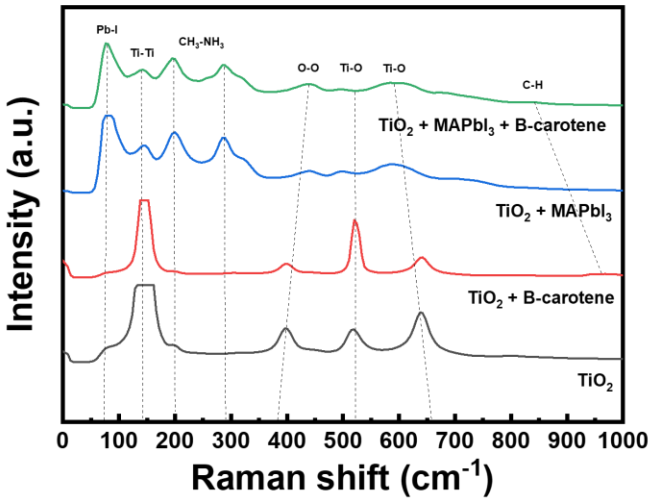

Figure 4.3 Comparison of Raman bands observed in the four designed photoanode heterostructure surfaces showing energy-shifts (red- or blue-shifted) in TiO_2 and β-carotene when combined with $MAPbI_3$ cosensitizer.

It turned out that the interactions between perovskite and TiO_2 at 0 K are purely van der Waals, whereas I–Ti covalent bonds can form transiently at the interface at ambient temperatures according to time-domain DFT calculations. The strong interactions between the donor and acceptor species at $CH_3NH_3PbI_3$/TiO_2 interface ensure fast electron injection completed within 100 fs. The covalent bonding contributes to the high efficiencies of perovskite-sensitized TiO_2 solar cells due to facilitated photoexcitation of charge-separated states and adiabatic electron transfer leading to ultrafast interfacial charge separation [229].

The Raman spectra of β-carotene with 11 conjugated double bonds (n = 11) shows a weak band at 970 cm^{-1} (v_3) due to the in-plane rocking modes of the CH_3 groups attached to the polyene chain and C-H bending (Figure 4.4) [230], [231]. Interestingly, when β-carotene was combined with either TiO_2 and $MAPbI_3$, we observed that there is a strong red-shift in the weak band of β-carotene equivalent to -130 cm^{-1}. This red-shifting might indicate stresses in the β-carotene structure induced by hydrogen-bonding and/or dipole-dipole van der Waals interactions of C-H bond with $MAPbI_3$ crystal lattice.

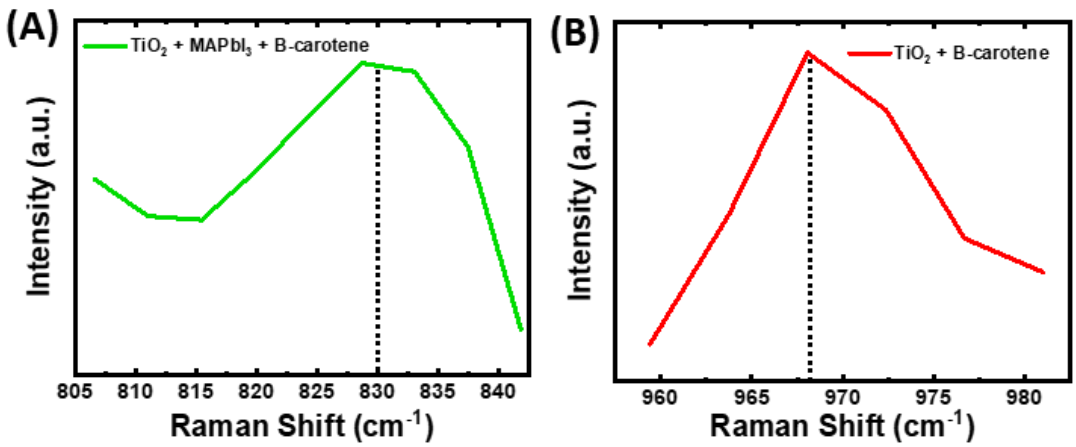

Figure 4.4. Zoom-in on the (v_3) vibrational bands of β-carotene from C-H rocking: **(A)** ITO/TiO_2/$MAPbI_3$/β-carotene; **(B)** ITO/TiO_2/β-carotene heterostructures.

4.2.2 Uniformity of β-Carotene Layer

Area scans for the position (left) and intensity (right) of the β-carotene band at 970 cm^{-1} in the two photoanodes (b) TiO_2/β-carotene and (d) $TiO_2/MAPbI_3/\beta$-carotene heterostructures (from Figure 3.3) are illustrated in Figure 4.5(A) and Figure 4.5(B), respectively, showing a uniform distribution of β-carotene on the TiO_2 semiconductor surface. The slight discontinuities in the deposited β-carotene layers could be the reason behind the low current densities (lower rates of injected electrons) when β-carotene is added in the photoanode.

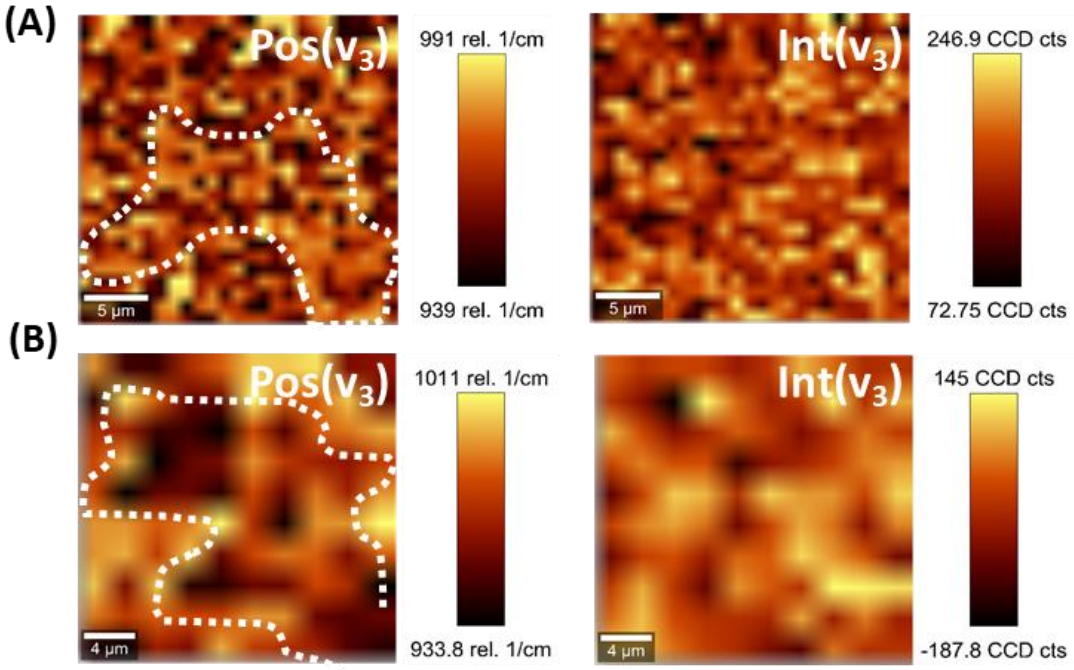

Figure 4.5 (A) and **(B)** Area scans (using Raman spectroscopy) for β-carotene uniformity/layer-thickness on TiO_2 and $TiO_2/MAPbI_3$, respectively, from peak position (left) and intensity (right).

4.2.3 rGO Cathode

In order to build a cost-effective bio-DSSCs, we have further employed a natural carbon source to create rGO-based counter electrodes (CEs). GO and rGO CEs were characterized from D-peak at 1346 cm^{-1} from in-plane (E_{2g}) structural defects and disordered sp^2 domains, G-peak at 1589 cm^{-1} (A_{1g}) from graphitized sp^2-hybridized C=C bonds, and 2D peaks at 2708 cm^{-1} from sp^2 hybridization [232], [233] with $I_{2D}/I_G \approx 0.74$ confirming the existence of a multi-layered graphene structure (Figure 4.6).

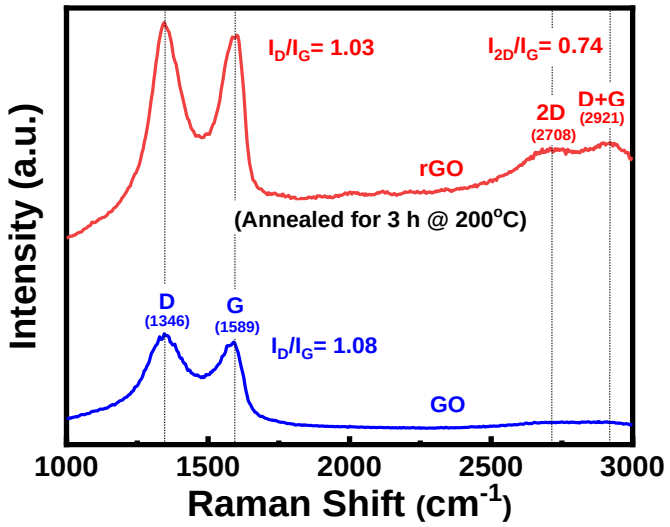

Figure 4.6 Single-spectrum Raman spectroscopy characterization for the synthesized GO and the annealed ITO/GO yielding in rGO-cathode electrodes.

4.3 Morphology and Cross-Section Characterization of Photoanode

The optimal designed cell structures with perovskite cosensitization is illustrated in Figure 3.3(A-[d]). FESEM and SEM images (Figure 4.7) show the uniformly deposited/annealed TiO_2 morphology on ITO and photoanode cross section layers characterization for quantifying each layer thickness: ITO~260 nm, TiO_2~1.2 µm, and $MAPbI_3$~2 µm. Since the annealing temperature of TiO_2 films was at 400 °C, anatase crystals are expected to form (300-700 °C) [234] (TiO_2 nanoparticles are observed as small and scattered crystals with typical ~40 nm grains), rather than rutile and brookite.

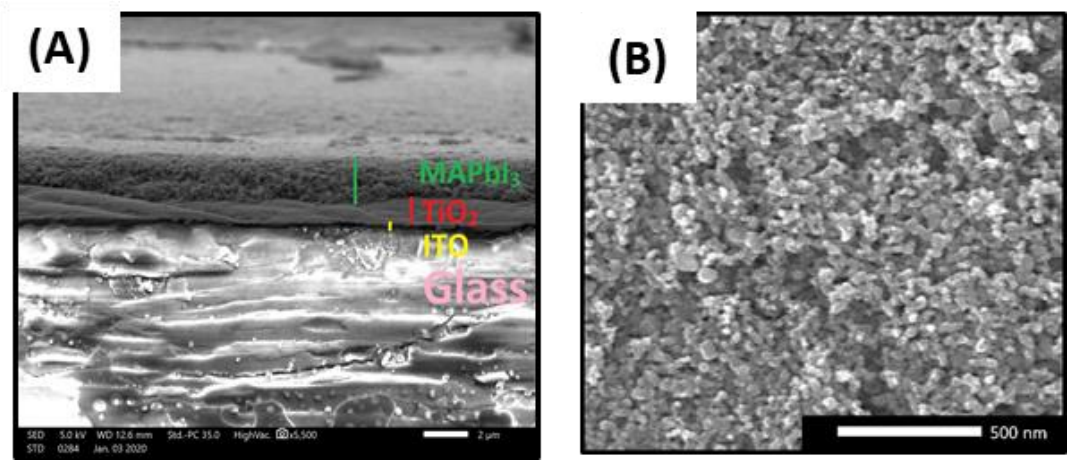

Figure 4.7. **(A)** FESEM and SEM showing sensitized/cosensitized spin-coated photoanode cross section and deposited layers with their approximated thicknesses**; (B)** Surface morphology of ITO/TiO_2 showing TiO_2 nanoparticles with average-diameter of 30-40 nm.

Chapter 5: Device Fabrication for Diode and Photovoltaic Measurements

Maddah, H. A., Aryadwita, L., Berry, V., & Behura, S. K. (2020). Perovskite Cosensitization for Reduced Voltage Loss in Naturally-Sensitized Solar Cells, ***Nano Energy,*** Under-Review.

5.1 Selected Photoanode Designs for Cell Fabrication

Four DSSC cell designs are considered for the performance analysis:

(a) ITO/TiO_2/[I^-/I_3^-]/rGO/ITO;

(b) ITO/TiO_2/β-carotene/[I^-/I_3^-]/rGO/ITO;

(c) ITO/TiO_2/$MAPbI_3$/[I^-/I_3^-]/rGO/ITO; and

(d) ITO/TiO_2/$MAPbI_3$/β-carotene/[I^-/I_3^-]/rGO/ITO;

as illustrated in Figure 5.1(A-D).

A drop of [I^-/I_3^-] liquid redox electrolyte was drop-casted on the TiO_2-photoanode. Both photoanode and cathode were brought together while keeping the conductive ITO sides facing each other with a careful line-up of TiO_2-anode on rGO-cathode. Once the line-up was satisfied, binder-clips were applied on the cell sides to hold the DSSCs in-place. An offset was kept between the two electrodes to connect Cu-tapes electrical contacts at the positive and negative terminals creating a complete electric circuit ready for current-voltage (IV) analysis [212]. Diode and photovoltaic measurements were carried out in room-conditions with a source meter (Keithley 2612); current density versus voltage (IV) measurements of designed solar cells were performed under 100 mW/cm^2 illuminations (AM1.5G).

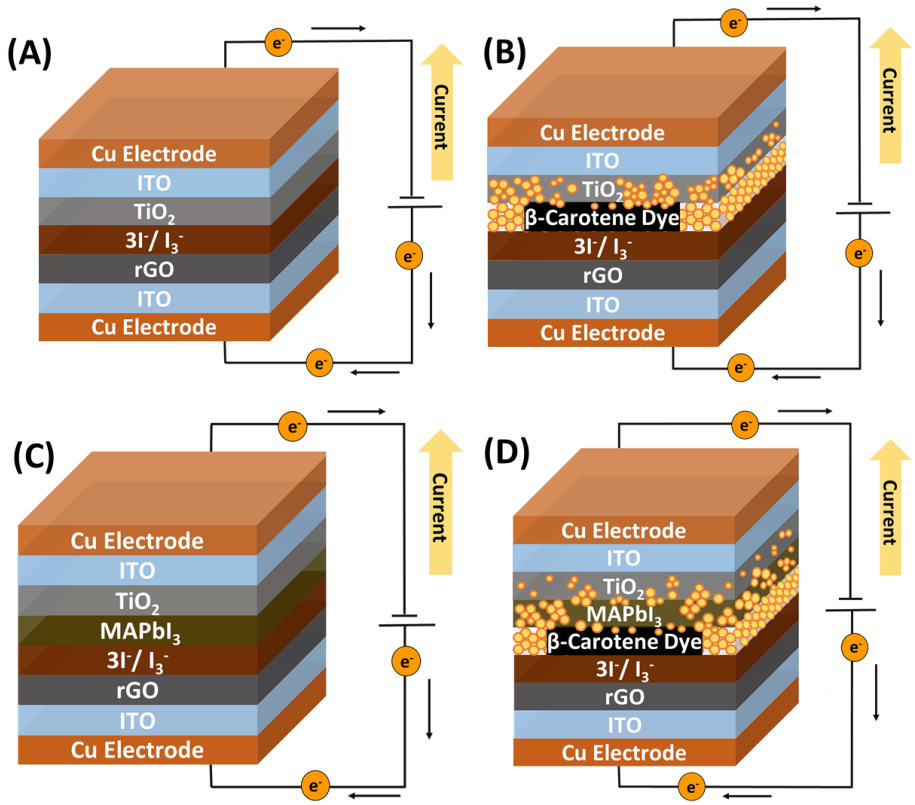

Figure 5.1 Selected designs and fabricated bio-DSSCs: **(A)** ITO/TiO_2/[I^-/I_3^-]/rGO/ITO; **(B)** ITO/TiO_2/β-carotene/[I^-/I_3^-]/rGO/ITO; **(C)** ITO/TiO_2/$MAPbI_3$/[I^-/I_3^-]/rGO/ITO; and **(D)** ITO/TiO_2/$MAPbI_3$/β-carotene/[I^-/I_3^-]/rGO/ITO.

5.2 Diode Characteristics of Bio/Co-Sensitized DSSCs

5.2.1. Equivalent Circuit Single-Diode Model

An equivalent circuit model resembling the single-diode model for DSSCs was proposed by Sarker et al. [235] to relate possible interfacial resistances in DSSCs to the produced cell current and voltage. Total cell current (I_{cell}) may be obtained from applying Kirchhoffs's voltage (KVL) and current (KCL) laws to the circuit model, Figure 5.2(A), in order to get Eq. (1) where I_{ph}, I_0, I_r, and I_{sh} refer to cell photo-generated current, dark saturation current, back reaction (recombination) current, and shunt (leakage) current, respectively. Photoanode electrode voltage (V_{PE}) and I_{sh} are defined in previous works as shown in Eq. (2). Series resistance (R_s), shunt resistance (R_{sh}), recombination resistance

(R_r), and applied cell voltage (V_{cell}) in DSSCs play an important role in controlling both V_{PE}, I_{sh}, and therefore I_{cell}. Further, recombination current (I_r) can be determined from Eq. (3) which was obtained from a Boltzmann-like distribution of electrons and V_{PE} that is the difference between electrons Fermi level and electrolyte redox potential. Hence, plugging both Eq. (2) and Eq. (3) in Eq. (1) will yield in Eq. (4) [235] that is the equivalent circuit model for DSSCs; where q (1.602×10^{-18} C) is the electron charge, n is the ideality factor, k_B is Boltzmann constant (1.38×10^{-23} J K^{-1}) and T is the absolute temperature.

$$I_{cell} = I_{ph} + I_0 - I_r - I_{sh} \tag{1}$$

$$V_{PE} = V_{cell} + I_{cell}R_s \quad ; \quad I_{sh} = \frac{V_{PE}}{R_{sh}} \tag{2}$$

$$I_r = I_0 \exp\left(\frac{qV_{PE}}{nk_BT}\right) \tag{3}$$

$$I_{cell} = I_{ph} - I_0\left[\exp\left(\frac{q(V_{cell} + I_{cell}R_s)}{nk_BT}\right) - 1\right] - \frac{V_{cell} + I_{cell}R_s}{R_{sh}} \tag{4}$$

The determined circuit model is comparable to the diode model equation for solar cells as explained in previous literature [236]–[238]. Both R_s and R_{sh} in DSSCs arise from the interfacial contact resistances between the phase contacts in the compact semiconductor layer [239] influencing electron recombination; Figure 5.2(B), specifically at the three interfaces: (i) TiO_2/electrolyte, (ii) TiO_2/dye, and (iii) ITO/electrolyte [82], [84], [240], [241]. Contact and bulk resistances from R_s and defect resistance from R_{sh} are both responsible for increasing recombination rates, shortening electron lifetime, and therefore decreasing the overall cell efficiency.

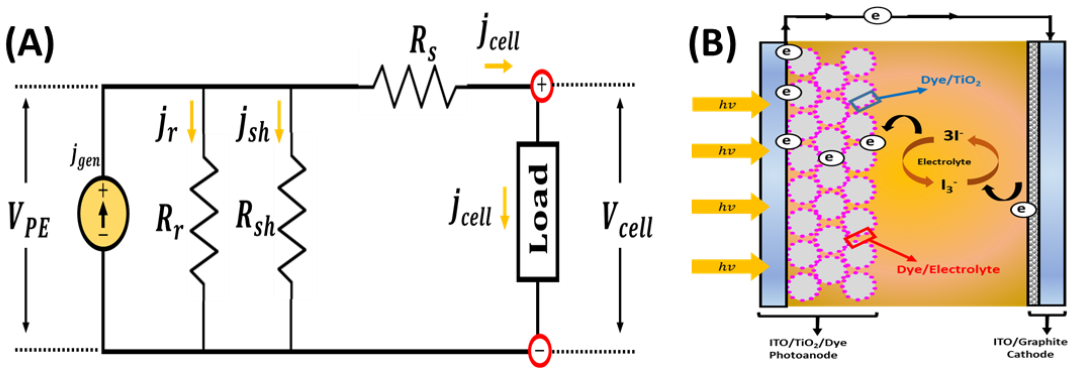

Figure 5.2 (A) Equivalent circuit and/or single-diode model for DSSCs, (J=I/Area); **(B)** TiO_2 photoanode compact layer in DSSCs.

Eq. (4) can be simplified further to estimate the DSSCs open-circuit voltage (V_{oc}) from the following assumptions [235] (i) there is an infinite value of R_{sh}, (ii) $I_{cell} = 0$, (iii) $V_{cell} = V_{oc}$, and $(I_{ph} >> I_0) \rightarrow (I_{ph} + I_0 \approx I_{ph})$; which will result in Eq. (5).

$$V_{oc} = \frac{nk_BT}{q} \ln\left(\frac{I_{ph}}{I_0}\right) \tag{5}$$

Similarly, Eq. (4) can be simplified further to estimate the DSSCs short-circuit current (I_{sc}) from the following assumptions [235] (i) there is an infinite value of R_{sh}, (ii) $I_{cell} = \mathrm{I_{sc}}$, (iii) $V_{cell} = 0$, and $(I_{ph} >> I_0) \rightarrow (I_{ph} + I_0 \approx I_{ph})$; which will result in Eq. (6).

$$\boldsymbol{I_{sc} = I_{ph} - I_0 \exp\left(\frac{qI_{sc}R_s}{nk_BT}\right)} \tag{6}$$

For ideal systems: ($R_s \rightarrow 0$); hence, Eq. (6) becomes Eq. (7).

$$\boldsymbol{I_{sc} = I_{ph} - I_0} \tag{7}$$

5.2.2. Results and Discussion

In order to quantify the diode and photovoltaic parameters, thermionic emission (TE) [242] and Cheung's methods [243] are typically used. The cell diode parameters were determined from the exponential fitting of dark current density-voltage (J-V) data (dark current) following the TE model: $J_D = J_0 \exp\left(\frac{qV}{nk_BT}\right)$, (Figure 5.3), where symbols definitions are as follows: q (1.602×10^{-18} C) is the electron charge, n is the ideality factor, k_B is Boltzmann constant (1.38×10^{-23} J K^{-1}), T is the absolute temperature (298 K), J_D is diode-generated current, and J_0 is dark saturation current.

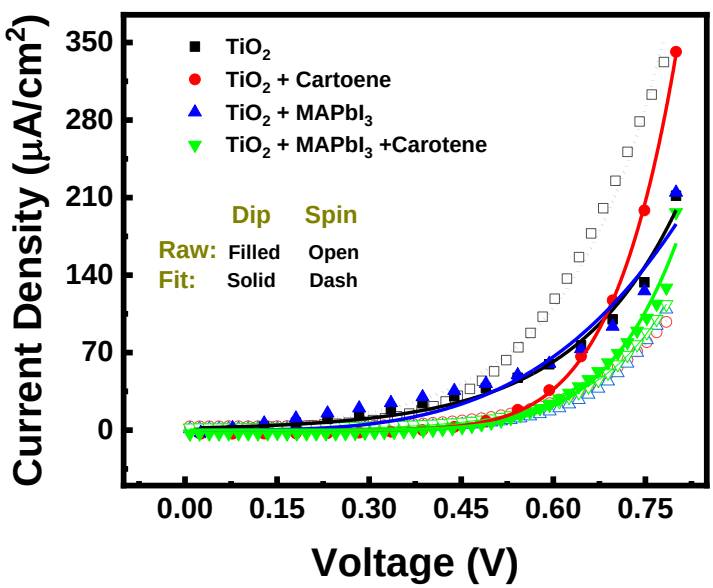

Figure 5.3 Exponential fitting of forward-current using the TE diode model for analyzing diode ideality (n factors) for β-carotene-sensitized and/or $MAPbI_3$ cosensitized DSSCs.

The diode ideality factor (n) approached unity by $MAPbI_3$ and/or β-carotene photoanode sensitization reaching optimal n=4–5, due to reduced current leakage (J_0). Dark saturation currents (J_0) are found to approach the nA range when adding $MAPbI_3$ and/or β-carotene yielding in less leakage current, Table 5.1 or Figure 5.8 for spin-coated

photoanode cells. Lower n value indicates better electron transport from reduced recombination at the interfacial contacts. Reproducibility of the diode curves was obtained for the same photoanode (see Appendix A, Figure A1). Sensitized/cosensitized DSSCs diodes showed the highest RF≈1.2–1.5 indicating a two-fold increase in [forward/reverse] currents compared to only-TiO_2 photoanodes (Figure 5.4). ITO/TiO_2 Schottky barrier height (SBH=ϕ_{SBH}) was also diminished matching the expected high V_{oc} (Figure 5.7).

Table 5.1. Determined diode parameters and ϕ_{SBH} (at the ITO/TiO_2 interface) in different DSSCs using various naturally-sensitized and/or cosensitized photoanode architectures.*

(SN) Photoanode Architecture	Coating	J_0 (μA)	n	RF	ϕ_{SBH} (V)	J_1 (pA)	J_2 (μA)
(a) TiO_2	Dip	2.280	5.97	0.73	0.607	0.274	0.150
	Spin	1.870	6.62	0.71	0.607	0.143	0.150
(b) TiO_2 + β-Carotene	Dip	0.364	5.40	0.74	0.559	N/A	N/A
	Spin	**0.002**	**5.00**	1.23	0.557	N/A	N/A
(c) TiO_2 + $MAPbI_3$	**Dip**	**0.006**	**4.03**	1.14	**0.542**	**423.2**	**1.330**
	Spin	0.041	10.76	1.42	0.542	3.988	1.170
(d) TiO_2 + $MAPbI_3$ + β-Carotene	**Dip**	0.173	4.67	**1.26**	0.544	N/A	N/A
	Spin	0.081	5.47	**1.51**	**0.528**	N/A	N/A

*R^2 > 0.99 in the different cells using TE diode equation against curves exponential fitting $[y = a\exp(bx)]$; ϕ_{SBH} at ITO/TiO_2 from Eq. (19) from the measured J_{sc} and V_{oc}=V_1 reported in Table 5.3; J_1 is the apparent current density in both TiO_2 and $MAPbI_3$, J_2 is the total apparent current density in the electrolyte solution $[I^-/I_3^-]$ from electron diffusion, calculated @ corresponding reported diffusion coefficients (D_e) and charge/electron densities or number of electrons (n_e) of materials from literature (see section 6.2.2).

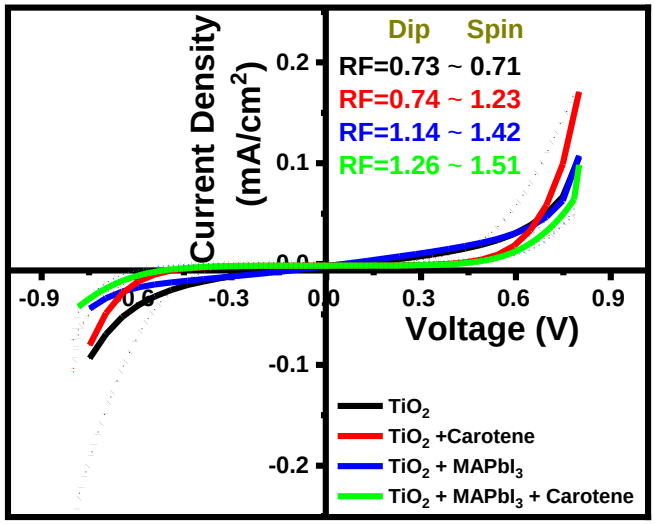

Figure 5.4 Diode behavior and rectification factors (RFs) for β-carotene-sensitized and/or $MAPbI_3$ cosensitized DSSCs with highest RF≈1.5 reserved for spin-coated photoanode with sensitized/cosensitized DSSC reducing dark saturation currents (J_0).

5.3 Photovoltaic Performance of Bio/Co-Sensitized DSSCs

5.3.1. Photoelectrochemical Performance Parameters

The photoelectrochemical performance of various designs of DSSCs using different electrodes, semiconductors, and dye photosensitizers is measured from four typical parameters, including: (i) the short-circuit current, (ii) the open-circuit voltage, (iii) fill factor, and (iv) conversion efficiency.

The short-circuit current (I_{sc}) is the maximum current from a DSSC which occurs at zero voltage (i.e. short-circuited solar cell), and can be determined from the IV curve and/or calculated from Eq. (8) [84], [244]; where q (1.602×10^{-18} C) is the electron charge, G is the generation rate, L_n and L_p are the electron and hole diffusion lengths respectively, IPCE is the incident photon-to-current-efficiency and Φ_0 is the incident photoflux both over the spectral distribution as a function of light wavelength (λ) in nm, and $r(\lambda)$ is the incident light loss [84], [244].

The short-circuit current arises from the generation and collection of light-generated carriers and it depends on various critical parameters including (i) the area of the DSSC (it is more common to report current density in mA/cm^2 to eliminate the dependence on area), (ii) the number of directed and/or delivered photons (i.e. light intensity), (iii) the spectrum of the incident light which is usually standardized to AM1.5, (iv) the DSSC optical properties like carriers collection and light absorption, and (v) surface collection probability which is associated with surface passivation, electron and hole (carriers) diffusion length and their lifetime. The short-circuit current usually decreases with increasing bandgap energy (E_g) and increases with increasing generation of light-generation carriers [244].

$$I_{sc} = qG\left(L_n + L_p\right) = q\int IPCE(\lambda)\Phi_0(\lambda)\left(1 - r(\lambda)\right)d\lambda \tag{8}$$

The open-circuit voltage (V_{oc}) is the maximum voltage from a DSSC which occurs at zero current, and can be determined from the IV curve and/or calculated from Eq. (9) [84], [244]; where q (1.602×10^{-18} C) is the electron charge, n is the ideality factor, ($k_B = k$) is Boltzmann constant (1.38×10^{-23} J K^{-1}), T is the absolute temperature, I_{ph} and I_0 are photo-generated and dark-generated saturation currents respectively, η is the quantum yield of photo-generated electrons for the given incident photoflux (Φ_0), n_0 represents the electron density on the conduction band of TiO_2 in the dark, while k_{et} reflects the recombination reaction rate for the given triiodide concentration $[I_3^-]$ [84], [244].

The open-circuit voltage arises from the forward bias in the solar cell junction due to light intensity, and it decreases with an increase in the amount of recombination of the generated carriers (electron-hole pairs) in the DSSC and increases with an increase in the band gap energy (E_g) [244]. Theoretically, the open-circuit voltage corresponds to the energy difference between the Fermi level (from the illumination of the solid semiconductor in the DSSC) and the Nernst potential (of the redox couple in the electrolyte). However, the energy difference between the conduction band edge and the redox couple, in reality, is smaller than the expected difference from the theory which lead to lowering the observed open-circuit voltage; and this is due to the inevitable competition that arises between electron transfer and charge recombination pathways [81].

$$V_{oc} = \frac{nkT}{q}\ln\left(\frac{I_{ph}}{I_0} + 1\right) = \frac{kT}{q}\ln\left(\frac{\eta\Phi_0}{n_0 k_{et}[I_3^-]}\right) \tag{9}$$

The fill factor (FF) parameter, in conjunction with V_{oc} and I_{sc}, gives us an estimation of the maximum possible power from a DSSC and/or squareness of the IV curve which can be calculated from Eq. (10) [50], [82], [244], where the subscript mp refers to the maximum point. The FF is defined as the ratio of the maximum power (P_{max}) from the DSSC to the product of V_{oc} and I_{sc} and it can take values between 0 and 1 [81]. The maximum power from the DSSC is reached when the product of the current and the voltage is maximal [52]. The measure of the squareness of the IV curve of the DSSC is directly associated with the FF parameter, and it is preferred to have the largest possible rectangle area in the IV curve for achieving higher FF and thereby higher cell efficiency (Figure 5.5) [244]. The FF reflects both electrical and electrochemical losses occurring during the DSSC operation [81], and it is proportionally related to the applied voltage and inversely proportional to carriers recombination rate [244]. The FF is also capable of measuring the junction quality and series resistance of the DSSC [50].

$$FF = \frac{I_{mp} \times V_{mp}}{I_{sc} \times V_{oc}} = \frac{P_{max}}{I_{sc} \times V_{oc}} \tag{10}$$

The solar-to-electrical conversion efficiency (η) of the DSSC is the most common parameter to identify and compare between performances of various cell designs. Solar-to-energy conversion efficiency is defined as the ratio of the output energy from the DSSC to the input power (P_{in}) from sunlight energy (usually with a simulated solar irradiation of AM1.5) and can be calculated from Eq. (11) [50], [82], [244]. The conversion efficiency of a DSSC depends on the spectrum and intensity of the incident sunlight as well as the temperature of the DSSC; hence, these parameters must be carefully controlled and optimized to obtain credible results for comparison purposes [244]. Incident photon-to-

current conversion efficiency (IPCE) and/or external quantum efficiency (EQE), Eq. (12) [81], are some of the other equivalent names of the above-discussed conversion efficiency which, as stated previously, determines how efficient is the DSSC in converting incident light into electrical energy at a given wavelength. The IPCE can be determined using Eq. (12), where $LHE(\lambda)$ is the light-harvesting efficiency at wavelength λ, φ_{inj} is the quantum yield for electron injection from the excited sensitizer in the conduction band of the TiO_2, and η_{coll} is the efficiency for the collection of electrons [81].

$$\eta = \frac{I_{sc} \times V_{oc} \times FF}{P_{in}} \times 100\% = \frac{P_{max}}{P_{in}} \times 100\% \tag{11}$$

$$IPCE(\lambda) = \frac{Photocurrent\ density}{Waverlenght\ \times Photon\ flux} = LHE(\lambda) \times \varphi_{inj} \times \eta_{coll} \tag{12}$$

IPCE has to be increased to enhance light absorption over a longer wavelength range. It is worth to mention that there is a difference between EQE and internal quantum efficiency (IQE); basically, EQE is the ratio of the number of collected carriers to the number incident photons while IQE is the ratio of the number of collected carriers to the number of absorbed photons [49], [50], [81], [82]. Table 5.2 summarizes the four common photoelectrochemical parameters used to evaluate DSSCs performance.

Table 5.2 Typical photoelectrochemical parameters for the determination of DSSCs performance

Parameter	Definition	Equation
Short-circuit current (I_{sc})	Max current at zero voltage	(8)
Open-circuit voltage (V_{oc})	Max voltage at zero current	(9)
Fill factor (FF)	Squareness of the IV curve	(10)
Conversion efficiency (η)[a]	Output power over input	(11) and (12)

[a] $\eta = IPCE = EQE$

5.3.2. IV Curves and Diode Resistive Effects

IV curves (Figure 5.5) and equivalent circuits for the DSSCs are very useful tools for the analysis of DSSC devices in order to improve cell performance and understand the solar cell mechanism. A diode-like behavior is applicable to DSSCs due to the presence of a charge transport at the interface of semiconductor/dye/electrolyte [45]; hence, the DSSCs mechanism can be simply expressed from the equivalent circuit of the single diode model as shown in Figure 5.2(A) and Eq. (4). The major benefit from using the equivalent circuit model is to avoid the tedious use of various chemical and physical parameters, and instead to use a combination of a minimal number of electrical circuit elements for describing the DSSC system. However, the single diode model cannot explain the effect of the capacitance (which reflects the existence of a double-charged layer known as Helmholtz layer at the semiconductor/electrolyte interface) and/or unsteady state conditions on the cell performance [82].

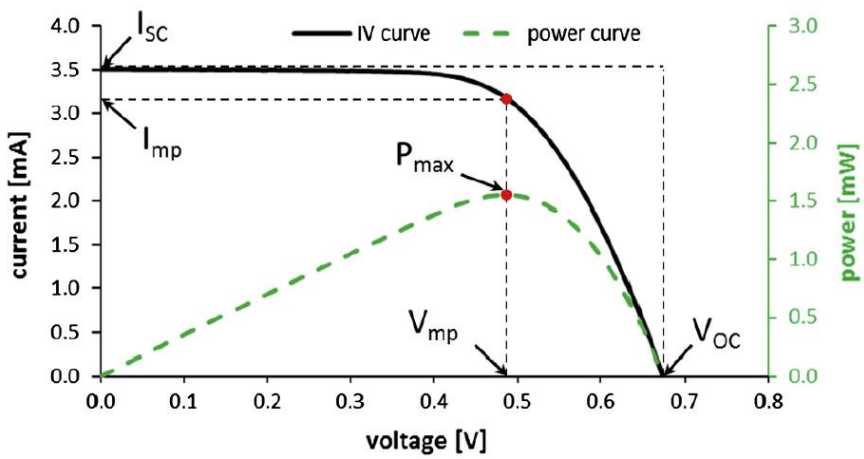

Figure 5.5 Photocurrent-voltage characteristics (I-V curve) of a DSSC; photosensitizer: ruthenium (Ru) complex dye N719, liquid electrolyte: redox couple [I^-/I_3^-]; Adapted and modified from [52].

Resistive effects in the DSSCs may reduce cell efficiency by dissipating power in the resistance; a parasitic resistance which includes R_s and R_{sh} can reduce FF due to either high R_s and/or low R_{sh} values. Light-generated current can flow through an alternative current path when there is a low shunt resistance which causes a high solar power loss. Diversion in the current flow reduces the amount of current flowing through the solar cell junction which results in lower voltage (due to the lower forward bias) from the DSSCs. Series resistance arises from emitter/base current movement as well as interface and top/rear contacts; shunt resistance typically arises from manufacturing and/or fabrication defects. Series resistance is preferred to be as low as possible while shunt resistance is preferred to be as high as possible in order to achieve the maximum power output from the DSSCs [82], [244].

5.3.3. Results and Discussions

The J-V curves of the architecturally designed DSSCs with different photoanodes are plotted in Figure 5.6, with the obtained photovoltaic parameters and cell performance reported in Table 5.3. The involvement of both $MAPbI_3$ + β-carotene as a cosensitizer and a sensitizer, respectively, resulted in increasing both J_{sc} and V_{oc} leading to a higher fill factor (FF) and PCE (η).

Table 5.3. DSSCs photovoltaic parameters in DSSCs using different photoanode heterostructures.

(SN) Photoanode Architecture	Coating	R_s (kΩ)	R_{sh} (kΩ)	V_{oc} (V)	J_{sc} (μA/cm^2)	FF	η (%)
(a) TiO_2	Dip	< 33.3	55.56	0.015	0.15	0.24	5.47 x 10^{-7}
	Spin	< 4.76	5.56	0.015	0.15	0.32	7.11 x 10^{-7}
(b) TiO_2 + β-Carotene	Dip	83 – 129	37.04	0.171	0.80	0.30	4.16 x 10^{-5}
	Spin	83 – 129	47.62	0.300	0.72	0.38	8.22 x 10^{-5}
(c) TiO_2 + $MAPbI_3$	Dip	**55 – 84**	33.33	0.290	**1.33**	0.33	1.29 x 10^{-4}
	Spin	111 – 168	33.33	0.368	**1.17**	0.48	2.05 x 10^{-4}
(d) TiO_2 + $MAPbI_3$ + β-Carotene	Dip	**51 – 83**	41.67	**0.341**	1.14	**0.36**	**1.40 x 10^{-4}**
	Spin	102 – 167	**166.67**	**0.655**	1.10	**0.63**	**4.56 x 10^{-4}**

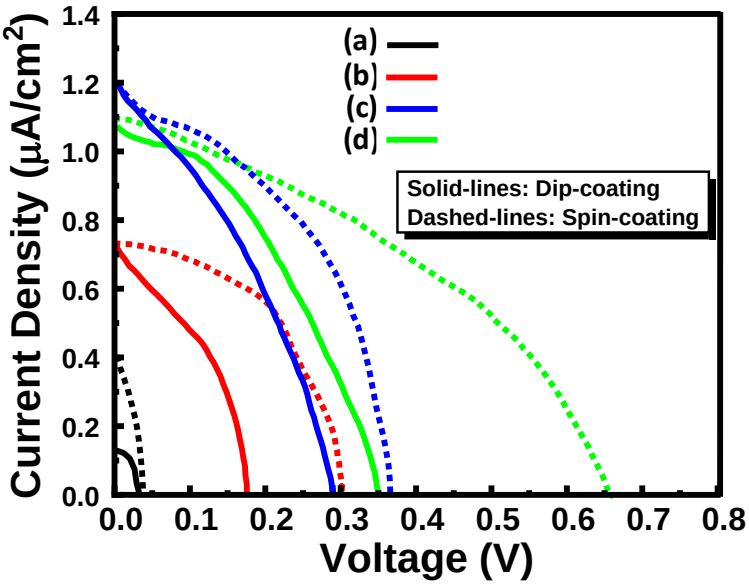

Figure 5.6 J-V curves and photovoltaic effect for β-carotene-sensitized and/or $MAPbI_3$ cosensitized DSSCs with highest $V_{oc}\approx 0.66$ V reserved for DSSC with spin-coated sensitized/cosensitized photoanode.

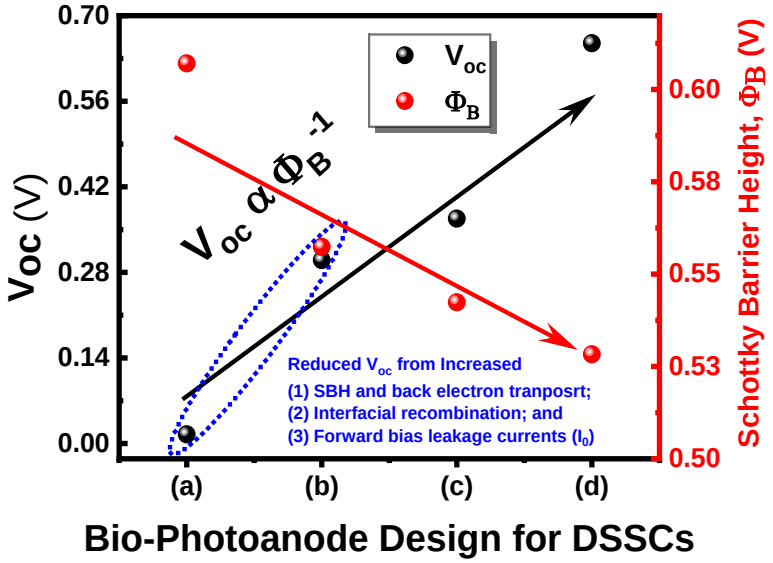

Figure 5.7 Relationship between V_{oc} and ITO/TiO_2 ϕ_{SBH} in spin-coated samples showing reduced ϕ_{SBH} from addition of $MAPbI_3$ cosensitizers resulting in high built-in potential and upward shifting of TiO_2 Fermi level for β-carotene-sensitized and/or $MAPbI_3$ cosensitized DSSCs, or as shown for the various DSSCs with different spin-coated photoanodes (a)-(d) from Figure 5.6 (or from Figure 5.1).

The reason behind the enhanced voltage is attributed to the presumed upward shifting in TiO_2 Fermi level due to increased number of injected electrons *via* $MAPbI_3$ cosensitization (lower TiO_2 work function decreases ϕ_{SBH} at ITO/TiO_2 blocking back-electron transport for minimized voltage loss, Figure 5.7). However, the high currents in perovskites-sensitized cells are attributed to (i) low J_0 and less leakage, (ii) enhanced exciton generation (e-h pairs) by the dye/perovskite molecules, and (iii) facilitated electron injection and charge separation at [$MAPbI_3$+dye]/TiO_2. Cosensitization with $MAPbI_3$ resulted in higher J_{sc} owing to low R_s allowing easy e^- injection from enhanced exciton generations and photon absorption. Reproducibility of the JV-curves has been also considered (see Appendix A, Figure A2 and A3). FF values have increased from 0.24 to 0.36 and from 0.32 to 0.63 when TiO_2 nanoparticles were interfaced with [$MAPbI_3$ + β-carotene] using dip-coated and spin-coated (Figure 5.8) photoanodes, respectively, in the different designed cell architectures, Figure 5.1(A-D), giving us a maximum PCE of (1.40–4.56)$\times 10^{-4}$% (three-order-of-magnitudes higher than that of non-sensitized DSSCs).

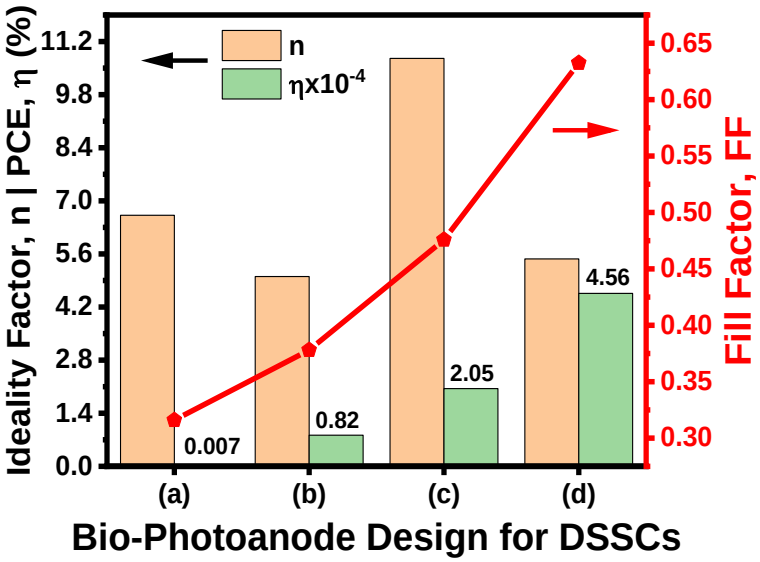

Figure 5.8 Calculated ideality factor (n), power conversion efficiency (PCE), and fill factor (FF) for β-carotene-sensitized and/or $MAPbI_3$ cosensitized DSSCs, or as shown for the various DSSCs with different spin-coated photoanodes (a)-(d) from Figure 5.6.

5.4 Series and Shunt Resistances of Bio/Co-Sensitized DSSCs

Series resistance (R_s) and shunt resistance (R_{sh}) were estimated from the linear relations obtained from the dark diode curves using Cheung's methods [243], [245] equation: $\frac{dV}{d\ln(I)} = IR_s + \left(\frac{nk_BT}{q}\right)$, and the J-V curves as $R_s = -[\Delta V_{oc}/\Delta I_{oc}]$ and $R_{sh} = -[\Delta V_{sc}/\Delta I_{sc}]$, respectively, where I=J here, and subscripts: oc and sc refer to open-circuit and short-circuit, respectively [246].

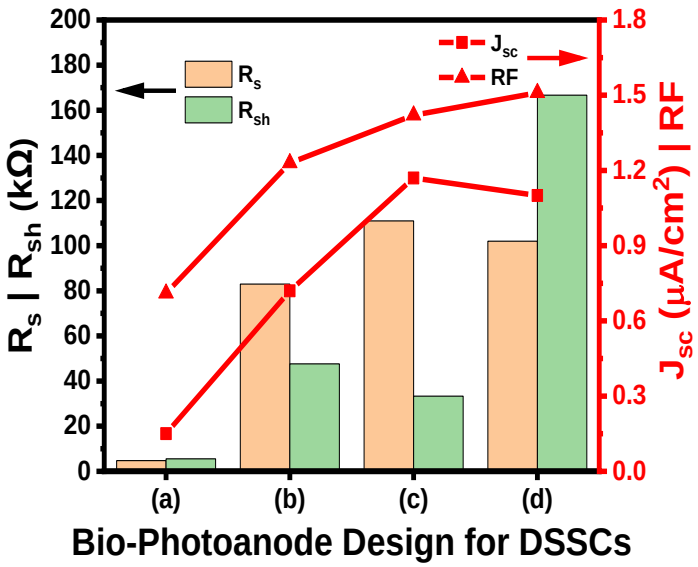

Figure 5.9 R_s, R_{sh}, J_{sc}, and RF observed in β-carotene-sensitized and/or $MAPbI_3$ cosensitized DSSCs, or as shown for the various DSSCs with different spin-coated photoanodes (a)-(d) from Figure 5.6.

From the J-V curves, maximum power points were determined and taken as reference to obtain the two linear lines at V_{oc} and J_{sc} locations. For efficient cells and high currents, R_s should be low for better electron injection and R_{sh} must be high enough to prevent current leakage. Both [$MAPbI_3$+β-carotene] enhanced R_{sh} (but with increased R_s) yielding in relatively high RF and J_{sc} (Figure 5.9). V_{oc} has been improved from the noticeable decrease in Φ_{SBH} at ITO/TiO_2 (from 0.61 to 0.53 eV) from addition of both [$MAPbI_3$ + β-carotene] sensitizers which prevented back-electron transport, and increased excitons generation and electron injection rates (Table 5.1). The sensitized/cosensitized photoanode active layers and the other designed cell architectures including β-carotene are illustrated in Figure 5.1(A-D).

Chapter 6: Photoanode UV-Vis Absorbance and Charge Transport Mechanisms

Maddah, H. A., Aryadwita, L., Berry, V., & Behura, S. K. (2020). Perovskite Cosensitization for Reduced Voltage Loss in Naturally-Sensitized Solar Cells, ***Nano Energy,*** Under-Review.

6.1 UV-Vis Absorbance and Tauc Plots for Photosensitizers Bandgaps Estimation

6.1.1 Introduction

Ultraviolet-visible (UV-Vis) spectroscopy is a common analytical technique that passes light through a sample and the transmittance of light by a sample is measured. This would also allow to detect nearly every molecule in the sample. From the transmittance (T), the absorbance can be calculated as A=-log (T). An absorbance spectrum is obtained that shows the absorbance of a compound at different wavelengths. The amount of absorbance at any wavelength is due to the chemical structure of the molecule. Most known molecules can absorb light energy in the UV-Vis wavelength range. The UV extends from 100–400 nm and the visible spectrum from 400–700 nm; whereas the 100–200 nm range is called the deep UV. Typical UV-Vis spectrometers use a deuterium lamp for the UV that produces light from 170–375 nm and a tungsten filament lamp for visible, which produces light from 350–2500 nm [247]. When a UV-visible light photon hits a molecule and is absorbed, the molecule is promoted into a more excited energetic state such that from the highest occupied molecular orbital (HOMO) to the lowest unoccupied molecular orbital (LUMO). Bandgap is the energy difference between the HOMO and the LUMO and/or bonding and anti-bonding orbitals. Each material has its unique bandgap based on its chemical and molecular structures. The most common transitions that fall in the UV-Vis range are π-π^* and n-π^*. The π orbitals arise due to double bonds, and the n orbitals are for non-bonding electrons. The π^* are anti-bonding pi orbitals. Therefore, the best UV-Vis

absorption is by molecules that contain double bonds. Typically, absorption increases with many π orbitals adjacent to each other and are connected creating conjugation. Absorption follows Beer's Law, $A=\varepsilon bC$ where ε is the molar attenuation coefficient, b is path length, and C is concentration. The molar attenuation coefficient is the characteristic of an individual compound to absorb at a given wavelength and this property is due to functional groups, conjugation, etc. Path length is generally related to the size of the cuvette and is 1 cm in standard spectrophotometers. The absorbance wavelength can be chosen using a filter or a monochromator, which is a device that separates the wavelengths of light spatially and then places an exit slit where the desired wavelength of light is [247].

6.1.2 Samples Preparation

Absorption spectrum analysis were carried out for the active photoanode materials ($MAPbI_3$, TiO_2, and β-Carotene), which typically absorb photons in the UV-Vis spectrum. Absorption spectrums of photoactive materials were measured using UV-Vis spectrometer (SSEYL UV-5100, ±2nm). Deionized water was used as a reference solution for the baseline of the absorption spectrum of $MAPbI_3$ and TiO_2, whereas THF-solvent was used as a reference solution for β-carotene absorption measurements. First, DI-water (10 mL) reference solution spectrum was measured for baseline correction. Then, a drop of $MAPbI_3$ or TiO_2 was added to one of the two separate cuvettes filled with DI (10 mL), put in front of the UV-Vis light to measure the absorption spectrum. Similarly, a drop of β-carotene was added to THF-solvent (10 mL) reference solution for β-carotene spectrum analysis. Three runs of each solution were carried out for accurate measurements. Lastly, calculations of the cumulative fit peak for all three solutions results were done to check for the photoanode optimal wavelength absorption abilities as well as absorption maximums.

6.1.3 Results and Discussion

Tauc plots for the wide bandgap (WBG) semiconductor and the sensitizers (Figure 6.3, Figure 6.4, and Figure 6.5), obtained from UV-Vis absorbance curves (Figure 6.1 and Figure 6.2) and the linearized Tauc Equation $\alpha\hbar\nu = A\left(\hbar\nu - E_g\right)^{1/2}$[248], are used to fit the absorption spectrum for direct allowed transition bandgaps of TiO_2, $MAPbI_3$, and β-carotene. Despite that $MAPbI_3$ is considered a direct bandgap semiconductor due to the high VB density of state, an indirect bandgap exists from spin-orbit coupling owing to CB Rashba-splitting [249]; where α is the absorption coefficient, $\hbar\nu$ is the photon energy, A is a constant, and E_g is the bandgap; α is calculated from: $\alpha = (2.303t) * OD$ where t is the thickness of the quartz cuvette (light path), 2.303 is the conversion constant between log(x) and ln(x) and OD is the optical density (UV/Vis absorbance) [249].

Absorbance curves from Figure 6.1 showed maximum absorption (λ_{max}) for TiO_2 at 297, 378 cm^{-1}, $MAPbI_3$ at 295, 1000.1 cm^{-1}, and β-carotene at 218, 343, 421, 479 cm^{-1} confirming that TiO_2 absorbs light mostly from the UV-region whereas sensitization fosters visible-light absorption. Cumulative peaks fitting (Gaussian fitting in ORIGIN, Figure 6.2) from the sub-fitted peaks of TiO_2 and both β-carotene and $MAPbI_3$ sensitizers would lead to minimum of 2-fold increase in the photoanode light absorption capabilities in the 200–600 UV-Vis spectrum, explaining the high observed performance in cosensitized DSSCs.

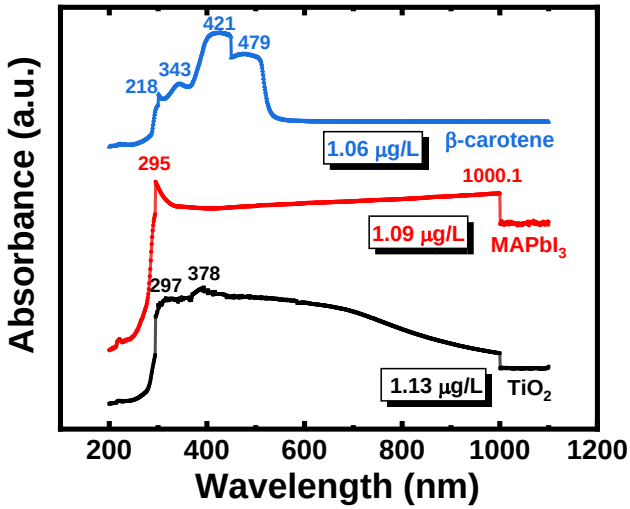

Figure 6.1 Absorbance curves for TiO_2 and sensitizers in H_2O solutions used in β-carotene-sensitized $MAPbI_3$-cosensitized DSSCs showing absorbance maximum of each material.

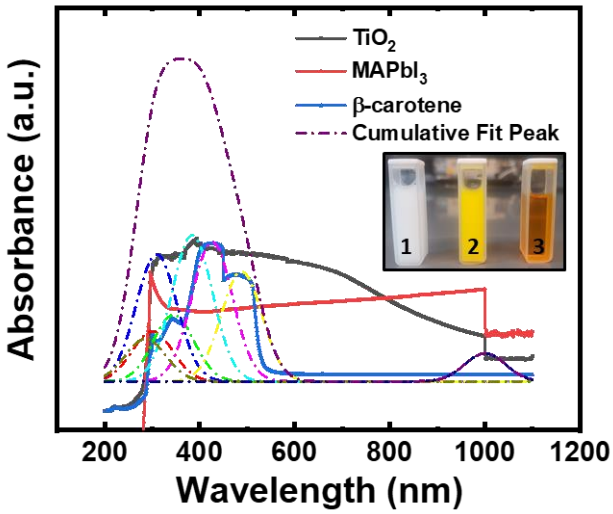

Figure 6.2 Cumulative peaks Gaussian fitting of the sub-fitted peaks of TiO_2 and sensitizers used in β-carotene-sensitized $MAPbI_3$-cosensitized DSSCs, showing 2-fold increase in the photoanode light absorption within 200–600 UV-Vis spectrum, inset: (1) TiO_2, (2) $MAPbI_3$, (3) β-carotene.

First-principle density functional theory (DFT) calculation showed that anatase behaves as an indirect transition bandgap semiconductor with high photocatalytic activity. Indirect transition ensures longer photogenerated exciton lifetime. Anatase is characterized with the lightest average effective mass phase yielding in faster electron

migration from TiO_2 to ITO with minimum recombination rates within TiO_2 [250]. WBG TiO_2 was observed with a direct bandgap of 3.34 eV (Figure 6.3) that is equivalent to the reported 3.3 eV for TiO_2 nanoparticles utilized by Kumar et al. in naturally-cosensitized DSSC [Jambolana + Eosin dye] with 0.13% PCE [251], where absorbance lies in the UV region. Organic–inorganic $MAPbI_3$ direct bandgap was found to be 1.87 eV (Figure 6.4), which agrees with the Guo et al. reported literature range (1.53 to 2.1 eV) [252].

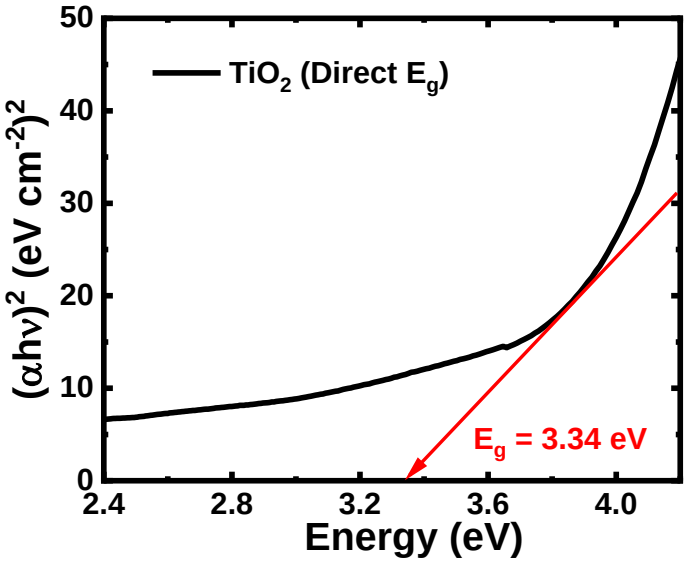

Figure 6.3 Tauc plot for TiO_2 semiconductor showing direct bandgap = 3.34 eV, obtained from absorbance curves for TiO_2 used later in β-carotene-sensitized $MAPbI_3$-cosensitized DSSCs.

An estimated direct bandgap of 2.29 eV (Figure 6.5) was obtained for β-carotene; this is smaller than the maximum reported direct bandgap of 3.74 eV (1.59 eV for indirect transition) for β-carotene in the fabricated x(SnO_2)-y(Ag)-β-carotene/ITO photoanode [86], [253]. However, other works estimated the HOMO/LUMO energy difference for various classes of carotene to be 2.2-6.7 eV [144]. Controllability of β-carotene bandgap is possible *via* incorporation of Ag/SnO_2 nanoparticles yielding β-carotene nanocomposite with lower E_g for its application in DSSCs, giving better molecular-dye electron excitation

[253]. Regarding the TiO_2, increasing semiconductor annealing temperature can blue-shift energies (decreasing bandgap); while, a decrease in semiconductor grain size decrease E_g due to electron quantum confinement [254].

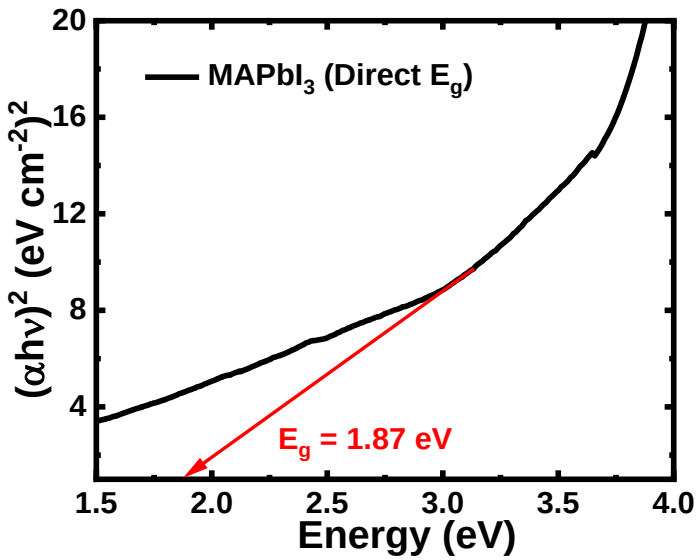

Figure 6.4 Tauc plot for $MAPbI_3$ semiconductor showing direct bandgap = 1.87 eV, obtained from absorbance curves for $MAPbI_3$ used later in β-carotene-sensitized $MAPbI_3$-cosensitized DSSCs.

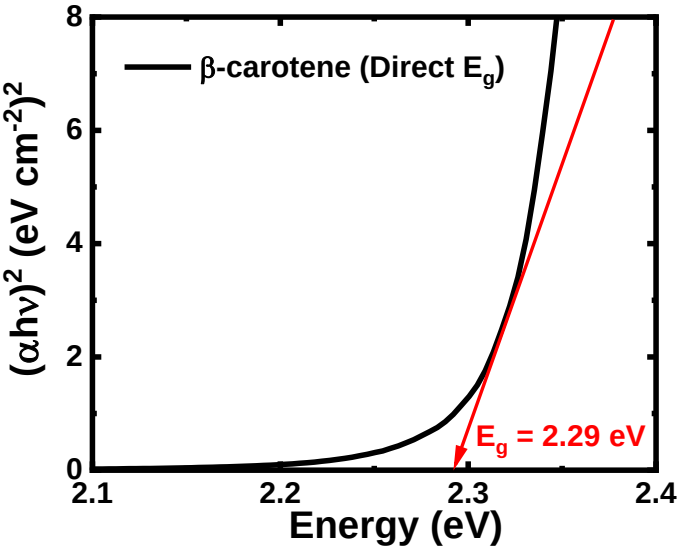

Figure 6.5 Tauc plot for β-carotene dye showing direct bandgap = 2.29 eV, obtained from absorbance curves for β-carotene dye used later in β-carotene-sensitized $MAPbI_3$-cosensitized DSSCs.

6.2 Voltage Loss at TiO_2/ITO and Hypothesized Charge Transport Mechanisms

6.2.1 Thermionic Emission and Cheung's Models

In a heterojunction diode structure, values like ideality factor (n), dark saturation and/or leakage current (J_0) [where, J_0=I_0/Area], and series resistance (R_s) are important for cell performance characterization. In DSSCs, thermionic emission (TE) [242] and Cheung's methods [243], [245] can be used to quantify the diode parameters. A Schottky diode exists in DSSCs at the metal-semiconductor interface in the photoanode structure as in ITO/TiO_2 or [Cu/ITO]/TiO_2 junctions. TE model has been used to determine both n and J_0 as shown in Eq. (13) from the exponential fitting [$y = a\exp(bx)$; $J_0 \rightarrow 0$]. Moreover. TE model can determine the Schottky-barrier height (Φ_{Bo}) as shown in Eq. (14) to Eq. (15); where A is the diode effective area and A* is Richardson constant from free electrons carriers' mass (120 A cm^{-2} K^{-2}) [243], [255]. For ideal structures ideality factor (n = 1); however, usually n > 1 due to recombination and R_s from interfacial contacts [242], [243], [256], [257].

$$J = J_0 \exp\left(\frac{q\mathrm{V}}{nk_BT}\right) \tag{13}$$

$$I_0 = AA^*T^2 \exp\left(-\frac{q\Phi_{Bo}}{k_BT}\right) \tag{14}$$

$$n = \frac{q}{k_BT}\left(\frac{dV}{d\ln \mathrm{I}}\right) \; ; \; \Phi_{Bo} = \frac{k_BT}{q}\ln\left(\frac{AA^*T^2}{I_o}\right) \tag{15}$$

According to Cheung's method, n, Φ_{Bo}, and R_s can be determined from [242], [243], [256], [257]:

$$\frac{dV}{d\ln(I)} = IR_s + \left(\frac{nk_BT}{q}\right) \tag{16}$$

$$H(I) = V - \left(\frac{nk_BT}{q}\right) ln\left(\frac{I}{AA^*T^2}\right) = IR_s + n\Phi_{Bo} \tag{17}$$

6.2.2 Voltage Loss from SBH at TiO_2/ITO and Max V_{oc} Correlated to TiO_2 Electrons

As mentioned earlier, In DSSCs there exists a Schottky diode at the metal-semiconductor interface in the photoanode structure as in ITO/TiO_2 or [Cu/ITO]/TiO_2 junctions. Onodera et al. [258]–[260] showed that V_{oc} decreased with increasing Schottky barrier height (ϕ_{SBH}). When TiO_2 comes in contact with ITO, band bending in TiO_2 CB occurs influencing current-loss mechanism from inhibited electron collection or increased recombination in agreement with thermionic-emission theory [260].

Voltage loss from ϕ_{SBH} at the ITO/TiO_2 interface (n-type semiconductor/metal) results from internal resistance and recombination current with the electrolyte; Onodera et al. [258]–[260] showed that the V_{oc} decreased with increasing the ϕ_{SBH}. Onodera et al. (2011) [258] proposed Eq. (19) to relate experimentally observed V_{oc} (V) to Schottky barrier height (SBH=ϕ_{SBH}) at the TiO_2/ITO interface ($\emptyset_{TiO_2-ITO}$); with the assumption that Fermi-level and conduction-band energies in TiO_2 are approximately the same. This assumption is valid due to the intrinsic n-type behavior of TiO_2 ($E_f \approx E_{CB}$), where one may estimate the maximum theoretical V_{oc} ($V_0 \approx 1$ V).

$$V = V_0 - V_1 \tag{18}$$

$$V_1 = \frac{k_B T}{q} \ln\left[1 + \frac{J_{cell}}{A^* T^2 \exp\left(-q\emptyset_{TiO_2-ITO}/k_B T\right)}\right] \tag{19}$$

$$J_{cell} = J_1 + J_2 \tag{20}$$

$$j_1 = qD_e \frac{dn}{dz} \tag{21}$$

$$J_1 = j_{1-TiO2} + j_{1-MAPbI3} \tag{22}$$

$$J_2 = q\frac{p}{\tau}(D_3 - 3D_1)\frac{dC_3}{dz} \tag{23}$$

where V_0 is the maximum theoretical V_{oc} could be obtained from the cell, V_1 is the voltage loss at TiO_2/ITO interface, and V is the experimental (actual) measured V_{oc}, A* is the Richardson constant of TiO_2 equal to 6.71×10^6 A m^{-2} K^{-2} [258], $\emptyset_{TiO_2-ITO}$ is the Schottky barrier height at the TiO_2/ITO interface, J_1 is the apparent current density in the TiO_2 porous structure, J_2 the total apparent current density in the electrolyte solution ($J_2 = J_{I^-} + J_{I_3^-}$), D_e is the effective electron diffusion coefficient, n is the electron concentration, z is the thickness of TiO_2 film, p is the porosity, τ is the tortuosity, D_1 and D_3 are the effective diffusion coefficients of I^- and I_3^-, respectively, (Redox reaction: $I_3^- + 2e^- \rightleftarrows 3I^-$), and C_3 is the ion concentration of I_3^- (0.75 M). Using Eq. (18) to Eq. (23) taken from ref. [258], the below calculation procedure is proposed to find out V_1, $\emptyset_{TiO_2-ITO}$, j_2 from j_1, and p/τ for the designed cosensitized and bio-molecularly sensitized DSSCs.

Calculations procedures (proposed and established) for V_1, $\emptyset_{TiO_2-ITO}$, J_1 and J_2 of the structured (bio/co)-sensitized DSSCs:

(i) Determine V_1 (lost voltage at TiO_2/ITO interface) from maximum theoretical V_{oc} (V_0) and experimentally observed V_{oc} (V) using Eq. (18).

(ii) Calculate $\emptyset_{TiO_2-ITO}$ from the total current density in the cell (J) and V_1 from Eq. (19).

(iii) Estimate j_1 in TiO_2 layer from the known (number of electrons=n_e=12,500 for 0.5 μm^3 TiO_2 [258]) that is equivalent to ($n_e=6\times10^{12}$ for 240×10^6 μm^3 TiO_2 layer volume in our system), $D_e=1.24\times10^{-4}$ cm^2 s^{-1} [258] and z=1.2 µm (as compared to ~3.5-15 µm film for anatase TiO_2 from literature [261]) for TiO_2 film, and $q=1.602\times10^{-18}$ C, plugged into Eq. (21).

(iv) Estimate j_1 in $MAPbI_3$ perovskite layer from the known (photogenerated carrier density 10^{17} cm^{-3} for $MAPbI_3$ from literature [262] and $400\text{x}10^6$ μm^3 volume for $MAPbI_3$ layer in our system) to get $n=4\times10^{13}$, with the known average $MAPbI_3$ D_e=0.03 cm^2 s^{-1} [263] and z=2 µm for $MAPbI_3$ film, and $q=1.602\times10^{-18}$ C, plugged into Eq. (21).

(v) Calculate the overall current J_1 flowing in the photoanode active layers from Eq. (22).

(vi) Back-calculate J_2 from using Eq. (20) with the known and/or experimentally observed J_{cell}; where that is equivalent to $J_{cell} = J_{sc}$ ($V_{cell} = 0$).

We can also get the ratio p/τ from Eq. (23) from concentration of redox, C_3, $[I^-/I_3^-]$ and their diffusion coefficients, and the calculated J_2.

Fermi energy (E_F) and vacuum level (E_V) correspond to the work function (Φ) of either the semiconductor or the metal, Eq. (24). The work function corresponds to the minimum amount of energy needed to remove an electron from the metal. However, the work function in semiconductors is different from the ionization energy in metals (energy difference between valence bands maximum (VBM) and vacuum level). In a

semiconductor, valence bands (E_{VB}) and conduction bands (E_{CB}) are separated by the bandgap (Eg), and the Fermi level becomes a somewhat theoretical construct since there are no allowed electronic states within the bandgap, which is a statistical function that gives the probability to find an electron in a given electronic state. The Fermi level or E_F refers to the point on the energy scale where the probability is just 50%, knowing that the valence bands are filled with electrons up to the Fermi energy. Nondegenerate semiconductors (having a moderate doping level) have their Fermi levels located within the bandgap [264].

The barrier between the metal and the semiconductor can be identified on an energy band diagram. To construct such diagram, we first consider the energy band diagram of the metal as well as the semiconductor and align them using the same vacuum level. As the metal and semiconductor are brought together, the difference in Fermi energies yield in band bending [265]. Band bending implies an electric field and, therefore, a potential difference across the junction. This "built-in" potential (V_{bi}) which can be determined from Eq. (25), where E_{F_2} and E_{F_1} refers to the Fermi energies of both the n-type semiconductor and the metal (or p-type semiconductor), respectively. This "built-in" potential is directly correlated to the difference in the Fermi levels on the two sides of the junction. This is clear because the bands need to bend due to this potential, so that the Fermi level is constant and flat throughout the device in equilibrium [266]. The barrier height (ϕ_{SBH}) is defined as the potential difference between the Fermi energy of the metal and the band edge where the majority carriers reside, as shown in Eq. (26) for an *n*-type semiconductor, where Φ_M is the work function of the metal and χ is the electron affinity of the semiconductor. A metal-semiconductor junction will therefore form a barrier for electrons and holes if the Fermi energy of the metal is somewhere between the conduction and valence band edge [265].

$$\Phi = E_V - E_F \tag{24}$$

$$V_1 = \mathrm{qV_{bi}} = E_{F_2} - E_{F_1} \tag{25}$$

$$\phi_{SBH} = \Phi_M - \chi \approx \phi_{TiO_2} - \phi_{ITO} \tag{26}$$

In addition to that the built-in potential is the difference between the Fermi energy of the metal and that of the semiconductor, V_{bi} is defined for n-type semiconductor as in Eq. (27) [265].

$$V_{bi} = \Phi_M - \chi - \frac{E_{CB} - E_F}{q} \tag{27}$$

The dark equilibrium density (n_{eq}) can be found using the expression from Andrande et al. [267] in Eq. (28), which gives n_{eq}= 1.87x10^5 cm^{-3} from E_{CB}-E_{redox}=0.93 eV, based on the literature value of the density of conduction band electrons N_{CB} (1x10^{21} cm^{-3}) in the semiconductor, where E_{CB} is the conduction band energy, E_R is the redox energy, k_B and T have been previously defined [267]. Similarly, the same equation can be rearranged and written in terms of E_F-E_{CB} = -0.272 eV (for n-type TiO_2), to calculate effective density of states of conduction band electrons or N_{CB} (2.46x10^{21} cm^{-3}) in TiO_2 from carrier concentration in the conduction band n_0=2.5x10^{16} cm^{-3} from knowing (number electrons=n_e=12,500 for 0.5 µm^3 TiO_2 [258] that is equivalent to n_e=6×10^{12} for 240×10^6 µm^3 TiO_2 layer volume in our system), Eq. (29) [85].

$$n_{eq} = N_{CB} \exp\left(-\frac{E_{CB} - E_R}{K_B T}\right) \tag{28}$$

$$E_F = E_{CB} + k_B T \ln \frac{n_0}{N_{CB}} \tag{29}$$

The work function of TiO_2 has been estimated in the two cells before (0) and after (1) photoanode perovskite cosensitization and from being correlated to the obtained fraction of reduced SBH, Eq. (30). The maximum V_{oc}^{*}=V_0 from the cell can be calculated from Eq. (31). Considering the produced voltage (V_2) from the semiconductor using the estimated Eq. (32), a new formulated equation can be used to theoretically estimate the actual or experimentally-tested cell output $V_{oc}|_{\exp}$, with x_1=x_2=0.5 as shown in Eq. (33).

$$\phi_{TiO_2}\big|_1 = \left(\frac{\phi_{SBH}|_0}{\phi_{SBH}|_1}\right) \times \phi_{TiO_2}\big|_0 \tag{30}$$

$$V_{oc}^{*} = V_0 = \frac{E_F - E_R}{q} \tag{31}$$

$$V_2 = E_{CB} - E_F \tag{32}$$

$$V_{oc}|_{\exp} \approx x_1(V_0 - V_1) + x_2 V_2 \tag{33}$$

6.2.3 Theoretical Conversion Efficiency and Band Diagram Alignment

Maximum theoretical PCE of <0.1% (spin-coated) and <0.7% (dip-coated) are estimated from the maximum theoretical V_{oc} = 1 V plugged into [$V_{oc} = \frac{nk_BT}{q}\ln\left(\frac{J_{ph}}{J_0}\right)$] and [$\eta^* = \frac{P_m}{P_{in}}$] according to DSSCs circuit and TE models (see Appendix B); where symbols definitions can be found in Appendix B. β-carotene deposited dye on TiO_2-photoanodes and their use in the different designed/fabricated DSSCs are shown in Figure 5.1(A-D), respectively. Post-annealed and created ITO/rGO CEs for lower R_s are shown in Figure 3.3(B). Energy band diagram alignment illustrated in Figure 6.6 shows perfect energy cascading for enhanced photoanode electron mobility, reduced interfacial recombination, and continuous forward electron pathways. The low bandgaps of both β-carotene (2.29

eV) and $MAPbI_3$ (1.87 eV) assure visible-light absorption, with their LUMO (-2.55 eV) and CB (-3.75 eV), respectively, relatively in higher states than TiO_2 CB (-4.2 eV) for more exciton generation and easy electron injection with a maximum ideal V_{oc} = 1 V. Low excitation energy requirements in the sensitizers ensure easy electron excitation and injection above the Fermi level of TiO_2. The large difference between HOMO/redox potentials drives electron-diffusion which effectively control charge injection and dye reduction rates [69].

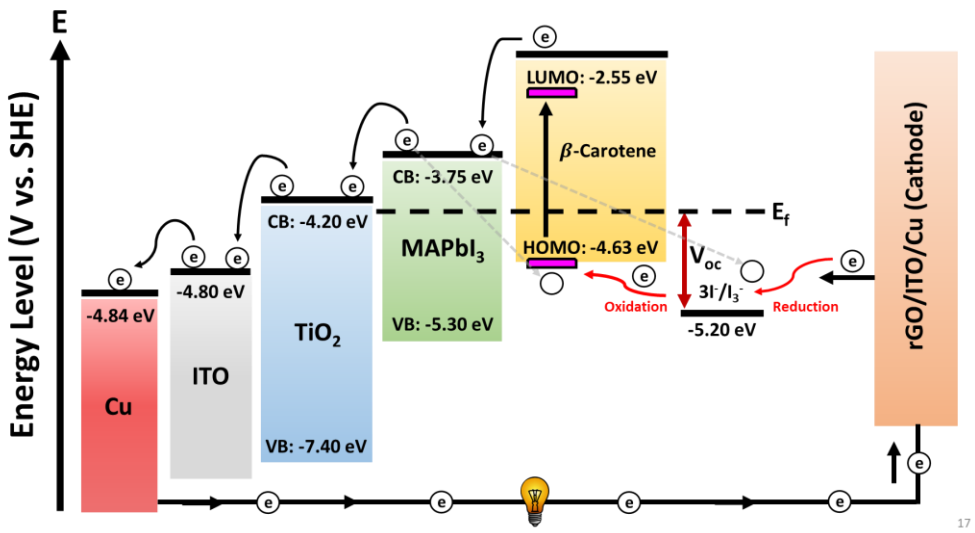

Figure 6.6 Energy levels and band diagram alignment for the sensitized/co-sensitized photoanode with perfect energy cascading for enhanced carriers mobility owing to the visible-absorption and low bandgaps of β-carotene and $MAPbI_3$.

6.2.4 HTL/ETL Theory and Improved Charge Transport from $MAPbI_3$ Cosensitization

Perovskite-based mesoporous solar cells typically consist of conductive electrodes, an electron transport layer (ETL), a mesoporous oxide layer (TiO_2), a perovskite layer, a hole transport layer (HTL). Solution spin-coating of perovskites on TiO_2 layer forms an interconnected absorbing layer and allows the perovskite nanocrystals to penetrate the pores of mesoporous, which transport electrons, block holes, and inhibit electron-hole recombination [268].

A schematic for the hypothesized HTL/ETL theory for exciton generation and charge transport is shown in Figure 6.7. According to Zhou et al. (2018) [268] and as illustrated in Figure 6.7, the basic roles of ETL and HTL in the charge transport are as follows:

(i) Electron Transport Layer (ETL): The basic function of the electron transport layer is to form an electron-selective contact with the perovskite light-absorbing layer to improve the extraction efficiency of photo-generated electrons, and to effectively prevent the hole from migrating to the counter electrode, enhancing the carrier's separation effect and to reducing the recombination.

(ii) Hole Transport Layer (HTL): The main role of the hole transport layer is to collect and transport holes from the perovskite light-absorbing layer to promote the separation of the electron-hole pairs, where the HOMO must match the valence band of perovskite materials for hole transport.

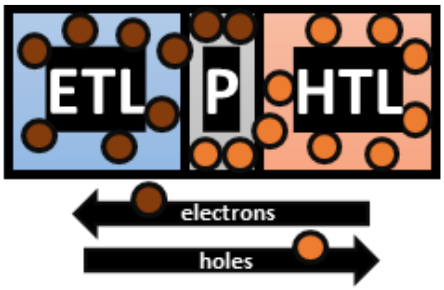

Figure 6.7 Hypothesized HTL/ETL (or HTL/P=Perovskite/ETL) theory for exciton generation and charge transport across the presumed built-in potential.

Like the p-n junction in conventional silicon solar cells, the DSSCs herein is hypothesized to have both HTL (p-type) and ETL (n-type) layers and when they come in contact, a depletion region is formed and there will be very few mobile electrons and holes in the depletion region, Figure 6.8. This region will only have the fixed charges associated with the dopant atoms exist, making it highly resistive and act a as a nearly perfect

insulator. The "built-in" electric field in the depletion region can be overcome by "applying" an external electric field opposite to the direction of the "built-in" electric field. This would result in thinner and less resistive depletion region, which considered to operate as a voltage-controlled resistor. In forward bias, if a positive voltage is applied to the p-type side and a negative voltage to the n-type side, current can flow (depending upon the magnitude of the applied voltage). If the applied voltage is large enough, the depletion region's resistance becomes negligible and current flows virtually unimpeded [269].

Typically, DSSCs without perovskite have a (i) depletion region between the n-type TiO_2 semiconductor (ETL) and redox electrolyte (HTL), and a (ii) depletion region between ITO/TIO_2 [258], [270], [271]. We may consider the dye component to generate its excitons in the HTL layer, and similarly for the $MAPbI_3$ cosensitizers, since these perovskites are observed as a hole conductor in HTM-free perovskite solar cells (PSCs). Many similarities arise between different solar cells [Si-cells, PSCs, and DSSCs], except that we have in DSSCs a redox electrolyte since it is an electrochemical cell sensitized with a molecular dye component, knowing that ETL= n-type, HTL=p-type [258], [270]–[272].

A perovskite solar cell can be either with mesoscopic or planar structure, our cell here is a n-i-p planer type (from SEM results), and since $MAPbI_3$ has both electron and hole transport features, the cell follows the HTL/P/ETL structure [271]. There will be no depletion region with TiO_2 if perovskite is an intrinsic semiconductor without n-type or p-type property [272]. However, another possibility arises in co-sensitized perovskite solar cells (including perovskite DSSCs) that there will be depletion layer created at the $CH_3NH_3PbI_3/TiO_2$ interface, considering perovskite as a hole conductor as observed in HTM-free PSCs [273].

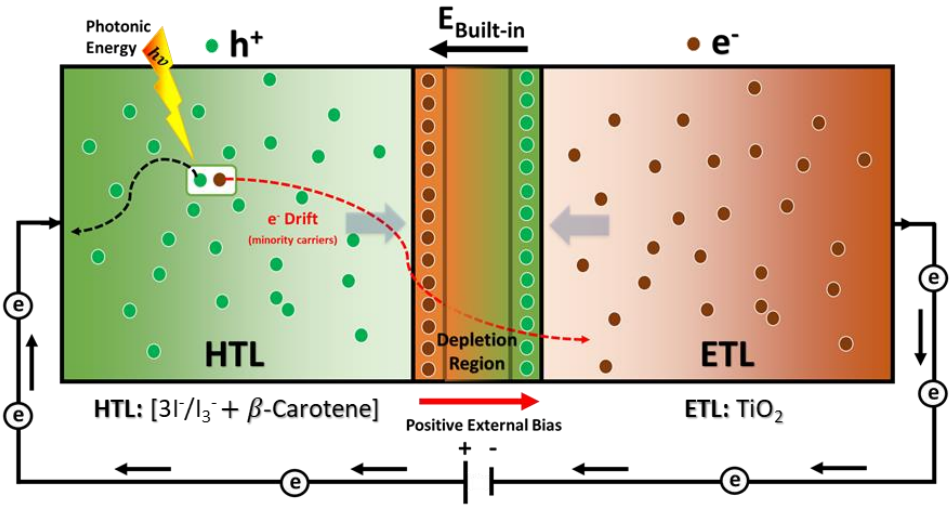

Figure 6.8 Excitons generation and charge transport mechanisms in perovskite-cosensitized DSSCs under illumination and/or forward bias; ETL: electron transport layer (TiO_2); HTL: hole-transport layer (β-carotene/[I^-/I_3^-]); in ETL/P/HTL.

When light shines on the DSSCs, they can generate current and voltage. The reason this can happen is because of dye excitation and the "built-in" electric field at the HTL/ETL junction (whether between dye/TiO_2 or even at a large-scale in the junction shown in Figure 6.8). The light has enough energy to excite both dye and semiconductors electrons into higher energy states creating excitons followed by charge separation, electron injection, and transport from anode (HTL) to cathode (ETL) for conventional current generation (from the p-type side to the n-type side). Created excitons in the HTL layer are free electron-hole pairs because for every electron excited by the light there is a corresponding hole generated, which both remains excited and free to move throughout the material for a short period of time before recombination occurs and electrons lose electrical energy as heat [269]. Electron drifting is the dominant electron transport mechanism when the cell is short-circuited for current generation as shown in Figure 6.8, while electron diffusion driving force becomes weak. Upon illumination, excited electrons in the HTL drifts towards the ETL layer, due to the moderate electric field existing in the depletion region.

Further, the existing electrons in the ETL move through the external load to the cathode for current generation. The current from the solar cell is the difference between the light-generated current and the forward bias current [244].

Under open-circuit conditions, the forward bias of the junction increases to a point where the light-generated current is exactly balanced by the forward bias diffusion current, and the net current is zero. The light-generated carriers forward bias the junction, thus increasing the diffusion current. Since the drift and diffusion current are in opposite direction, there is no net current from the solar cell at open circuit. In this scenario, both diffusion and drift mechanisms play equal roles in charge transport where light-generated carriers are prevented from leaving the solar cell and that collection of carriers causes an increase in the number of electrons on the n-type side of the p-n junction and a similar increase in holes in the p-type material. The separation of charge creates an electric field opposite to that already existing at the junction, reaching a new equilibrium in which light-generated current balancing diffusion current and a voltage exists across the p-n junction (yielding in generating high built-in potential equivalent to the cell voltage) [244].

Perovskite cosensitization can promote the β-carotene sensitized-photoanode light-harvesting ability addressing both TiO_2 CB bending and voltage loss problems. Perovskite cosensitization mitigates interfacial recombination and CB bending in TiO_2 (reduced ϕ_{SBH}) due to the $CH_3NH_3PbI_3/TiO_2$ interactions. Strong van der Waals interactions ensure fast electron injection completed within 100 fs (with possible improved dye attachment on $MAPbI_3$), where $CH_3NH_3PbI_3/TiO_2$ covalent bonding facilitates photoexcitation of charge-separated states leading to ultrafast interfacial charge separation prior to electron injection [229].

We suspect that there are three mechanisms, as illustrated in Figure 6.9(A,B) before/after perovskite sensitization, responsible for the improved PCE from $MAPbI_3$ cosensitization:

(i) Absorbance expansion and increase in the probability of absorbing more visible-photons (400–700 nm) [70].

(ii) Upward shifting of TiO_2 Fermi level due to increased injected electrons and CB effective density of states (>2.46×10^{21} cm^{-3}) reducing the TiO_2 work function (4.82 eV), consequently preventing back-electron transport allowing only quantum tunneling of photoelectrons at ITO/TiO_2, rather than transport over a Schottky barrier [88], [274], Figure 6.9(A,B).

(iii) Hindered ϕ_{SBH} at the ITO/TiO_2 interface with a 13.1% reduction in photoinduced electrostatic potential barrier due to the minimized band bending of TiO_2 CB and reduced TiO_2 work function resulting in low built-in potential and lower voltage loss (V_1).

All of the discussed mechanisms are attributed to possible ITO/TiO_2 electron tunneling from the increased number of initially injected electrons from perovskite and dye molecules into TiO_2 CB [260], [275]. Briefly, this upward shifting in E_F level for TiO_2 promotes both electrons tunneling and V_{oc} while decreasing the minimum work function (ϕ_{TiO_2}) required for electron excitation. Injected electrons tunnel from TiO_2 to ITO overcoming the suppressed ϕ_{SBH} at the presumed junction with hindered TiO_2 CB band bending resulting in less recombination and high V_{oc} [276]–[278] from the $MAPbI_3$ cosensitization.

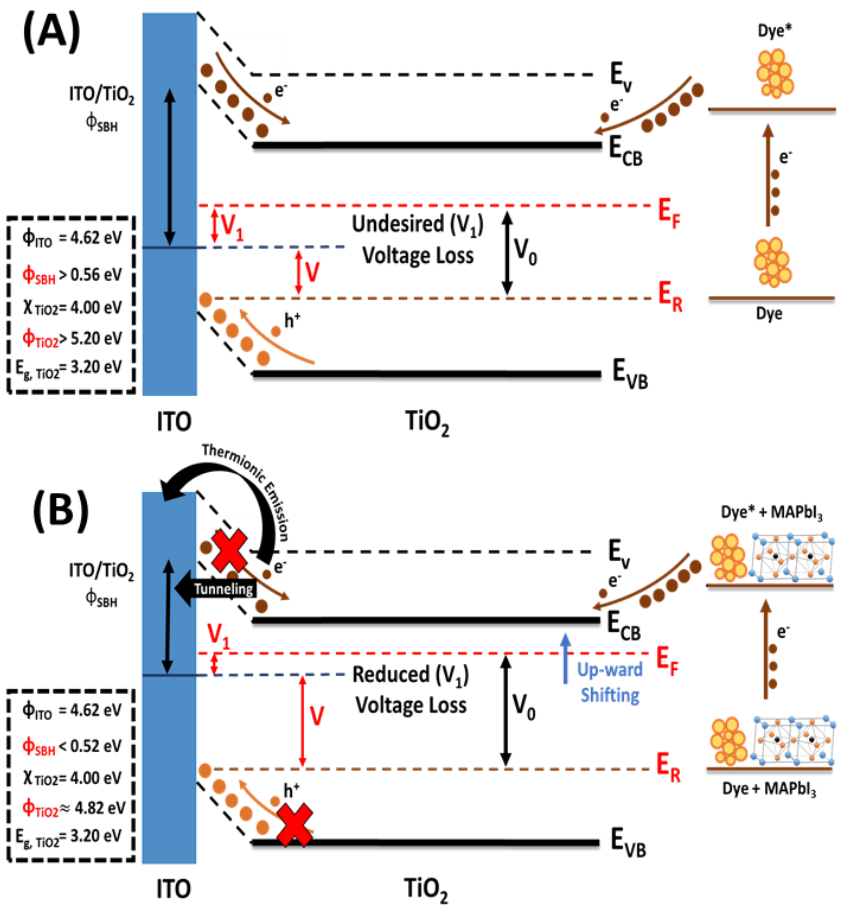

Figure 6.9 (A) TiO_2 Fermi level and ITO/TiO_2 SBH before $MAPbI_3$ cosensitization; **(B)** Upward shifting of TiO_2 Fermi level after $MAPbI_3$ cosensitization minimizing ITO/TiO_2 SBH for reduced voltage loss (V_1) and prevented back-electron transport to TiO_2.

6.2.5 Discussion

The voltage loss from ϕ_{SBH} at the ITO/TiO_2 interface arise from internal resistance and recombination current with the electrolyte; thus, the V_{oc} decreased with increasing the ϕ_{SBH}. When TiO_2 comes in contact with ITO, band bending in TiO_2 CB occurs influencing current-loss mechanism from inhibited electron collection. In other words, As the metal and semiconductor are brought together, the difference in Fermi energies yield in band bending. Band bending implies an electric field and, therefore, a potential difference across the junction. This "built-in" potential is directly correlated to the difference in the Fermi levels on the two sides of the junction.

Fermi energy and vacuum level corresponds to the work function of either the semiconductor or the metal. However, the work function in semiconductors is different from the ionization energy in metals. In a semiconductor, valence bands and conduction bands are separated by the bandgap , and the Fermi level becomes a somewhat theoretical construct since there are no allowed electronic states within the bandgap, which is a statistical function that gives the probability to find an electron in a given electronic state. We have suggested a calculations procedure for determining V_1, $\emptyset_{TiO_2-ITO}$, J_1 and J_2 of the structured (bio/co)-sensitized DSSCs based on the discussed concepts and common theoretical models.

The barrier height can also be defined as the potential difference between the Fermi energy of the metal and the band edge where the majority carriers reside. A metal-semiconductor junction will therefore form a barrier for electrons and holes if the Fermi energy of the metal is somewhere between the conduction and valence band edge. We calculated the effective density of states of conduction band electrons or N_{CB} (2.46×10^{21} cm^{-3}) in TiO_2 from carrier concentration in the conduction band. The work function of TiO_2 has been estimated in the two cells before (0) and after (1) photoanode perovskite cosensitization and from being correlated to the obtained fraction of reduced SBH. A new formulated equation is proposed to be used to theoretically estimate the actual or experimentally-tested cell output. Maximum theoretical PCE of <0.1% (spin-coated) and <0.7% (dip-coated) are estimated from the maximum theoretical V_{oc} = 1 V. Energy band diagram alignment showed perfect energy cascading for enhanced photoanode electron mobility, reduced interfacial recombination, and continuous forward electron pathways. The low bandgaps of both β-carotene (2.29 eV) and $MAPbI_3$ (1.87 eV) assure visible-light

absorption for more exciton generation and easy electron injection with a maximum ideal V_{oc} = 1 V.

Like the p-n junction in conventional silicon solar cells, the DSSCs herein is hypothesized to have both HTL (p-type) and ETL (n-type) layers and when they come in contact, a depletion region is formed and there will be very few mobile electrons and holes in the depletion region. The basic function of the electron transport layer is to form an electron-selective contact with the perovskite light-absorbing layer, while the main role of the hole transport layer is to collect and transport holes from the perovskite light-absorbing layer to promote the separation of the electron-hole pairs. Electron drifting is found to be the dominant electron transport mechanism when the cell is short-circuited for current generation. Upon illumination, excited electrons in the HTL drifts towards the ETL layer, due to the moderate electric field existing in the depletion region. Further, the existing electrons in the ETL move to the cathode for current generation. The current from the solar cell is the difference between the light-generated current and the forward bias current.

Perovskite cosensitization can promote the β-carotene sensitized-photoanode light-harvesting ability addressing both TiO_2 CB bending and voltage loss problems. Perovskite cosensitization mitigates interfacial recombination and CB bending in TiO_2 (reduced ϕ_{SBH}) due to the $CH_3NH_3PbI_3/TiO_2$ interactions. We suspect that there are three mechanisms responsible for the improved PCE from $MAPbI_3$ cosensitization: (i) absorbance expansion, (ii) upward shifting of TiO_2 Fermi level due to increased injected electrons and CB effective density of states (>2.46×10^{21} cm^{-3}) reducing the TiO_2 work function (4.82 eV), and (iii) hindered ϕ_{SBH} at the ITO/TiO_2 interface with a 13.1% reduction in photoinduced electrostatic potential barrier.

Chapter 7: Conclusions and Recommendations

Maddah, H. A., Aryadwita, L., Berry, V., & Behura, S. K. (2020). Perovskite Cosensitization for Reduced Voltage Loss in Naturally-Sensitized Solar Cells, ***Nano Energy,*** Under-Review.

7.1 Thesis Summary

We demonstrated the concept of natural photosensitization using bio-sensitized TiO_2 photoanodes which were further cosensitized by $MAPbI_3$ perovskites for enhanced photon absorption, exciton generation, charge separation, and electron injection resulting in reduced voltage loss. The hybrid dye-perovskite photoanode heterostructure [TiO_2/$MAPbI_3$/β-carotene] is believed to extend the photoanode absorption spectrum and reduce interfacial recombination, and most importantly facilitating interfacial charge separation, electron injection, and electron tunneling which reduced voltage loss at the presumed junction (ITO/TiO_2) for enhanced $V_{oc.}$

7.2 Contribution and Recommendations

The observed results were attributed to the upward shifting in E_F level for TiO_2, TiO_2 minimized work function, and hindered TiO_2 CB bending. Perovskite-integrated photoanode structures found to enhance diode ideality, reduce leakage current, improve cell rectification factors, increase FF, and noticeably show high V_{oc} (>0.65 V), from shifting E_F level and lowering ϕ_{SBH}. The low cell current densities are due to the unfavorable high series resistances need further investigation on the created interfacial contacts with the possibility of using noble-Pt-like CE for better electron collection.

Moreover, cosensitization prevents back-electron transport which also facilitate exciton generation, electron injection, and the possibility of 2-fold increase in photoanode UV-Vis absorption capabilities. This thesis paves the way towards designing efficient bio/co-sensitized photoanodes, which can be further improved from incorporation of WBG

low-dimensional materials, solid-state HTL redox electrolytes, and Ag/Au plasmonic nanoparticles leveraging photon absorption, electron injection and hopping, dye regeneration, and interfacial charge transport for an improved overall cell performance.

7.3 Directions for Future Works

Lastly, more focused future works for this research and/or thesis area include: (i) utilization of acidic dye solutions and/or surface hydroxylation of TiO_2 semiconductor (to introduce more –OH anchoring groups) for strong dye molecules acceptor-moieties attachment yielding in lower series resistance, (ii) designing of 3D graphene-based counter electrodes with interconnected networks to provide fast electron transport from cathode, diminished contact resistance at the graphene/electrolyte interface, and high electrocatalytic activity towards reduction of I_3^-, and (iii) incorporation of low-dimensional WBG 1D-ZnO nanowires ensuring large surface area for better dye coverage, high V_{oc}, and enhanced photoanode stability against excessive UV radiation.

CITED LITERATURE

[1] S. Shafiee and E. Topal, "When will fossil fuel reserves be diminished?," *Energy Policy*, 2009.

[2] B. Parida, S. Iniyan, and R. Goic, "A review of solar photovoltaic technologies," *Renewable and Sustainable Energy Reviews*. 2011.

[3] X. Pi, L. Zhang, and D. Yang, "Enhancing the efficiency of multicrystalline silicon solar cells by the inkjet printing of silicon-quantum-dot ink," *J. Phys. Chem. C*, 2012.

[4] H. F. W. Dekkers, L. Carnel, and G. Beaucarne, "Carrier trap passivation in multicrystalline Si solar cells by hydrogen from SiNx:H layers," *Appl. Phys. Lett.*, 2006.

[5] M. Lipiński, P. Panek, Z. Witek, E. Beltowska, and R. Ciach, "Double porous silicon layer on multi-crystalline Si for photovoltaic application," in *Solar Energy Materials and Solar Cells*, 2002.

[6] E. Klampaftis and B. S. Richards, "Improvement in multi-crystalline silicon solar cell efficiency via addition of luminescent material to EVA encapsulation layer," *Prog. Photovoltaics Res. Appl.*, 2011.

[7] D. Sarti and R. Einhaus, "Silicon feedstock for the multi-crystalline photovoltaic industry," *Sol. Energy Mater. Sol. Cells*, 2002.

[8] N. K. Noel *et al.*, "Lead-free organic-inorganic tin halide perovskites for photovoltaic applications," *Energy Environ. Sci.*, 2014.

[9] L. Tzounis, T. Stergiopoulos, A. Zachariadis, C. Gravalidis, A. Laskarakis, and S. Logothetidis, "Perovskite solar cells from small scale spin coating process towards roll-to-roll printing: Optical and Morphological studies," in *Materials Today: Proceedings*, 2017.

[10] W. Zhang, G. E. Eperon, and H. J. Snaith, "Metal halide perovskites for energy applications," *Nature Energy*. 2016.

[11] M. Liu, M. B. Johnston, and H. J. Snaith, "Efficient planar heterojunction perovskite solar cells by vapour deposition," *Nature*, 2013.

[12] N. G. Park, "Perovskite solar cells: An emerging photovoltaic technology," *Materials Today*. 2015.

[13] M. A. Green, A. Ho-Baillie, and H. J. Snaith, "The emergence of perovskite solar cells," *Nature Photonics*. 2014.

[14] H. Zhou *et al.*, "Interface engineering of highly efficient perovskite solar cells," *Science (80-.).*, 2014.

[15] G. Hodes, "Perovskite-based solar cells," *Science*. 2013.

[16] H. S. Jung and N. G. Park, "Perovskite solar cells: From materials to devices," *Small*. 2015.

[17] M. Tao, "Inorganic Photovoltaic Solar Cells: Silicon and Beyond," *Electrochem. Soc.*

Interface, 2008.

[18] R. W. Miles, G. Zoppi, and I. Forbes, "Inorganic photovoltaic cells," *Mater. Today*, 2007.

[19] B. E. McCandless and J. R. Sites, "Cadmium Telluride Solar Cells," in *Handbook of Photovoltaic Science and Engineering*, 2011.

[20] J. Britt and C. Ferekides, "Thin-film CdS/CdTe solar cell with 15.8% efficiency," *Appl. Phys. Lett.*, 1993.

[21] X. Wu, "High-efficiency polycrystalline CdTe thin-film solar cells," *Sol. Energy*, 2004.

[22] M. Kaelin, D. Rudmann, and A. N. Tiwari, "Low cost processing of CIGS thin film solar cells," *Sol. Energy*, 2004.

[23] R. Wuerz *et al.*, "CIGS thin-film solar cells on steel substrates," *Thin Solid Films*, 2009.

[24] T. Wada *et al.*, "High-efficiency CIGS solar cells with modified CIGS surface," *Sol. Energy Mater. Sol. Cells*, 2001.

[25] E. Cuce, C.-H. Young, and S. B. Riffat, "Thermal performance investigation of heat insulation solar glass: A comparative experimental study," *Energy Build.*, 2015.

[26] T. Ameri, G. Dennler, C. Lungenschmied, and C. J. Brabec, "Organic tandem solar cells: A review," *Energy and Environmental Science*. 2009.

[27] S. Albrecht *et al.*, "Solution processed organic tandem solar cells," in *Energy Procedia*, 2011.

[28] A. Hadipour, B. De Boer, and P. W. M. Blom, "Organic tandem and multi-junction solar cells," *Adv. Funct. Mater.*, 2008.

[29] T. Ameri, N. Li, and C. J. Brabec, "Highly efficient organic tandem solar cells: A follow up review," *Energy and Environmental Science*. 2013.

[30] M. Riede *et al.*, "Efficient organic tandem solar cells based on small molecules," *Adv. Funct. Mater.*, 2011.

[31] L. Meng *et al.*, "Organic and solution-processed tandem solar cells with 17.3% efficiency," *Science (80-.).*, 2018.

[32] K. Tvrdy and P. V. Kamat, "Quantum Dot Solar Cells," in *Comprehensive Nanoscience and Technology*, 2010.

[33] R. A. Taylor and K. Ramasamy, "Colloidal quantum dots solar cells," *SPR Nanosci.*, 2017.

[34] Z. Pan, H. Rao, I. Mora-Seró, J. Bisquert, and X. Zhong, "Quantum dot-sensitized solar cells," *Chemical Society Reviews*. 2018.

[35] P. V. Kamat, "Quantum dot solar cells. Semiconductor nanocrystals as light harvesters," *J. Phys. Chem. C*, 2008.

[36] A. J. Nozik, M. C. Beard, J. M. Luther, M. Law, R. J. Ellingson, and J. C. Johnson,

"Semiconductor Quantum Dots and Quantum Dot Arrays and Applications of Multiple Exciton Generation to Third-Generation Photovoltaic Solar Cells," *Chem. Rev.*, 2010.

[37] Z. Ning *et al.*, "Quantum-dot-in-perovskite solids," *Nature*, 2015.

[38] B. O'Regan and M. Grätzel, "A low-cost, high-efficiency solar cell based on dye-sensitized colloidal TiO2 films," *Nature*, 1991.

[39] Y. Koyama, T. Miki, X. F. Wang, and H. Nagae, "Dye-sensitized solar cells based on the principles and materials of photosynthesis: Mechanisms of suppression and enhancement of photocurrent and conversion efficiency," *International Journal of Molecular Sciences*. 2009.

[40] L. Kavan, "Electrochemistry and dye-sensitized solar cells," *Current Opinion in Electrochemistry*. 2017.

[41] A. Hagfeldt, "Brief overview of dye-sensitized solar cells," in *Ambio*, 2012.

[42] T. Bessho, S. M. Zakeeruddin, C. Y. Yeh, E. W. G. Diau, and M. Gr??tzel, "Highly efficient mesoscopic dye-sensitized solar cells based on donor-acceptor-substituted porphyrins," *Angew. Chemie - Int. Ed.*, 2010.

[43] K. V. Hemalatha, S. N. Karthick, C. Justin Raj, N. Y. Hong, S. K. Kim, and H. J. Kim, "Performance of Kerria japonica and Rosa chinensis flower dyes as sensitizers for dye-sensitized solar cells," *Spectrochim. Acta - Part A Mol. Biomol. Spectrosc.*, 2012.

[44] S. Ito *et al.*, "High-conversion-efficiency organic dye-sensitized solar cells with a novel indoline dye," *Chem. Commun.*, 2008.

[45] B. Tan, E. Toman, Y. Li, and Y. Wu, "Zinc stannate (Zn2SnO4) dye-sensitized solar cells," *J. Am. Chem. Soc.*, 2007.

[46] K. Woronowicz *et al.*, "Near-IR absorbing solar cell sensitized with bacterial photosynthetic membranes," *Photochem. Photobiol.*, 2012.

[47] S. M. Feldt, E. A. Gibson, E. Gabrielsson, L. Sun, G. Boschloo, and A. Hagfeldt, "Design of organic dyes and cobalt polypyridine redox mediators for high-efficiency dye-sensitized solar cells," *J. Am. Chem. Soc.*, 2010.

[48] C. Dette *et al.*, "TiO 2 Anatase with a Bandgap in the Visible Region," *Nano Lett.*, vol. 14, no. 11, pp. 6533–6538, 2014.

[49] V. Sugathan, E. John, and K. Sudhakar, "Recent improvements in dye sensitized solar cells: A review," *Renewable and Sustainable Energy Reviews*. 2015.

[50] M. R. Narayan, "Review: Dye sensitized solar cells based on natural photosensitizers," *Renewable and Sustainable Energy Reviews*. 2012.

[51] S. Mathew *et al.*, "Dye-sensitized solar cells with 13% efficiency achieved through the molecular engineering of porphyrin sensitizers," *Nat. Chem.*, 2014.

[52] H. Hug, M. Bader, P. Mair, and T. Glatzel, "Biophotovoltaics: Natural pigments in dye-sensitized solar cells," *Appl. Energy*, 2014.

[53] A. Molaeirad, S. Janfaza, A. Karimi-Fard, and B. Mahyad, “Photocurrent generation by adsorption of two main pigments of Halobacterium salinarum on TiO2nanostructured electrode,” *Biotechnol. Appl. Biochem.*, 2015.

[54] C. Y. Chen *et al.*, “Highly efficient light-harvesting ruthenium sensitizer for thin-film dye-sensitized solar cells,” *ACS Nano*, 2009.

[55] W. Wu *et al.*, “D-π-M-π-A structured platinum acetylide sensitizer for dye-sensitized solar cells,” *J. Mater. Chem.*, 2011.

[56] N. Órdenes-Aenishanslins, G. Anziani-Ostuni, M. Vargas-Reyes, J. Alarcón, A. Tello, and J. M. Pérez-Donoso, “Pigments from UV-resistant Antarctic bacteria as photosensitizers in Dye Sensitized Solar Cells,” *J. Photochem. Photobiol. B Biol.*, 2016.

[57] I. McConnell, G. H. Li, and G. W. Brudvig, “Energy Conversion in Natural and Artificial Photosynthesis,” *Chem. Biol.*, 2010.

[58] G. Richhariya, A. Kumar, P. Tekasakul, and B. Gupta, “Natural dyes for dye sensitized solar cell: A review,” *Renewable and Sustainable Energy Reviews*. 2017.

[59] N. T. R. N. Kumara, A. Lim, C. M. Lim, M. I. Petra, and P. Ekanayake, “Recent progress and utilization of natural pigments in dye sensitized solar cells: A review,” *Renewable and Sustainable Energy Reviews*. 2017.

[60] N. Sawhney, A. Raghav, and S. Satapathi, “Utilization of Naturally Occurring Dyes as Sensitizers in Dye Sensitized Solar Cells,” *IEEE J. Photovoltaics*, 2017.

[61] S. A. Mozaffari, M. Saeidi, and R. Rahmanian, “Photoelectric characterization of fabricated dye-sensitized solar cell using dye extracted from red Siahkooti fruit as natural sensitizer,” *Spectrochim. Acta - Part A Mol. Biomol. Spectrosc.*, 2015.

[62] N. A. Ludin, A. M. Al-Alwani Mahmoud, A. Bakar Mohamad, A. A. H. Kadhum, K. Sopian, and N. S. Abdul Karim, “Review on the development of natural dye photosensitizer for dye-sensitized solar cells,” *Renewable and Sustainable Energy Reviews*. 2014.

[63] S. A. Agarkar *et al.*, “Isobutrin from butea monosperma (flame of the forest): A promising new natural sensitizer belonging to chalcone class,” *ACS Appl. Mater. Interfaces*, 2011.

[64] X. F. Wang *et al.*, “Dye-sensitized solar cells using retinoic acid and carotenoic acids: Dependence of performance on the conjugation length and the dye concentration,” *Chem. Phys. Lett.*, 2005.

[65] W. Stahl and H. Sies, “Antioxidant activity of carotenoids,” *Molecular Aspects of Medicine*. 2003.

[66] X. F. Wang, Y. Koyama, H. Nagae, Y. Yamano, M. Ito, and Y. Wada, “Photocurrents of solar cells sensitized by aggregate-forming polyenes: Enhancement due to suppression of singlet-triplet annihilation by lowering of dye concentration or light intensity,” *Chem. Phys. Lett.*, 2006.

[67] X. F. Wang *et al.*, “Effects of plant carotenoid spacers on the performance of a dye-

sensitized solar cell using a chlorophyll derivative: Enhancement of photocurrent determined by one electron-oxidation potential of each carotenoid," *Chem. Phys. Lett.*, 2006.

[68] H. Zhou, L. Wu, Y. Gao, and T. Ma, "Dye-sensitized solar cells using 20 natural dyes as sensitizers," *J. Photochem. Photobiol. A Chem.*, 2011.

[69] G. Calogero, J. H. Yum, A. Sinopoli, G. Di Marco, M. Grätzel, and M. K. Nazeeruddin, "Anthocyanins and betalains as light-harvesting pigments for dye-sensitized solar cells," *Sol. Energy*, 2012.

[70] M. Grätzel, "Conversion of sunlight to electric power by nanocrystalline dye-sensitized solar cells," *J. Photochem. Photobiol. A Chem.*, 2004.

[71] Q. Dai and J. Rabani, "Photosensitization of nanocrystalline TiO2films by anthocyanin dyes," *J. Photochem. Photobiol. A Chem.*, 2002.

[72] S. Hao, J. Wu, Y. Huang, and J. Lin, "Natural dyes as photosensitizers for dye-sensitized solar cell," in *Solar Energy*, 2006.

[73] S. Mori *et al.*, "Enhancement of incident photon-to-current conversion efficiency for phthalocyanine-sensitized solar cells by 3D molecular structuralization," *J. Am. Chem. Soc.*, 2010.

[74] T. Ikeuchi, H. Nomoto, N. Masaki, M. J. Griffith, S. Mori, and M. Kimura, "Molecular engineering of zinc phthalocyanine sensitizers for efficient dye-sensitized solar cells," *Chem. Commun.*, 2014.

[75] W. Wu, J. Hua, Y. Jin, W. Zhan, and H. Tian, "Photovoltaic properties of three new cyanine dyes for dye-sensitized solar cells," *Photochem. Photobiol. Sci.*, 2007.

[76] X. Ma *et al.*, "A high-efficiency cyanine dye for dye-sensitized solar cells," *Tetrahedron*, 2008.

[77] I. B. Karki, J. J. Nakarmi, P. K. Mandal, and S. Chatterjee, "Effect of organic dyes on the performance of ZnO based dye-sensitized solar cells," *Appl. Sol. Energy*, 2013.

[78] K. Hara *et al.*, "Design of new coumarin dyes having thiophene moieties for highly efficient organic-dye-sensitized solar cells," *New J. Chem.*, 2003.

[79] Z. S. Wang, Y. Cui, K. Hara, Y. Dan-Oh, C. Kasada, and A. Shinpo, "A high-light-harvesting-efficiency coumarin dye for stable dye-sensitized solar cells," *Adv. Mater.*, 2007.

[80] S. K. Behura, C. Wang, Y. Wen, and V. Berry, "Graphene–semiconductor heterojunction sheds light on emerging photovoltaics," *Nat. Photonics*, 2019.

[81] M. K. Nazeeruddin, E. Baranoff, and M. Grätzel, "Dye-sensitized solar cells: A brief overview," *Sol. Energy*, 2011.

[82] J. Gong, K. Sumathy, Q. Qiao, and Z. Zhou, "Review on dye-sensitized solar cells (DSSCs): Advanced techniques and research trends," *Renewable and Sustainable Energy Reviews*. 2017.

[83] L. Kavan, “Electrochemistry of titanium dioxide: Some aspects and highlights,” *Chem. Rec.*, 2012.

[84] J. Gong, J. Liang, and K. Sumathy, “Review on dye-sensitized solar cells (DSSCs): Fundamental concepts and novel materials,” *Renewable and Sustainable Energy Reviews*. 2012.

[85] T. Marinado, “Photoelectrochemical studies of dye-sensitized solar cells using organic dyes,” 2009.

[86] H. A. Maddah, V. Berry, and S. K. Behura, “Biomolecular photosensitizers for dye-sensitized solar cells: Recent developments and critical insights,” *Renewable and Sustainable Energy Reviews*. 2020.

[87] A. Hagfeldt and M. Grätzel, “Light-Induced Redox Reactions in Nanocrystalline Systems,” *Chem. Rev.*, 1995.

[88] S. Rühle and D. Cahen, “Electron tunneling at the TiO2/substrate interface can determine dye-sensitized solar cell performance,” *J. Phys. Chem. B*, 2004.

[89] J. B. Asbury, E. Hao, Y. Wang, H. N. Ghosh, and T. Lian, “Ultrafast Electron Transfer Dynamics from Molecular Adsorbates to Semiconductor,” *J. Phys. Chem. B*, 2001.

[90] A. R. Glenn, “Production of extracellular proteins by bacteria,” *Annu. Rev. Microbiol.*, vol. 30, no. 1, pp. 41–62, 1976.

[91] “Ribosome,” *Nature Education*, 2014. [Online]. Available: https://www.nature.com/scitable/definition/ribosome-194.

[92] “Ribosomes, Transcription, and Translation,” *Nature Education*, 2014. [Online]. Available: https://www.nature.com/scitable/topicpage/ribosomes-transcription-and-translation-14120660.

[93] G. K. Chandi and B. S. Gill, “Production and characterization of microbial carotenoids as an alternative to synthetic colors: A review,” *Int. J. Food Prop.*, 2011.

[94] J.-L. Barredo, *Microbial Carotenoids from Bacteria and Microalgae. Methods and Protocols*. 2012.

[95] K. Kirti, S. Amita, S. Priti, A. Mukesh Kumar, and S. Jyoti, “Colorful World of Microbes: Carotenoids and Their Applications,” *Adv. Biol.*, 2014.

[96] X. F. Wang *et al.*, “Dye-sensitized solar cells using a chlorophyll a derivative as the sensitizer and carotenoids having different conjugation lengths as redox spacers,” *Chem. Phys. Lett.*, 2005.

[97] Y. Lu *et al.*, “Photoelectric performance of bacteria photosynthetic proteins entrapped on tailored mesoporous WO3-TiO2films,” *Langmuir*, 2005.

[98] J. H. Caufield, M. Abreu, C. Wimble, and P. Uetz, “Protein Complexes in Bacteria,” *PLoS Comput. Biol.*, 2015.

[99] D. A. Bryant *et al.*, “Candidates Chloracidobacterium thermophilum: An aerobic

phototrophic acidobacterium," *Science (80-.).*, 2007.

[100] G. J. Magis *et al.*, "Light harvesting, energy transfer and electron cycling of a native photosynthetic membrane adsorbed onto a gold surface," *Biochim. Biophys. Acta - Biomembr.*, 2010.

[101] Q. Fu, C. Zhao, S. Yang, and J. Wu, "The photoelectric performance of dye-sensitized solar cells fabricated by assembling pigment-protein complexes of purple bacteria on nanocrystalline photoelectrode," *Mater. Lett.*, 2014.

[102] Y. Yang *et al.*, "Complete biosynthetic pathway of the C<inf>50</inf> carotenoid bacterioruberin from lycopene in the extremely halophilic archaeon Haloarcula japonica," *J. Bacteriol.*, 2015.

[103] M. F. Montagni, T., Enciso, P., Marizcurrena, J. J., Castro-Sowinski, S., Fontana, C., Davyt, D., & Cerdá, "Dye sensitized solar cells based on Antarctic Hymenobacter sp. UV11 dyes," *Environ. Sustain.*, pp. 1–9, 2018.

[104] S. K. Srivastava, P. Piwek, S. R. Ayakar, A. Bonakdarpour, D. P. Wilkinson, and V. G. Yadav, "A Biogenic Photovoltaic Material," *Small*, 2018.

[105] A. Mershin *et al.*, "Self-assembled photosystem-I biophotovoltaics on nanostructured TiO2and ZnO," *Sci. Rep.*, 2012.

[106] A. Kay and M. Graetzel, "Artificial photosynthesis. 1. Photosensitization of titania solar cells with chlorophyll derivatives and related natural porphyrins," *J. Phys. Chem.*, 1993.

[107] S. Ahmad, E. Guillén, L. Kavan, M. Grätzel, and M. K. Nazeeruddin, "Metal free sensitizer and catalyst for dye sensitized solar cells," *Energy and Environmental Science*. 2013.

[108] A. Mishra, M. K. Fischer, and P. Bauerle, "Metal-free organic dyes for dye-sensitized solar cells: from structure: property relationships to design rules," *Angew Chem Int Ed Engl*, 2009.

[109] E. Galoppini, "Linkers for anchoring sensitizers to semiconductor nanoparticles," *Coordination Chemistry Reviews*. 2004.

[110] K. Nagai, A., & Takagi, *Conjugated Objects: Developments, Synthesis, and Applications*. Pan Stanford, 2017.

[111] G. N. Lewis and M. Calvin, "The color of organic substances," *Chem. Rev.*, 1939.

[112] Samal, "A Brief Discussion on Color: Why does such conjugation allow absorption of visible light?," 2014. [Online]. Available: https://people.chem.umass.edu/samal/269/color.pdf.

[113] E. Daviso *et al.*, "The electronic structure of the primary electron donor of reaction centers of purple bacteria at atomic resolution as observed by photo-CIDNP 13C NMR.," *Proc. Natl. Acad. Sci. U. S. A.*, 2009.

[114] M. Fairhead, D. Shen, L. K. M. Chan, E. D. Lowe, T. J. Donohoe, and M. Howarth, "Love-Hate ligands for high resolution analysis of strain in ultra-stable protein/small

molecule interaction," *Bioorganic Med. Chem.*, 2014.

[115] F. Gai, K. C. Hasson, J. C. McDonald, and P. A. Anfinrud, "Chemical dynamics in proteins: The photoisomerization of retinal in bacteriorhodopsin," *Science (80-.).*, 1998.

[116] A. M. Dummer, J. C. Bonsall, J. B. Cihla, S. M. Lawry, G. C. Johnson, and R. F. Peck, "Bacterioopsin-Mediated regulation of bacterioruberin biosynthesis in Halobacterium salinarum," *J. Bacteriol.*, 2011.

[117] D. J. Kim, N. Takasuka, H. Nishino, and H. Tsuda, "Chemoprevention of lung cancer by lycopene," in *BioFactors*, 2000.

[118] B. P. Jelle, C. Breivik, and H. Drolsum Røkenes, "Building integrated photovoltaic products: A state-of-the-art review and future research opportunities," *Sol. Energy Mater. Sol. Cells*, 2012.

[119] L. P. Heiniger *et al.*, "See-through dye-sensitized solar cells: Photonic reflectors for tandem and building integrated photovoltaics," *Adv. Mater.*, 2013.

[120] D. Yu, G. Zhu, S. Liu, B. Ge, and F. Huang, "Photocurrent activity of light-harvesting complex II isolated from spinach and its pigments in dye-sensitized TiO2solar cell," *Int. J. Hydrogen Energy*, 2013.

[121] J. Chellamuthu, P. Nagaraj, S. G. Chidambaram, A. Sambandam, and A. Muthupandian, "Enhanced photocurrent generation in bacteriorhodopsin based bio-sensitized solar cells using gel electrolyte," *J. Photochem. Photobiol. B Biol.*, 2016.

[122] S. A. Trammell, L. Wang, J. M. Zullo, R. Shashidhar, and N. Lebedev, "Orientated binding of photosynthetic reaction centers on gold using Ni-NTA self-assembled monolayers," *Biosens. Bioelectron.*, 2004.

[123] J. Zhao, Y. Zou, B. Liu, C. Xu, and J. Kong, "Differentiating the orientations of photosynthetic reaction centers on Au electrodes linked by different bifunctional reagents," *Biosens. Bioelectron.*, 2002.

[124] D. C. Feher, G.; Allen, J. P.; Okamura, M. Y.; Rees, "Structue and function of bacterial photosynthetic reaction centeres," *Nature*, 1989.

[125] J. Deisenhofer and H. Michel, "The photosynthetic reaction center from the purple bacterium Rhodopseudomonas viridis," *Science (80-.).*, 1989.

[126] R. J. Franck, H., & Cogdell, "Photochemistry and function of carotenoids in photosynthesis," in *A. Young, G. Britton eds. Carotenoids in Photosynthesis.*, 1993.

[127] R. Koyama, Y., & Fujii, "Cis-trans carotenoids in photosynthesis: configurations, excited-state properties and physiological functions," in *The photochemistry of carotenoids*, Springer, Dordrecht, 1999, pp. 161–188.

[128] H. A. Frank and G. W. Brudvig, "Redox functions of carotenoids in photosynthesis," *Biochemistry*. 2004.

[129] S. Bhandari, D. Mondal, S. K. Nataraj, and R. G. Balakrishna, "Biomolecule-derived quantum dots for sustainable optoelectronics," *Nanoscale Adv.*, 2019.

[130] R. Mansour, “Natural Dyes and Pigments: Extraction and Applications,” in *Handbook of Renewable Materials for Coloration and Finishing*, 2018, pp. 75–102.

[131] K. Furuichi, T. Sashima, and Y. Koyama, “The first detection of the 3Ag- state in carotenoids using resonance-Raman excitation profiles,” *Chem. Phys. Lett.*, 2002.

[132] H. R. Shahmohammadi *et al.*, “Protective roles of bacterioruberin and intracellular KCl in the resistance of Halobacterium salinarium against DNA-damaging agents.,” *J. Radiat. Res.*, 1998.

[133] C. Gallardo *et al.*, “Low-temperature biosynthesis of fluorescent semiconductor nanoparticles (CdS) by oxidative stress resistant Antarctic bacteria,” *J. Biotechnol.*, 2014.

[134] D. O. Plaza, C. Gallardo, Y. D. Straub, D. Bravo, and J. M. Pérez-Donoso, “Biological synthesis of fluorescent nanoparticles by cadmium and tellurite resistant Antarctic bacteria: Exploring novel natural nanofactories,” *Microb. Cell Fact.*, 2016.

[135] I. J. Iwuchukwu, M. Vaughn, N. Myers, H. O’Neill, P. Frymier, and B. D. Bruce, “Self-organized photosynthetic nanoparticle for cell-free hydrogen production,” *Nat. Nanotechnol.*, 2010.

[136] G. B. Ferreira, E. Hollauer, N. M. Comerlato, and J. L. Wardell, “An experimental and theoretical study of the electronic spectra of tetraethylammonium [bis(1,3-dithiole-2-thione-4,5-dithiolato)M(III)] and tetraethylammonium [bis(1,3-dithiole-2-one-4,5-dithiolato)M(III)] (M = Sb or Bi),” *Spectrochim. Acta - Part A Mol. Biomol. Spectrosc.*, 2008.

[137] C. N. Ramachandran, D. Roy, and N. Sathyamurthy, “Host-guest interaction in endohedral fullerenes,” *Chem. Phys. Lett.*, 2008.

[138] I. Losito, F. Palmisano, and P. G. Zambonin, “o-phenylenediamine electropolymerization by cyclic voltammetry combined with electrospray ionization-ion trap mass spectrometry,” *Anal. Chem.*, 2003.

[139] S. Janietz, D. D. C. Bradley, M. Grell, C. Giebeler, M. Inbasekaran, and E. P. Woo, “Electrochemical determination of the ionization potential and electron affinity of poly(9,9-dioctylfluorene),” *Appl. Phys. Lett.*, 1998.

[140] Y.-S. Kim, J.-I. Shin, S.-Y. Park, K. Jun, and Y.-A. Son, “Electrochemical Studies on Heptamethine Cyanine Dyes,” *Text. Color. Finish.*, 2013.

[141] X. F. Wang, C. H. Zhan, T. Maoka, Y. Wada, and Y. Koyama, “Fabrication of dye-sensitized solar cells using chlorophylls c1 and c2 and their oxidized forms c1′ and c2′ from Undaria pinnatifida (Wakame),” *Chem. Phys. Lett.*, 2007.

[142] G. Calogero *et al.*, “Synthetic analogues of anthocyanins as sensitizers for dye-sensitized solar cells,” *Photochem. Photobiol. Sci.*, 2013.

[143] T. Ruiz-Anchondo, N. Flores-Holguín, and D. Glossman-Mitnik, “Natural carotenoids as nanomaterial precursors for molecular photovoltaics: A computational DFT study,” *Molecules*, 2010.

[144] J. B. L. Martins, J. A. Durães, M. J. A. Sales, A. S. F. A. Vilela, G. M. E. Silva, and R. Gargano, "Theoretical investigation of carotenoid ultraviolet spectra," *Int. J. Quantum Chem.*, 2009.

[145] X. F. Wang, H. Tamiaki, O. Kitao, T. Ikeuchi, and S. I. Sasaki, "Molecular engineering on a chlorophyll derivative, chlorin e6, for significantly improved power conversion efficiency in dye-sensitized solar cells," *J. Power Sources*, 2013.

[146] F. A. Castro *et al.*, "On the use of cyanine dyes as low-bandgap materials in bulk heterojunction photovoltaic devices," *Synth. Met.*, 2006.

[147] K. Liu *et al.*, "Spiro[fluorene-9,9′-xanthene]-based hole transporting materials for efficient perovskite solar cells with enhanced stability," *Mater. Chem. Front.*, 2017.

[148] Y. Qian *et al.*, "Spiro[fluorene-9,9′-xanthene]-based universal hosts for understanding structure-property relationships in RGB and white PhOLEDs," *RSC Adv.*, 2015.

[149] B. B. Carbas and A. M. Önal, "New fluorene-xanthene-based hybrid electrochromic and fluorescent polymers via donor-acceptor approach," *Electrochim. Acta*, 2012.

[150] R. Sánchez-De-Armas, M. Á. San Miguel, J. Oviedo, and J. F. Sanz, "Coumarin derivatives for dye sensitized solar cells: A TD-DFT study," *Phys. Chem. Chem. Phys.*, 2012.

[151] J. M. D. Agrawal, S., Dev, P., English, N. J., Thampi, K. R., & MacElroy, "First-principles study of the excited-state properties of coumarin-derived dyes in dye-sensitized solar cells," *J. Mater. Chem.*, vol. 21, no. 30, pp. 11101–11108, 2011.

[152] S. Tombe, G. Adam, H. Heilbrunner, H. Apaydin, E. Iwuoha, and M. C. Scharber, "Optical and electronic properties of mixed halide," pp. 1714–1723, 2017.

[153] H. Hu, T. Salim, B. Chen, and Y. M. Lam, "Molecularly Engineered Organic-Inorganic Hybrid Perovskite with Multiple Quantum Well Structure for Multicolored Light-Emitting Diodes," *Sci. Rep.*, 2016.

[154] H. Hu, T. Salim, B. Chen, and Y. M. Lam, "Molecularly Engineered Organic- Inorganic Hybrid Perovskite with Multiple Quantum Well Structure for Multicolored Light-Emitting Diodes," *Nat. Publ. Gr.*, no. September, pp. 1–8, 2016.

[155] C. C. Stoumpos *et al.*, "Ruddlesden − Popper Hybrid Lead Iodide Perovskite 2D Homologous Semiconductors," 2016.

[156] D. B. Mitzi, C. A. Feild, Z. Schlesinger, and R. B. Laibowitz, "Transport, optical, and magnetic properties of the conducting halide perovskite ch3nh3sni3," *J. Solid State Chem.*, 1995.

[157] H. Bloemen *et al.*, "ConductingLayeredOrganic-inorganicHalidesContaining(110)-OrientedPerovskite Sheets," *Science (80-.).*, 1995.

[158] W. Travis, E. N. K. Glover, H. Bronstein, D. O. Scanlon, and R. G. Palgrave, "On the application of the tolerance factor to inorganic and hybrid halide perovskites: A revised system," *Chem. Sci.*, 2016.

[159] J. Shi and S. Yun, “First-Principles DFT Calculations for Perovskite Solar Cells,” in *Counter Electrodes for Dye-sensitized and Perovskite Solar Cells*, 2018.

[160] H. A. Maddah, V. Berry, and S. K. Behura, “Cuboctahedral stability in Titanium halide perovskites via machine learning,” *Comput. Mater. Sci.*, 2020.

[161] G. Niu, W. Li, J. Li, X. Liang, and L. Wang, “RSC Advances Enhancement of thermal stability for perovskite solar cells through cesium doping †,” pp. 17473–17479, 2017.

[162] H. Tsai *et al.*, “High-efficiency two-dimensional Ruddlesden–Popper perovskite solar cells,” *Nat. Publ. Gr.*, vol. 536, no. 7616, pp. 312–316, 2016.

[163] and M. K. N. Peng Gao*, Michael Grätzel, “Environmental Science Organohalide lead perovskites for photovoltaic applications,” *Energy Environ. Sci.*, 2012.

[164] F. Deschler *et al.*, “High photoluminescence efficiency and optically pumped lasing in solution-processed mixed halide perovskite semiconductors,” *J. Phys. Chem. Lett.*, 2014.

[165] K. Wu *et al.*, “Temperature-dependent excitonic photoluminescence of hybrid organometal halide perovskite films,” *Phys. Chem. Chem. Phys.*, 2014.

[166] L. Tzounis, T. Stergiopoulos, A. Zachariadis, and C. Gravalidis, “ScienceDirect Perovskite solar cells from small scale spin coating process towards roll-to-roll printing : Optical and Morphological studies □,” *Mater. Today Proc.*, vol. 4, no. 4, pp. 5082–5089, 2017.

[167] S. Rutile *et al.*, “High E ffi ciency Solid-State Sensitized Solar Cell-Based on Submicrometer Rutile TiO 2 Nanorod and CH 3 NH 3 PbI 3 Perovskite Sensitizer,” 2013.

[168] A. Kojima, K. Teshima, Y. Shirai, and T. Miyasaka, “Organometal halide perovskites as visible-light sensitizers for photovoltaic cells,” *J. Am. Chem. Soc.*, 2009.

[169] J. H. Im, C. R. Lee, J. W. Lee, S. W. Park, and N. G. Park, “6.5% efficient perovskite quantum-dot-sensitized solar cell,” *Nanoscale*, 2011.

[170] K. Kakiage, T. Kyomen, and M. Hanaya, “Improvement in Photovoltaic Performance of Dye-sensitized Solar Cells by Cosensitization with an Organometal Halide Perovskite,” *Chem. Lett.*, 2013.

[171] H. S. Kim *et al.*, “High efficiency solid-state sensitized solar cell-based on submicrometer rutile TiO2 nanorod and CH3NH3PbI3 perovskite sensitizer,” *Nano Lett.*, 2013.

[172] A. Supriyanto, F. Nurosyid, and A. H. Ahliha, “Carotenoid pigment as sensitizers for applications of dye-sensitized solar cell (DSSC),” in *IOP Conference Series: Materials Science and Engineering*, 2018.

[173] C. Motta, F. El-Mellouhi, and S. Sanvito, “Charge carrier mobility in hybrid halide perovskites,” *Sci. Rep.*, 2015.

[174] W. Ning *et al.*, “Long Electron–Hole Diffusion Length in High-Quality Lead-Free Double Perovskite Films,” *Adv. Mater.*, 2018.

[175] E. Edri, S. Kirmayer, D. Cahen, and G. Hodes, “High open-circuit voltage solar cells

based on organic-inorganic lead bromide perovskite," *J. Phys. Chem. Lett.*, 2013.

[176] H. S. Kim *et al.*, "Lead iodide perovskite sensitized all-solid-state submicron thin film mesoscopic solar cell with efficiency exceeding 9%," *Sci. Rep.*, 2012.

[177] S. Ye *et al.*, "CuSCN-Based Inverted Planar Perovskite Solar Cell with an Average PCE of 15.6%," *Nano Lett.*, 2015.

[178] J. D. Roy-Mayhew and I. A. Aksay, "Graphene materials and their use in dye-sensitized solar cells," *Chemical Reviews*. 2014.

[179] S. Sun, L. Gao, and Y. Liu, "Enhanced dye-sensitized solar cell using graphene- TiO2 photoanode prepared by heterogeneous coagulation," *Appl. Phys. Lett.*, 2010.

[180] Y. H. Wang, H., & Hu, "Graphene as a counter electrode material for dye-sensitized solar cells," *Energy Environ. Sci.*, vol. 5, no. 8, pp. 8182–8188, 2012.

[181] K. S. Novoselov *et al.*, "Electric field effect in atomically thin carbon films.," *Science (80-.).*, 2004.

[182] X. Du, I. Skachko, A. Barker, and E. Y. Andrei, "Approaching ballistic transport in suspended graphene.," *Nat. Nanotechnol.*, 2008.

[183] A. Peigney, C. Laurent, E. Flahaut, R. R. Bacsa, and A. Rousset, "Specific surface area of carbon nanotubes and bundles of carbon nanotubes," *Carbon N. Y.*, 2001.

[184] R. R. Nair *et al.*, "Fine Structure Constant Defines Visual Transparency of Graphene," *Science (80-.).*, 2008.

[185] X. Wang, L. Zhi, and K. Müllen, "Transparent, conductive graphene electrodes for dye-sensitized solar cells," *Nano Lett.*, 2008.

[186] D. W. Zhang *et al.*, "Graphene-based counter electrode for dye-sensitized solar cells," *Carbon N. Y.*, 2011.

[187] H. Choi, H. Kim, S. Hwang, Y. Han, and M. Jeon, "Graphene counter electrodes for dye-sensitized solar cells prepared by electrophoretic deposition," *J. Mater. Chem.*, 2011.

[188] W. Hong, Y. Xu, G. Lu, C. Li, and G. Shi, "Transparent graphene/PEDOT-PSS composite films as counter electrodes of dye-sensitized solar cells," *Electrochem. commun.*, vol. 10, no. 10, pp. 1555–1558, 2008.

[189] G. Wang, S. Zhuo, and W. Xing, "Graphene/polyaniline nanocomposite as counter electrode of dye-sensitized solar cells," *Mater. Lett.*, 2012.

[190] K. S. Lee, Y. Lee, J. Y. Lee, J. H. Ahn, and J. H. Park, "Flexible and platinum-free dye-sensitized solar cells with conducting-polymer-coated graphene counter electrodes," *ChemSusChem*, 2012.

[191] F. Gong, H. Wang, and Z. S. Wang, "Self-assembled monolayer of graphene/Pt as counter electrode for efficient dye-sensitized solar cell," *Phys. Chem. Chem. Phys.*, 2011.

[192] M. Y. Yen *et al.*, "Platinum nanoparticles/graphene composite catalyst as a novel composite counter electrode for high performance dye-sensitized solar cells," *J. Mater.*

Chem., 2011.

[193] Y. Y. Dou, G. R. Li, J. Song, and X. P. Gao, "Nickel phosphide-embedded graphene as counter electrode for dye-sensitized solar cells," *Phys. Chem. Chem. Phys.*, 2012.

[194] J. Velten *et al.*, "Carbon nanotube/graphene nanocomposite as efficient counter electrodes in dye-sensitized solar cells," *Nanotechnology*, 2012.

[195] H. Wang, K. Sun, F. Tao, D. J. Stacchiola, and Y. H. Hu, "3D honeycomb-like structured graphene and its high efficiency as a counter-electrode catalyst for dye-sensitized solar cells," *Angew. Chemie - Int. Ed.*, 2013.

[196] X. Xu, D. Huang, K. Cao, M. Wang, S. M. Zakeeruddin, and M. Grätzel, "Electrochemically reduced graphene oxide multilayer films as efficient counter electrode for dye-sensitized solar cells," *Sci. Rep.*, 2013.

[197] Q. Chang *et al.*, "Graphene nanosheets@ZnO nanorods as three-dimensional high efficient counter electrodes for dye sensitized solar cells," *Electrochim. Acta*, 2015.

[198] G. Wang, W. Xing, and S. Zhuo, "Nitrogen-doped graphene as low-cost counter electrode for high-efficiency dye-sensitized solar cells," *Electrochim. Acta*, 2013.

[199] G. Yue *et al.*, "Platinum/graphene hybrid film as a counter electrode for dye-sensitized solar cells," *Electrochim. Acta*, 2013.

[200] N. M. N. Gomesh, A. H. Ibrahim, R. Syafinar, M. Irwanto, M. R. Mamat, Y. M Irwan, U. Hashim2, "Fabrication Of Dye Sensitized Solar Cell Using Various Counter Electrode Thickness," *Int. J. Ser. Eng. Sci.*, vol. 1, no. 1, pp. 49–65, 2015.

[201] I. A. Sahito, K. C. Sun, A. A. Arbab, M. B. Qadir, Y. S. Choi, and S. H. Jeong, "Flexible and conductive cotton fabric counter electrode coated with graphene nanosheets for high efficiency dye sensitized solar cell," *J. Power Sources*, 2016.

[202] H. Wang, K. Sun, F. Tao, D. J. Stacchiola, and Y. H. Hu, "3D honeycomb-like structured graphene and its high efficiency as a counter-electrode catalyst for dye-sensitized solar cells," *Angew. Chemie - Int. Ed.*, 2013.

[203] Y. S. Yen, H. H. Chou, Y. C. Chen, C. Y. Hsu, and J. T. Lin, "Recent developments in molecule-based organic materials for dye-sensitized solar cells," *J. Mater. Chem.*, 2012.

[204] U. Mehmood, S. U. Rahman, K. Harrabi, I. A. Hussein, and B. V. S. Reddy, "Recent advances in dye sensitized solar cells," *Advances in Materials Science and Engineering*. 2014.

[205] M. Papageorgiou, N.; Maier, W. F.; Grätzel, "An Iodine/Triiodide Reduction Electrocatalyst for Aqueous and Organic Media," *J. Electrochem. Soc.*, 1997.

[206] N. Papageorgiou, "An Iodine/Triiodide Reduction Electrocatalyst for Aqueous and Organic Media," *J. Electrochem. Soc.*, 2006.

[207] S. S. Kim, S. I. Na, J. Jo, D. Y. Kim, and Y. C. Nah, "Plasmon enhanced performance of organic solar cells using electrodeposited Ag nanoparticles," *Appl. Phys. Lett.*, 2008.

[208] X. Fang, T. Ma, G. Guan, M. Akiyama, T. Kida, and E. Abe, "Effect of the thickness of the Pt film coated on a counter electrode on the performance of a dye-sensitized solar cell," *J. Electroanal. Chem.*, 2004.

[209] N. Shasidharan, G. N., Ibrahim, A. H., Syafinar, R., Irwanto, M., Mamat, M. R., Irwan, Y. M., ... & Mariun, "Fabrication Of Dye Sensitized Solar Cell Using Various Counter Electrode Thickness.," *Int. J. Ser. Eng. Sci.*, vol. 1, no. 1, pp. 49–56, 2015.

[210] S. Sathyajothi, R. Jayavel, and A. C. Dhanemozhi, "The Fabrication of Natural Dye Sensitized Solar Cell (Dssc) based on TiO2 Using Henna and Beetroot Dye Extracts," in *Materials Today: Proceedings*, 2017.

[211] S. N. Alam, N. Sharma, and L. Kumar, "Synthesis of Graphene Oxide (GO) by Modified Hummers Method and Its Thermal Reduction to Obtain Reduced Graphene Oxide (rGO)*," *Graphene*, 2017.

[212] M. Rani and S. K. Tripathi, "Electron transfer properties of organic dye sensitized ZnO and ZnO/TiO2 photoanode for dye sensitized solar cells," *Renew. Sustain. Energy Rev.*, 2016.

[213] N. E. Craft and J. H. Soares, "Relative Solubility, Stability, and Absorptivity of Lutein and β-Carotene In Organic Solvents," *J. Agric. Food Chem.*, 1992.

[214] N. I. Zaaba, K. L. Foo, U. Hashim, S. J. Tan, W. W. Liu, and C. H. Voon, "Synthesis of Graphene Oxide using Modified Hummers Method: Solvent Influence," in *Procedia Engineering*, 2017.

[215] J. Guerrero-Contreras and F. Caballero-Briones, "Graphene oxide powders with different oxidation degree, prepared by synthesis variations of the Hummers method," *Mater. Chem. Phys.*, 2015.

[216] J. Chen, B. Yao, C. Li, and G. Shi, "An improved Hummers method for eco-friendly synthesis of graphene oxide," *Carbon N. Y.*, 2013.

[217] C. Quarti *et al.*, "The raman spectrum of the CH3NH3PbI3 hybrid perovskite: Interplay of theory and experiment," *J. Phys. Chem. Lett.*, 2014.

[218] P. Pistor, A. Ruiz, A. Cabot, and V. Izquierdo-Roca, "Advanced Raman Spectroscopy of Methylammonium Lead Iodide: Development of a Non-destructive Characterisation Methodology," *Sci. Rep.*, 2016.

[219] M. Ledinský *et al.*, "Raman spectroscopy of organic-inorganic halide perovskites," *J. Phys. Chem. Lett.*, 2015.

[220] L. Q. Xie *et al.*, "Organic-inorganic interactions of single crystalline organolead halide perovskites studied by Raman spectroscopy," *Phys. Chem. Chem. Phys.*, 2016.

[221] G. Singh Bumbrah and R. Mohan Sharma, "Raman spectroscopy and Basic principle, instrumentation and selected applications for the characterization of drugs of abuse," *Egypt. J. Forensic Sci.*, 2016.

[222] M. Omidi *et al.*, "Characterization of biomaterials," in *Biomaterials for Oral and Dental*

Tissue Engineering, 2017.

[223] "Techniques for Oral Microbiology," in *Atlas of Oral Microbiology*, 2015.

[224] F. D. Hardcastle, H. Ishihara, R. Sharma, and A. S. Biris, "Photoelectroactivity and Raman spectroscopy of anodized titania (TiO 2) photoactive water-splitting catalysts as a function of oxygen-annealing temperature," *J. Mater. Chem.*, 2011.

[225] P. Pistor *et al.*, "Recent Progress on the Long-Term Stability of Perovskite Solar Cells," *Adv. Sci.*, vol. 1379, no. June, pp. 1–8, 2016.

[226] M. A. Pérez-Osorio *et al.*, "Raman Spectrum of the Organic-Inorganic Halide Perovskite CH3NH3PbI3from First Principles and High-Resolution Low-Temperature Raman Measurements," *Journal of Physical Chemistry C*, 2018.

[227] Q. Lin *et al.*, "Raman Spectrum of the Organic − Inorganic Halide Perovskite CH 3 NH 3 PbI 3 from First Principles and High-Resolution Low- Temperature Raman Measurements," 2018.

[228] S. Thampy, B. Zhang, K.-H. Hong, K. Cho, and J. W. P. Hsu, " Altered Stability and Degradation Pathway of CH 3 NH 3 PbI 3 in Contact with Metal Oxide ," *ACS Energy Lett.*, 2020.

[229] R. Long, W. H. Fang, and O. V. Prezhdo, "Strong Interaction at the Perovskite/TiO2 Interface Facilitates Ultrafast Photoinduced Charge Separation: A Nonadiabatic Molecular Dynamics Study," *J. Phys. Chem. C*, 2017.

[230] J. Jehlička, H. G. M. Edwards, and A. Oren, "Raman spectroscopy of microbial pigments," *Applied and Environmental Microbiology*. 2014.

[231] N. Tschirner *et al.*, "Raman excitation profiles of β-carotene - Novel insights into the nature of the ν1-band," in *Physica Status Solidi (B) Basic Research*, 2008.

[232] S. Fang *et al.*, "Three-dimensional reduced graphene oxide powder for efficient microwave absorption in the S-band (2-4 GHz)," *RSC Adv.*, 2017.

[233] I. Childres, L. A. Jauregui, W. Park, H. Cao, and Y. Chen, "Raman Spectroscopy of Graphene and Related Materials," *New Dev. Phot. Mater. Res.*, 2013.

[234] A. Nakaruk, D. Ragazzon, and C. C. Sorrell, "Anatase-rutile transformation through high-temperature annealing of titania films produced by ultrasonic spray pyrolysis," *Thin Solid Films*, 2010.

[235] S. Sarker, H. W. Seo, and D. M. Kim, "Calculating current density-voltage curves of dye-sensitized solar cells: A straight-forward approach," *J. Power Sources*, 2014.

[236] J. Halme, P. Vahermaa, K. Miettunen, and P. Lund, "Device physics of dye solar cells," *Advanced Materials*. 2010.

[237] A. Jain and A. Kapoor, "A new approach to study organic solar cell using Lambert W-function," *Sol. Energy Mater. Sol. Cells*, 2005.

[238] A. Jain and A. Kapoor, "A new method to determine the diode ideality factor of real solar

cell using Lambert W-function," *Sol. Energy Mater. Sol. Cells*, 2005.

[239] H. Yu, S. Zhang, H. Zhao, G. Will, and P. Liu, "An efficient and low-cost TiO2 compact layer for performance improvement of dye-sensitized solar cells," *Electrochim. Acta*, 2009.

[240] P. J. Cameron, L. M. Peter, and S. Hore, "How important is the back reaction of electrons via the substrate in dye-sensitized nanocrystalline solar cells?," *J. Phys. Chem. B*, 2005.

[241] P. J. Cameron and L. M. Peter, "How does back-reaction at the conducting glass substrate influence the dynamic photovoltage response of nanocrystalline dye-sensitized solar cells?," *J. Phys. Chem. B*, 2005.

[242] P. K. Gupta, R. K., Ghosh, K., & Kahol, "Fabrication and electrical characterization of Au/p-Si/STO/Au contact," *Curr. Appl. Physics*, vol. 9, no. 5, pp. 933–936, 2009.

[243] H. K. Çavuş, M. M. Voigt, and R. Şahingöz, "Optical and electrical properties of new organic thin film," *J. Mater. Sci. Mater. Electron.*, 2013.

[244] C. Honsberg and B. Stuart, "The Photovoltaic Education Network," *PV Education*, 2018. [Online]. Available: https://www.pveducation.org/.

[245] N. Brutscher and M. Hoheisel, "Schottky diodes with high series resistance: A simple method of determining the barrier heights," *Solid State Electron.*, 1988.

[246] M. Diantoro, T. Suprayogi, A. Hidayat, A. Taufiq, A. Fuad, and R. Suryana, "Shockley's equation fit analyses for solar cell parameters from I-V curves," *Int. J. Photoenergy*, 2018.

[247] JoVE, "Ultraviolet-Visible (UV-Vis) Spectroscopy," *JoVE Science Education Database. Analytical Chemistry. Cambridge, MA.*, 2020. [Online]. Available: https://www.jove.com/science-education/10204/ultraviolet-visible-uv-vis-spectroscopy.

[248] J. Tauc and A. Menth, "States in the gap," *J. Non. Cryst. Solids*, 1972.

[249] T. Wang *et al.*, "Indirect to direct bandgap transition in methylammonium lead halide perovskite," *Energy Environ. Sci.*, 2017.

[250] J. Zhang, P. Zhou, J. Liu, and J. Yu, "New understanding of the difference of photocatalytic activity among anatase, rutile and brookite TiO2," *Phys. Chem. Chem. Phys.*, 2014.

[251] K. Ashok Kumar, J. Manonmani, and J. Senthilselvan, "Effect on interfacial charge transfer resistance by hybrid co-sensitization in DSSC applications," *J. Mater. Sci. Mater. Electron.*, 2014.

[252] X. Guo, C. McCleese, C. Kolodziej, A. C. S. Samia, Y. Zhao, and C. Burda, "Identification and characterization of the intermediate phase in hybrid organic-inorganic MAPbI3perovskite," *Dalt. Trans.*, 2016.

[253] A. Diantoro, M., Sa'adah, U., & Hidayat, "Effect of SnO2 Nanoparticles on Band Gap Energy of x (SnO2)-y (Ag)-β-Carotene/FTO Thin Film," *J. Phys. Conf. Ser.*, vol. 1093, no. 1, p. 012049, 2018.

[254] A. Tumuluri, K. Lakshun Naidu, and K. C. James Raju, “Band gap determination using Tauc’s plot for LiNbO3 thin films,” in *International Journal of ChemTech Research*, 2014.

[255] P. Syed Abthagir and R. Saraswathi, “Electronic properties of polyindole and polycarbazole Schottky diodes,” *Org. Electron. physics, Mater. Appl.*, 2004.

[256] C. Luongo, G., Di Bartolomeo, A., Giubileo, F., Chavarin, C. A., & Wenger, “Electronic properties of graphene/p-silicon Schottky junction,” *J. Phys. D. Appl. Phys.*, vol. 51, no. 25, pp. 255–305, 2018.

[257] V. Rajan, L., Periasamy, C., & Sahula, “Electrical characterization of Au/ZnO thin film Schottky diode on silicon substrate,” *Perspect. Sci.*, vol. 8, pp. 66–68, 2016.

[258] M. Onodera *et al.*, “Multiscale simulation of dye-sensitized solar cells considering schottky barrier effect at photoelectrode,” *Jpn. J. Appl. Phys.*, 2011.

[259] M. K. Nazeeruddin *et al.*, “Conversion of Light to Electricity by cis-X2Bis (2,2′-bipyridyl-4,4′-dicarboxylate) ruthenium (II) Charge-Transfer Sensitizers (X = Cl−, Br−, I−, CN−, and SCN−) on Nanocrystalline TiO2Electrodes,” *J. Am. Chem. Soc.*, 1993.

[260] M. Ni, M. K. H. Leung, D. Y. C. Leung, and K. Sumathy, “Theoretical modeling of TiO 2 /TCO interfacial effect on dye-sensitized solar cell performance,” *Sol. Energy Mater. Sol. Cells*, 2006.

[261] M. J. Jeng, Y. L. Wung, L. B. Chang, and L. Chow, “Dye-sensitized solar cells with anatase TiO2 nanorods prepared by hydrothermal method,” *Int. J. Photoenergy*, 2013.

[262] T. Zhao, W. Shi, J. Xi, D. Wang, and Z. Shuai, “Intrinsic and Extrinsic Charge Transport in CH3 NH3 PbI3 Perovskites Predicted from First-Principles,” *Sci. Rep.*, 2016.

[263] A. Sridharan, N. K. Noel, H. Hwang, S. Hafezian, B. P. Rand, and S. Kéna-Cohen, “Time-resolved imaging of carrier transport in halide perovskite thin films and evidence for nondiffusive transport,” *Phys. Rev. Mater.*, 2019.

[264] R. Schlaf, “Tutorial on Work Function,” *USF Surf. Sci. Lab.*, 2007.

[265] V. Zeghbroeck, “Principles of Semiconductor Devices: Metal-Semicond. Junctions,” *ecee.colorado*, 2011. [Online]. Available: https://ecee.colorado.edu/~bart/book/book/chapter3/ch3_2.htm.

[266] F. Rana, “Semiconductor Optoelectronics: Semiconductor Heterostructures,” *Cornell University*. [Online]. Available: https://courses.cit.cornell.edu/ece533/Lectures/handout2.pdf.

[267] B. Maldon and N. Thamwattana, “An analytical solution for charge carrier densities in dye-sensitized solar cells,” *J. Photochem. Photobiol. A Chem.*, 2019.

[268] D. Zhou, T. Zhou, Y. Tian, X. Zhu, and Y. Tu, “Perovskite-Based Solar Cells: Materials, Methods, and Future Perspectives,” *Journal of Nanomaterials*. 2018.

[269] A. Sproul, “UNSW Understanding the p-n Junction,” in *Solar Cells: Resource for the Secondary Science Teacher*, 2016.

[270] C. Cavallo, F. Di Pascasio, A. Latini, M. Bonomo, and D. Dini, “Nanostructured Semiconductor Materials for Dye-Sensitized Solar Cells,” *Journal of Nanomaterials*. 2017.

[271] I. Hussain, H. P. Tran, J. Jaksik, J. Moore, N. Islam, and M. J. Uddin, “Functional materials, device architecture, and flexibility of perovskite solar cell,” *Emergent Mater.*, 2018.

[272] N. Das, “Introduction of Nano-Structured Solar Cells,” in *Nanostructured Solar Cells*, 2017.

[273] S. Aharon, S. Gamliel, B. El Cohen, and L. Etgar, “Depletion region effect of highly efficient hole conductor free CH 3NH3PbI3 perovskite solar cells,” *Phys. Chem. Chem. Phys.*, 2014.

[274] Y. Shiraishi *et al.*, “Quantum tunneling injection of hot electrons in Au/TiO2 plasmonic photocatalysts,” *Nanoscale*, 2017.

[275] H. J. Snaith and M. Grätzel, “The role of a ‘schottky barrier’ at an electron-collection electrode in solid-state dye-sensitized solar cells,” *Adv. Mater.*, 2006.

[276] M. C. Gavin Conibeer, Arthur J. Nozik, Matthew C Beard Nozik, A. J., Conibeer, G., & Beard, *Advanced Concepts in Photovoltaics*. Royal Society of Chemistry, 2014.

[277] J. W. Zhiqun Lin, *Low-cost Nanomaterials: Toward Greener and More Efficient Energy Applications*. Springer, 2014.

[278] F. Gu, W. Huang, S. Wang, X. Cheng, Y. Hu, and P. S. Lee, “Open-circuit voltage improvement in tantalum-doped TiO2 nanocrystals,” *Phys. Chem. Chem. Phys.*, 2014.

[279] R. Suryana, Khoiruddin, and A. Supriyanto, “Beta-carotene dye of daucus carota as sensitizer on dye-sensitized solar cell,” in *Materials Science Forum*, 2013.

[280] W. O. Nirwana Sari Halidun, E. Cahya Prima, B. Yuliarto, and Suyatman, “Fabrication Dye Sensitized Solar Cells (DSSCs) Using β-Carotene Pigment Based Natural Dye,” in *MATEC Web of Conferences*, 2018.

[281] C. Cari, K. Khairuddin, T. Y. Septiawan, P. M. Suciatmoko, D. Kurniawan, and A. Supriyanto, “The preparation of natural dye for dye-sensitized solar cell (DSSC),” in *AIP Conference Proceedings*, 2018.

[282] D. Rangel, J. C. Gallegos, S. Vargas, F. García, and R. Rodríguez, “Optimized dye-sensitized solar cells: A comparative study with different dyes, mordants and construction parameters,” *Results Phys.*, 2019.

Appendix A: Reproducibility of the Diode Curves and the JV-Curves for Bio-DSSCs

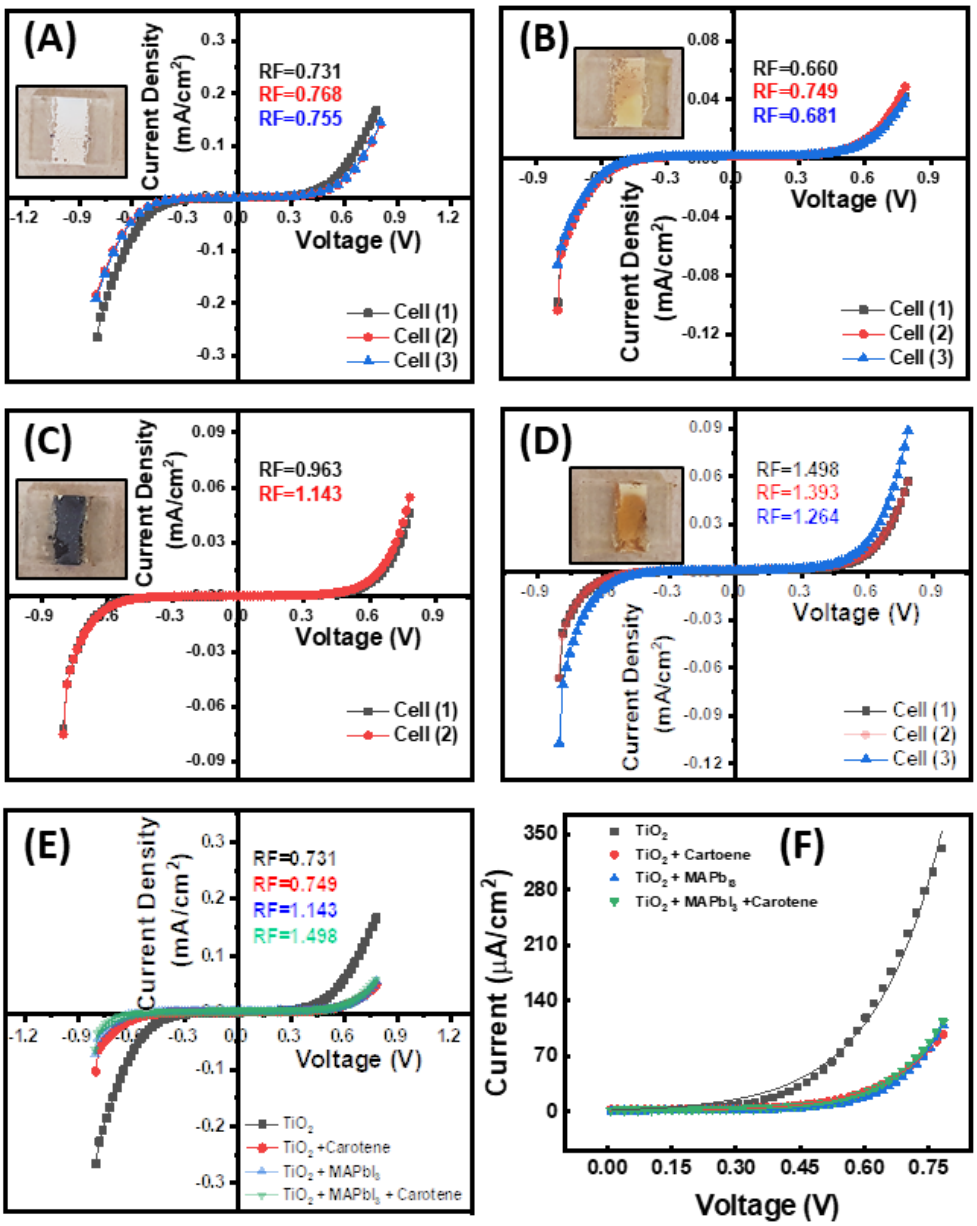

Figure A1. Diode curves and rectification factors (RFs) for bio-sensitized DSSCs using β-carotene dip-coated photoanodes: **(A)** ITO/TiO_2/[I^-/I_3^-]/rGO/ITO; **(B)** ITO/TiO_2/β-carotene/[I^-/I_3^-]/rGO/ITO; **(C)** ITO/TiO_2/$MAPbI_3$/[I^-/I_3^-]/rGO/ITO; and **(D)** ITO/TiO_2/$MAPbI_3$/β-carotene/[I^-/I_3^-]/rGO/ITO. **(E)** Comparison of diode curves and RFs obtained from using the four different bio-photoanodes with highest RF for design (d); **(F)** Exponential fitting of forward-current data using the TE diode model for diode ideality analysis.

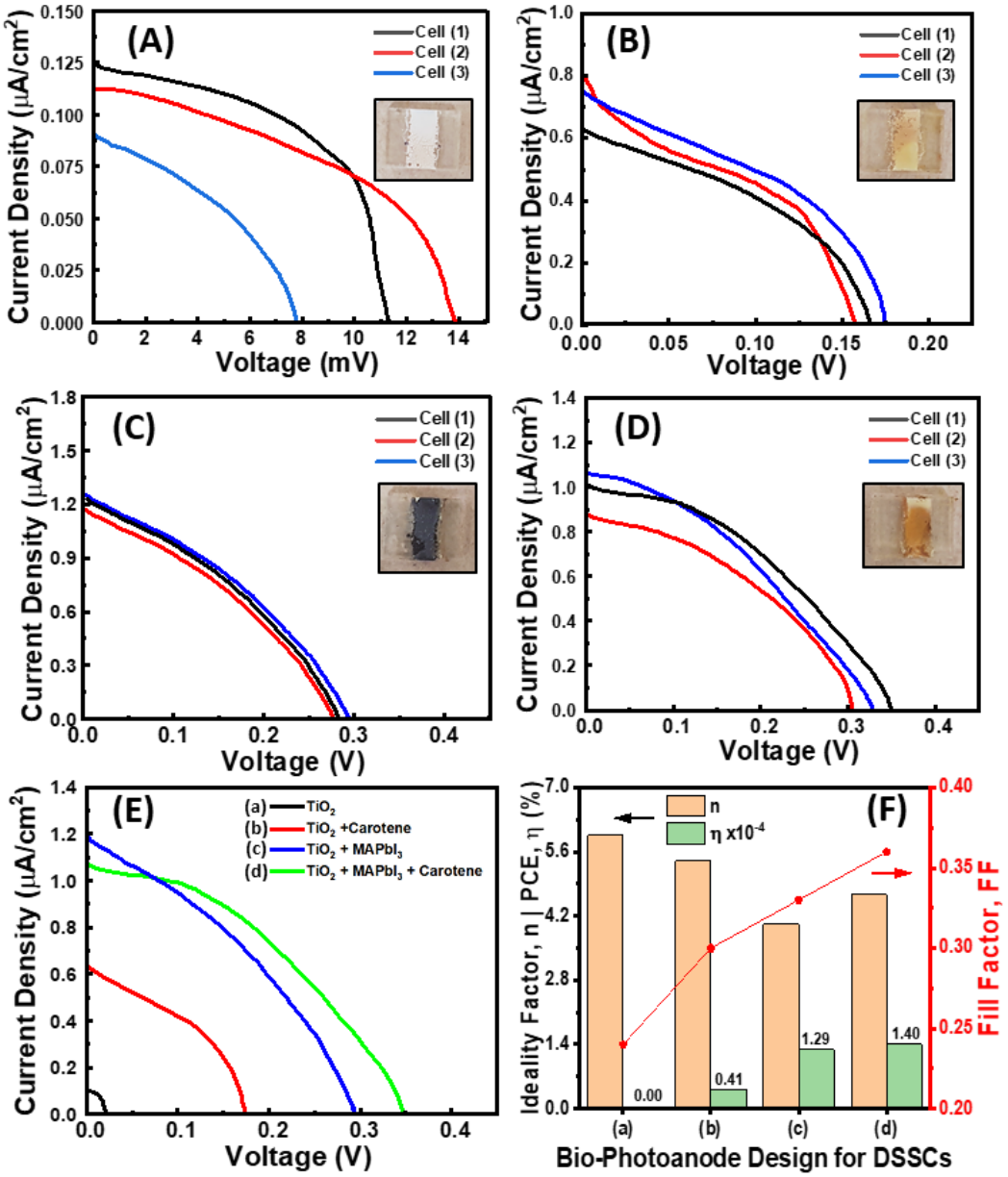

Figure A2. J-V curves for bio-sensitized DSSCs using β-carotene dip-coated photoanodes in: **(A)** ITO/TiO_2/[I^-/I_3^-]/rGO/ITO; **(B)** ITO/TiO_2/β-carotene/[I^-/I_3^-]/rGO/ITO; **(C)** ITO/TiO_2/$MAPbI_3$/[I^-/I_3^-]/rGO/ITO; and **(D)** ITO/TiO_2/$MAPbI_3$/β-carotene/[I^-/I_3^-]/rGO/ITO. **(E)** Comparison of J-V curves obtained from using the four different bio-photoanodes with highest V_{oc} for design (d); **(F)** Calculated ideality factor (n), conversion efficiency (PCE) and fill factor (FF) for the four bio-DSSCs devices.

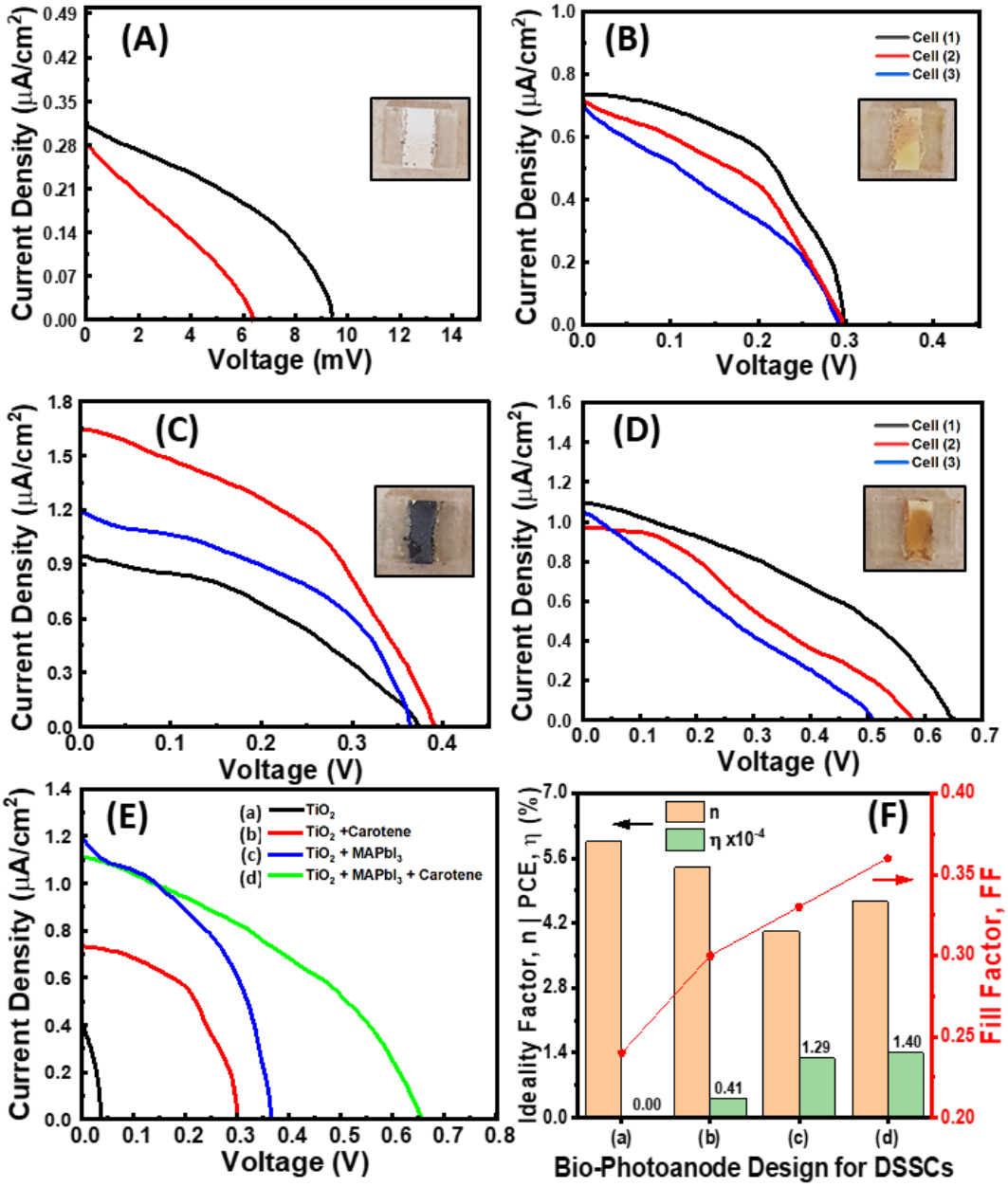

Figure A3. J-V curves for bio-sensitized DSSCs using β-carotene spin-coated photoanodes in: **(A)** ITO/TiO_2/[I^-/I_3^-]/rGO/ITO; **(B)** ITO/TiO_2/β-carotene/[I^-/I_3^-]/rGO/ITO; **(C)** ITO/TiO_2/$MAPbI_3$/[I^-/I_3^-]/rGO/ITO; and **(D)** ITO/TiO_2/$MAPbI_3$/β-carotene/[I^-/I_3^-]/rGO/ITO. **(E)** Comparison of J-V curves obtained from using the four different bio-photoanodes with highest V_{oc} for design (d); **(F)** Calculated ideality factor (n), conversion efficiency (PCE) and fill factor (FF) for the four bio-DSSCs devices.

Appendix B: Photovoltaic Parameters, Maximum PCE, and TE Models

Total cell current density (J_{cell}) can be obtained from Kirchhoffs's voltage (KVL) and current (KCL) laws to the circuit model yield in Eq. (S1) [235] that is the equivalent circuit model for DSSCs where q (1.602×10^{-18} C) is the electron charge, n is the ideality factor, k_B is Boltzmann constant (1.38×10^{-23} J K^{-1}), T is the absolute temperature (298 K), J_{ph} is photo-generated current, and J_0 is dark saturation current. Series resistance (R_s), shunt resistance (R_{sh}), and applied cell voltage (V_{cell}) in DSSCs play an important role in controlling J_{cell}.

$$J_{cell} = J_{ph} - J_0 \left[\exp\left(\frac{q(V_{cell} + J_{cell}R_s)}{nk_BT} \right) - 1 \right] - \frac{V_{cell} + J_{cell}R_s}{R_{sh}} \quad \text{(S1)}$$

The above equation, Eq. (S1), can be simplified further to estimate the DSSCs open circuit voltage (V_{oc}) from the following assumptions and considerations[235] (i) there is an infinite value of R_{sh}; (ii) $J_{cell} = 0$; (iii) $V_{cell} = V_{oc}$; $(I_{ph} >> I_0) \rightarrow (I_{ph} + I_0 \approx I_{ph})$; which will result in Eq. (S2) that is used to determine (J_{ph}/J_0) and J_{sc} for estimating the maximum theoretical PCE. With the assumption that Fermi-level and conduction-band energies in TiO_2 are approximately the same due to the intrinsic n-type behavior of TiO_2 ($E_f \approx E_{CB}$), one may estimate the maximum theoretical $V_{oc} \approx 1$ V. Using Eq. (S2-S4) with the obtained experimental results of the photoanode architecture (d) TiO_2 + $MAPbI_3$ + β-Carotene [n* = 4.67 (dip-coated) and 5.47 (spin-coated); FF* = 1; k_BT/q = 25.9 mV (T = 298 K); J_0 = 0.173 μA/cm^2 (dip-coated) and 0.081 μA/cm^2 (spin-coated); R_s = 0; $R_{sh} = \infty$; $J_{sc} = J_{cell}$ (V_{cell} = 0)], we have approximated the maximum PCE* that could be achieved by $MAPbI_3$/β-Carotene photoanodes interfaced with coal-derived-rGO-cathode in liquid-state DSSCs.

$$V_{oc} = \frac{nk_BT}{q} \ln\left(\frac{J_{ph}}{J_0}\right) = 1\ V \tag{S2}$$

$$\frac{J_{ph}}{J_0} \approx 3896 \rightarrow J_{sc}^{*} = J_{ph} - J_0 = 0.09{\sim}0.67\ mA/cm^2 \tag{S3}$$

$$PCE^{*} = \frac{P_m}{P_{in}} = \frac{J_{sc}V_{oc}FF}{100\ (mW/cm^2)} = 0.1\% \sim 0.7\% \tag{S4}$$

In a heterojunction diode structure, values like n, J_0, and series resistance (R_s) are important for cell performance characterization. In DSSCs, thermionic emission (TE) [242] and Cheung's methods[243], [245] can be used to quantify the diode parameters. TE model have been used to determine both n and J_0 as shown in Eq. (S5) from the exponential fitting [$y = a\exp(bx)$]. For ideal structures ideality factor (n = 1); however, usually n > 1 due to recombination and R_s from interfacial contacts [242], [243], [256], [257].

$$J = J_0 \exp\left(\frac{q\mathrm{V}}{nk_BT}\right) \tag{S5}$$

Appendix C: Performance Comparison of β-carotene-based DSSCs with Previous Works

Table C1. Performance comparison and photovoltaic parameters of various literature works on β-carotene-based DSSCs in contrast with the proposed bio-DSSCs system under AM1.5 radiation*

Pigment: Source / Absorbance | [Architecture]	**J_{sc} (μA cm^{-2})**	**V_{oc} (mV)**	**FF**	**η * (%)**	**Ref.**
Daucus Carota / 415-508 nm [FTO/TiO_2/β-carotene/[I^-/I_3^-]/C/FTO]	33	239	-	1.2 x 10^{-3}	[279]
Carrot / 400-510 nm; peaks: 433, 472.5 nm [FTO/TiO_2/β-carotene/[I^-/I_3^-]/Pt/FTO]	360	40	0.64	9 x 10^{-3}	[172]
Orange fruit; 400-510 nm; peaks: 441, 466.5 nm [FTO/TiO_2/β-carotene/[I^-/I_3^-]/Pt/FTO]	370	60	0.58	2 x 10^{-2}	[172]
Tomatoes / 400-510 nm; max: 441 nm and 466.5 nm [FTO/TiO_2/β-carotene/[I^-/I_3^-]/Pt/FTO]	510	140	0.37	3 x 10^{-2}	[172]
Syngonium sp leafs / 440-480 nm; peaks: 450, 480 nm; bandgap=2.47 eV; EL-HSE (High stability redox, Dyesol) [FTO/TiO_2/β-carotene/[I^-/I_3^-]/Pt/FTO]	270	400	0.68	7.4 x 10^{-2}	[280]
Yellow sweet potato / 400-500 nm; peaks: 401 nm [FTO/TiO_2/β-carotene/[I^-/I_3^-]/Pt/FTO]	0.27	515	-	5.7 x 10^{-2}	[281]
Purple sweet potato /400-500 nm; peaks: 532 nm, [FTO/TiO_2/β-carotene/[I^-/I_3^-]/Pt/FTO]	0.17	378	-	3.3 x 10^{-2}	[281]
β-carotene powder; 380 nm – 500 nm [ITO/TiO_2/β-carotene/[I^-/I_3^-]/C/ITO]	162	123	0.039	1 x 10^{-4}	[282]
β-carotene powder; 218 nm – 479 nm [ITO/TiO_2/$MAPbI_3$/β-carotene/[I^-/I_3^-]/rGO/ITO]	1.10	655	0.63	4.6 x 10^{-4}	This work

* J_{sc} = Short-circuit current density; V_{oc} = Open-circuit voltage; FF = Fill factor; η = Incident photon-to-current efficiency (IPCE) = Quantum efficiency (QE). Note that we have used the β-carotene powder source similar to the last reported study [282], Sigma US, and recorded better η.

Appendix D: Stability Over Time (3 months) of Bio-DSSCs with Dip-Coated Photoanodes

Incident light: 100 mW/cm^2 [~20 hr of total radiation for 3 months; equivalent to 9 measurements with 2 hours of radiation for each analysis]

Redox refill: 1-2 drops of iodide-triiodide are added before each measurement [~9 times]

Humidity: 20 – 35%

Temperature: 23 °C

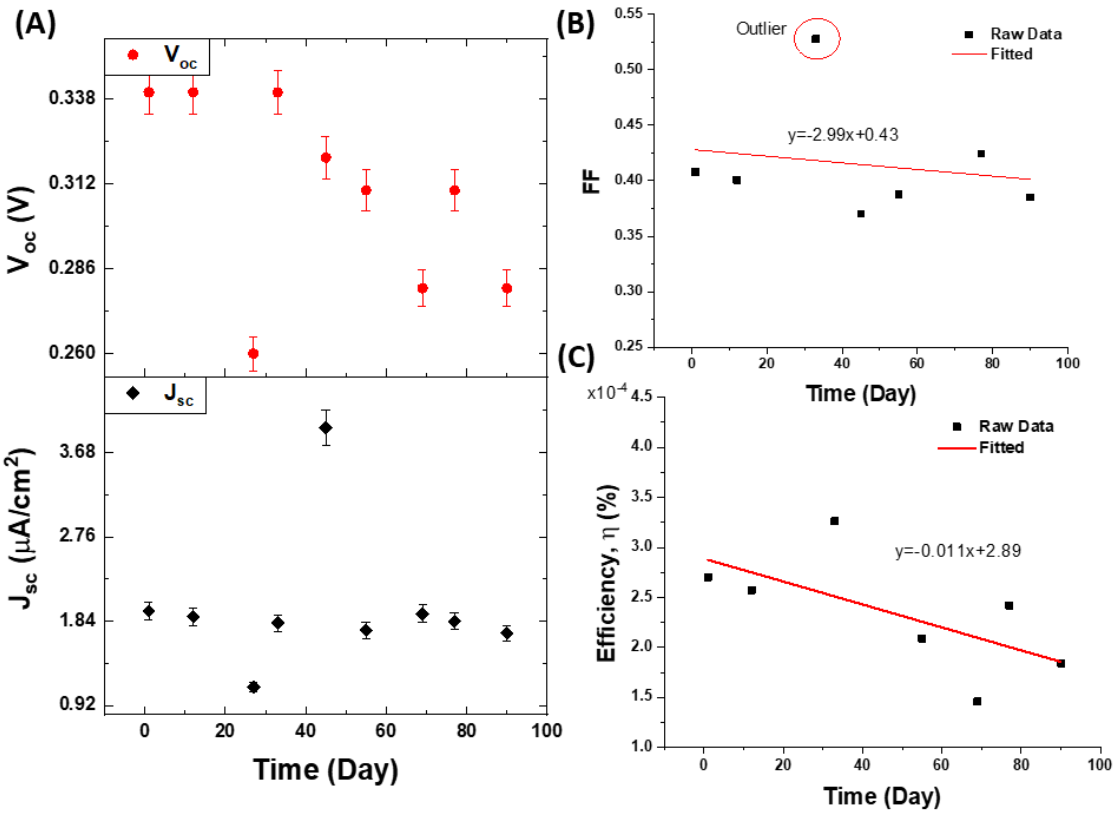

Figure D1. Cell stability over time for bio-sensitized DSSCs using β-carotene dip-coated photoanodes: **(A)** Changes in the observed V_{oc} (2% error bars) and J_{sc} (5% error bars); **(B)** Slight reductions in FF with the estimated linear fitted relationship considering an outlier value; **(E)** Slight reductions in efficiency with the estimated linear fitted relationship after removing any outlier values.

Copyright Clearance Center | RightsLink®

Home | Help | Email Support | Sign in | Create Account

Biomolecular photosensitizers for dye-sensitized solar cells: Recent developments and critical insights

Author: Hisham A. Maddah,Vikas Berry,Sanjay K. Behura

Publication: Renewable and Sustainable Energy Reviews

Publisher: Elsevier

Date: April 2020

Please note that, as the author of this Elsevier article, you retain the right to include it in a thesis or dissertation, provided it is not published commercially. Permission is not required, but please ensure that you reference the journal as the original source. For more information on this and on your other retained rights, please visit: https://www.elsevier.com/about/our-business/policies/copyright#Author-rights

BACK | CLOSE WINDOW

Copyright Clearance Center | RightsLink®

Home | Help | Email Support | Sign in | Create Account

Cuboctahedral stability in Titanium halide perovskites via machine learning

Author: Hisham A. Maddah,Vikas Berry,Sanjay K. Behura

Publication: Computational Materials Science

Publisher: Elsevier

Date: 15 February 2020

Please note that, as the author of this Elsevier article, you retain the right to include it in a thesis or dissertation, provided it is not published commercially. Permission is not required, but please ensure that you reference the journal as the original source. For more information on this and on your other retained rights, please visit: https://www.elsevier.com/about/our-business/policies/copyright#Author-rights

BACK | CLOSE WINDOW

VITA

HISHAM AGEEL MADDAH
Ph.D. Candidate, Department of Chemical Engineering
University of Illinois at Chicago, Chicago, IL 60607
E-Mail: hmadda2@uic.edu; hmaddah@kau.edu.sa

(a) Professional Preparation

University of Illinois at Chicago, USA	Chemical Engineering	Ph.D.	2020
University of Southern California, USA	Chemical Engineering	M.Sc.	2017
King Abdulaziz University, KSA	Chemical Engineering	B.Sc.	2012

(b) Appointments

11/18 – Present Lab Assistant, Chemical Engineering, University of Illinois, Chicago, USA
01/16 – 12/16 Research Assistant, Chemical Engineering, University of Southern California, LA, USA
02/14 – 08/14 Teaching Assistant, Chemical Engineering, King Abdulaziz University, Rabigh, KSA

(c) Peer-Reviewed Publications (Selected)

(1) **Maddah, H. A.**, Berry, V., & Behura, S. K. (2020). Biomolecular Photosensitizers for Dye-Sensitized Solar Cells: Recent Developments and Critical Insights. ***Renewable and Sustainable Energy Reviews***, *121*, 109678.
(2) **Maddah, H. A.**, Berry, V., & Behura, S. K. (2020). Cuboctahedral stability in Titanium halide perovskites *via* machine learning. ***Computational Materials Science***, *173*, 109415.
(3) **Maddah, H. A.,** Aryadwita, L., Berry, V., & Behura, S. K. (2020). Perovskite Cosensitization for Reduced Voltage Loss in Naturally-Sensitized Solar Cells, ***Nano Energy,*** Under-Review.
(4) Emani, P. S.[#], **Maddah, H. A.**[#], Rangoonwala, A., Che, S., Gruen, D. M., Berry, V., & Behura, S. K. (2020). Organophilicity of Graphene Oxide for Enhanced Wettability of ZnO Nanowires, ***ACS Applied Materials & Interfaces,*** Under-Review. [#]Equally contributing authors.

(d) Conferences (Selected)

(1) **Maddah, H. A.,** Aryadwita, L., Berry, V., & Behura, S. K. (2020). Perovskite Co-Sensitization of Naturally-Sensitized β-Carotene Photoanode for Dye-Sensitized Solar Cells. *In* ***12th Annual AIChE Midwest Regional Conference.***
(2) **Maddah, H. A.,** Berry, V., Behura, S. K. (2019). Random Sampling of Ionic Radii and Discrete Distributions for Structural Stability and Formability of Titanium-Based Perovskites. In ***APS/CNM Users Meeting.***
(3) **Maddah, H. A.,** Berry, V., & Behura, S. K. (2019). Random Sampling of Ionic Radii and Discrete Distributions for Structural Stability and Formability of Titanium-Based Perovskites. *In* ***11th Annual AIChE Midwest Regional Conference.***
(4) **Maddah, H. A.,** Berry, V., & Behura, S. K. (2018). Anthocyanin Coated TiO_2 as a Photoanode in Dye-Sensitized Solar Cells. *In* ***2nd Annual Graduate Research and Career Symposium at UIC***. [Best Poster Award]

(e) Book Chapters

(1) **Maddah, H. A.**, Jhally, A., Berry, V., Behura, S. K. (2020). Highly Efficient DSSCs with 3D Graphene-Based Materials, ***Royal Society of Chemistry***, Under-Review.